University of Bath

UNIVERSITY OF
BATH

PHD

Adaptive neurocomputation with spiking semiconductor neurons

Zhao, Le

Award date:
2015

Awarding institution:
University of Bath

[Link to publication](#)

ADAPTIVE NEUROCOMPUTATION WITH SPIKING SEMICONDUCTOR NEURONS

Le Zhao

A thesis submitted for the degree of Doctor of Philosophy

University of Bath

Department of Physics

September 2014

COPYRIGHT

Signature：赵乐

This thesis is dedicated to the memory of my grandfather, Changsheng Zhao.

Abstract

In this thesis, we study the neurocomputation by implementing two different neuron models. One is a semi magnetic micro p-n wire that emulates nerve fibres and supports the electrical propagation and regeneration. The other is a silicon neuron based on Hodgkin-Huxley conductance model that can generate spatiotemporal spiking patterns. The former model focuses on the spatial propagation of electrical pulses along a transmission line and presents the thesis that action potentials may be represented by solitary waves. The later model focuses on the dynamical properties such as how the output patterns of the active networks adapt to external stimulus. To demonstrate the dynamical properties of spiking networks, we present a central pattern generator (CPG) network with winnerless competition architecture. The CPG consists of three silicon neurons which are connected via reciprocally inhibitory synapses. The network of three neurons was stimulated with current steps possessing different time delays and that the voltage oscillations of the three neurons were recorded as a function of the strengths of inhibitory synaptic interconnections and internal parameters of neurons, such as voltage thresholds, time delays, etc. The architecture of the network is robust and sensitively depends on the stimulus. Stimulus dependent rhythms can be generated by the CPG network. The stimulus-dependent sequential switching between collective modes of oscillations in the network can explain the fundamental contradiction between sensitivity and robustness to external stimulus and the mechanism of pattern memorization.

We successfully apply the CPG in modulating the heart rate of animal models (rats). The CPG was stimulated with respiratory signals and generated tri-phasic patterns corresponding to the respiratory cycles. The tri-phasic stimulus from the CPG was used to synchronize the heart rate with respiration. In this way, we artificially induce the respiratory sinus arrhythmia (RSA), which refers to the heart rate fluctuation in synchrony with respiration. RSA is lost in heart failure. Our CPG paves to way to novel medical devices that can provide a therapy for heart failure.

Acknowledgements

Contents

Chapter 1 Introduction

1.1 Motivation of the Thesis

Biological nervous system receives information from the outside world and computes and communicates in the form of electrical impulses, also known as spikes. Computational neuroscience [1, 2] aims at describing and expressing information process in nervous system, such as how information is encoded in spikes, how these spikes travel along specific pathways in the nervous system and how the central nervous system makes decisions based on the incoming signals, etc.

One primary reason for studying the neurocomputation is that in comparison with traditional digital computation, biological neurons are shown to be extremely effective in information process. For example, processing speed of human brain is about 10 fold greater than the computers' for face recognition [3]. Moreover, brains can perform tasks which are too complex to be processed by digital computers in any length of time, such as motor control during locomotion [4], pattern recognition based on incomplete information [5, 6], associative memory [7], etc.

Computation in neural systems is a dynamical process [8]. One aspect of research on neurocomputation is to study the dynamical properties in particular neuron models. The study can carry out either in software [9, 10] or in hardware [11]. A software simulation is suitable for performing neurocomputation in small networks or developing new algorithms. However, if large networks with learning ability are to be used, a software simulation would not be a good choice any more due to the high time consuming. Instead, hardware is in need for building efficient adaptive systems.

Choosing neuron models is an issue on keeping a balance between incorporating sufficient details to demonstrate selected features of neural dynamics and reducing the complexity to make a model tractable [12]. The aim of this thesis is to study the propagation of electrical pulses along artificial nerve fibres as well as the neuron adaptability. The spatial aspect of neurons is important because nerve fibres operate as transmission delay lines to phase the timing of spikes[13], which is essential for neural computation[14]. Neuron adaptability is related to brain functions such as memory storage, temporal pattern recognition [8], etc.

For the former goal, we emphasize the spatial structure of the neuron model. On way to achieve the spatially delocalised nervous system is using synaptic connections to construct neural networks with particular architecture [8]. Besides, a new medium, which is p-n wires, for channelling electrical pulses has been proposed [15]. Here we use a p-n wire to demonstrate that it can support soliton-like electrical pulses propagating through it.

For the latter goal, we start from building a single neuron which can replicate the temporal response of a nerve fibre to an excitatory current [20]. And we go further and use these silicon neurons to construct a small neural network which can generate spatiotemporal patterns. We study the adaptability of the network by recording the stimulus dependent spike patterns. Besides, we use it as a new medical appliance to modulate the heart rate of rats during which physiologically realistic signals are in need. Bearing these aims in mind we choose to implement Hodgkin-Huxley (HH) neuron model [16, 17]. This is bottom up dynamical neuron model which can describe individual neurons in details. On one side, it is a sufficiently realistic neuron model as a suitable tool for exploring the dynamics in the biological nervous systems. Using this model will be faster and more convenient than using animals. On the other side, it is a biophysically meaningful model that can precisely match the known physiological parameters thus the output of it can satisfy the standard for medical experiments. Also the interaction between it and the real neurons is possible.

And we implemented HH neuron using analogue components because of the benefits from advantages of analogue techniques. First, analogue neurons can compute the complex nonlinear equations of the HH models for large systems more quickly and flexibly than software does. Secondly, operation of analogue computation is accurate and in real time. Thirdly, analogue chips can be miniaturized. All these advantages will be beneficial for the study of the dynamical properties in neural network as well as in implant of artificial neurons in animals.

As set forth, the dynamic property of the neural network that we are interested in is how the network adapts to external stimulus. And we study it by recording the spatiotemporal patterns generated by the network. The spatiotemporal pattern will be shown as an attractor in the phase space when the oscillations of the neural network are steady and periodic. The adaptability will result in the evolution from initial conditions to the common attractor along different trajectories. This evolution can happen while the parameters of the system, such as intrinsic properties of individual neurons, connection strengths, etc. are all fixed.

And a neural system can possess several attractors. The attraction dynamics can be a mechanism of inaccurate pattern recognition in living neurons as the inaccurate input will lead to trajectories within the basin of attraction converging towards the attractor. The existence of multi-attractors can stand different memory states.

The dynamical mechanism underlying the neural network is winnerless competition principle (WLC) [18]. In a winnerless competition neural network, neurons compete with each other for firing and the firing sequence is stimulus-dependent. This paradigm explains why a neural system can be sensitive to incoming stimulus as well as robust against noise. What more, WLC network possesses remarkable capacity of producing a big number of different patterns. For example, for a network with N neurons, the number of distinguishable patterns could be of order e (N-1)![18]. This number is corresponding to the possible number of memory states. Furthermore, WLC network possesses rich dynamical features such as multi-attractors, transient dynamics, etc. Therefore, inducing WLC dynamics into our neural network is crucial for us to study the stimulus dependent rhythms in the networks.

1.2 Background Information

1.2.1 The Functional Parts and Electrical Properties of Neurons

The neuron is a fundamental structure of the nervous system that receives incoming information and computes and transmits information through chemical or electrical signals. An idealized neuron can typically be divided into three functional parts: the dendrites, the soma, and the axon, as shown in figure 1.1(a) [19]. The dendrites are 'input devices' that collect signals from other neurons and transmit them to the soma. The soma integrates inputs. If the total inputs exceed a certain threshold, then an output signal is generated and transmitted over the axon. The axon terminates at a variable distance from the soma. The distance ranges from less than one millimetre to more than one meter [20].

The junctions that connect the terminal region of the axon of one neuron to dendrites of another neuron are called synapses [21]. They are shown in figure 1.1(a). Synapses allow signals transmitted from one neuron to another. Commonly the neuron which sends signals is called a presynaptic cell and the neuron which receives signal is called a postsynaptic cell. According to the influence, synapses fall into two categories: one is excitatory synapses and the other is inhibitory synapses. An excitatory synapse is a synapse in which

the signal from the presynaptic cell increases the probability of activation of the postsynaptic cell. An inhibitory synapse is a synapse in which the signal from the presynaptic cell decreases the probability of activation the postsynaptic cell [22]. According to the operation mechanism, there are two types of synapses in neurons: one is chemical synapses and the other is electrical synapses. Chemical synapses transmit signals by releasing chemicals through the junction between neurons or from neuron cells to non-neuronal cells such as muscle or glands. Electrical synapses function as Ohmic electrical connections between the membranes of two neuron cells. In this thesis, we choose the electrical synapse to model for two reasons. First, electrical synapses are faster than chemical synapses. Second, electrical synapses are bidirectional while chemical synapses are unidirectional [22]. The influence of bidirectional synaptic signal can be from either neuron to the other. We take the advantage of bidirectional operation of electrical synapses to switch them between 'being excitatory' and 'being inhibitory'. Details about the design of the artificial synapses are demonstrated in 3.3.

The elementary unit of electrical neuronal signalling is spikes consisting of electrical pulses as shown in figure 1.1(b). They are also called action potentials. A spike has amplitude of about 100mV and typically duration of 1-2ms [8].

A spike is carried by ions, such as Na^+, K^+, Ca^{2+}, Cl^-, etc. It results from the movement of ions across the neuron cell membrane through ion channels, which are embedded in membranes and gated by the membrane voltage [19]. At rest, the ion channels are shut. There is no ionic current flowing across the neuron cell membrane. Concentrations of ions maintain steady values inside and outside the neuron. For example, potassium ions have higher concentration inside the neuron while sodium ions have higher concentrations outside. Although no ion can move through the ion channels, there is potassium current because the membrane is selectively permeable to potassium. This leads to the imbalance distribution of charges inside and outside the neuron and eventually results in the polarization of the neuron cell membrane. The potential of inside the neuron is about 60mV less than that of outside the neuron. Based on the physiologists' sign convention, the potential in the exterior of the neuron cell is defined to be zero and inward is negative. Thus the resting membrane potential of a neuron is about -60mV. The resting potential is also called equilibrium potential. It can be calculated by the Nernst equation, which relates the concentration of ions to the electric gradient that balance it. The equation is shown as below [23]:

$$V_r = \frac{RT}{zF} \ln(\frac{C_{out}}{C_{in}})$$

<div align="right">(1. 1)</div>

Where V_r is the resting potential, R is the ideal gas constant, T is the temperature of solution in Kelvin, z is the valence of the ion, C_{out} is the concentration of the ion outside the neuron, and C_{out} is the concentration of the ion inside the neuron.

A spike is initiated when the neuron cell membrane is depolarized [19]. The voltage at which the depolarization is sufficient to trigger a spike is called the threshold. Usually we say a neuron is fired when the neuron is triggered to generate a spike. A neuron can be fired by injecting a current stimulus. And the value of the injected current which is sufficient to fire a neuron is called the threshold of the stimulus. The dynamic process of generating a spike is associated with the dynamics of ion channels and the movements of ions across the neuron cell membrane [8]. This is quite complex process. Here we only take into account the sodium and potassium ions to demonstrate the simplified process of initiating a spike. When a current stimulus which is above the threshold is injected into the neuron, first the sodium channels open such that sodium ions move from outside to inside. The neuron is therefore depolarized and become more positive. The potassium channels start to open when the sodium channels start to close. When potassium channels open, potassium ions move from inside to outside of the neuron, the neuron goes back to the negative state. If the membrane is charged more negatively than its resting potential, it is said to be hyperpolarized, in which case the generation of the next spike is inhibited. The hyperpolarization ends up when potassium channels close. Then the neuron goes back to the rest state and another spike can be generated.

Information in the nervous system is encoded by spiking patterns. In spiking patterns, both the rate and the timing of spikes are crucial for encoding information [21]. The nervous system processes and transmits information by generating and propagating spiking patterns [8]. The flow of information starts from the sensory systems, where it is captured and encoded, and then it is transmitted to central nervous systems. In central nervous system, response spiking patterns are generated. After that, spiking patterns are transported to the muscles to produce behaviours (dynamical principles). Neurocomputation is a subject that studies how the information is processed in all the stage. One generalization of studying neurocomputation is analysing the spatial, temporal and spatial-temporal aspects of neurocomputation. The spatial aspect concerns the transmission of spikes in space, such as how the spikes propagating along the neuron nerve fibres, etc. The temporal aspect

concerns how the information is processed by the rate and timing of spikes. The spatial-temporal aspect is the combination of the former two.
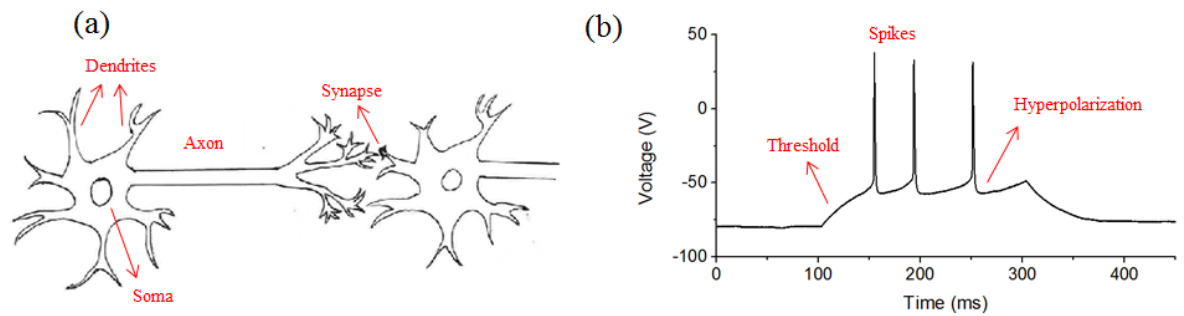
Figure 1.1 Illustration of the functional parts and electrical properties of neurons. (a) A schematic figure of neurons. A single neuron consists of dendrites, a soma and axons. The neurons are connected together by synapses. (b) An example of neuronal action potentials, which is commonly called spikes. A spike is a short voltage pulse of 1-2 ms duration and amplitude of about 100mV. It is generated when the depolarization of the membrane is above the threshold. A spike is followed by a hyperpolarization period during which the generation of the next spike is inhibited. This plot is the courtesy of Dr. Daniel Meliza. It is the electrophysiological recording of a neuron from the songbird high vocal centre in response to a current stimulus of 0.75nA.

1.2.2 Modelling Propagation Delays Using Semiconductor P-N Wires

The spatial propagation of spikes and propagation delays along the neuron nerves are important for the neurocomputation. For example, dendrites transmit signals from many neurons to the soma or central processing unit. The soma only integrates inputs that arrive within a particular time window [24, 25]. In this way, the soma acts as a coincidence detector for incoming pulses to indicate if spikes are synchronized as well as generate outputs according to the correlations in the input patterns. This function is crucial for neurocomputation based on timing of spikes, such as Hebbian learning rule based on spike timing dependent plasticity [26], azimuthal sound localization based on spike arrival times in the auditory system of barn owls [27, 28], etc.

P-n wires are proposed to be a proper medium for spatially propagating spikes analogue to signalling in neuron nerve fibres [15].

The first reason for choosing p-n wires as the medium is that p-n junctions share many common physical properties with nerve fibres [15]. The key elements in a neuron that perform electric properties include the membrane, the charge carriers and the resting

potential. The membrane is an insulator that can separate and accumulate electrical charges. The charge carriers are crucial for the generation of spikes. And the resting potential is a parameter associated with the charge distribution across the neuron cell membrane and it can be calculated by the Nernst equation as shown in the equation 1.1. In p-n junctions, the depletion region is an insulating region that spatially separates the p type and n type electrode. Charge carriers are the majority and minority carriers such as electrons and holes. As a result of the imbalance of charge carriers across the depletion region, a potential barrier is established and it can also be defined by the Nernst equation. This potential is generally called the built in potential.

Secondly, electrical characteristics of p-n wires can model the characteristics of electrical signalling along the biological nerve fibre. The electrical signalling depends on the axial resistance along the membrane, the radial conductivity through the membrane and the capacitance of the nerve membrane. The axial resistance is due to the resistance of capillary to movements of electric charge [29]. For a neuron surrounded by a large volume of conducting fluid, the internal resistance is larger than the external one. For a semiconductor like GaAs, the n type mobility is bigger than the p type. Therefore we can model the internal resistance by the resistance between p type electrodes along GaAs based p-n wires and model the external resistance by the resistance between n type electrodes along GaAs based p-n wires [15]. Regarding the radial conductivity, the ion conductance is nonlinear because the ion channels are voltage controlled and only open when the membrane potential crosses the threshold [16]. The exponential conductivity of the p-n junction exhibits equivalent nonlinearity. Regarding the capacitance of the neuron membrane, it can be modelled by the capacitance of the depletion layer of the p-n wire. The charging and discharging rate of capacitors determine the speed of signals.

Thirdly, it has been demonstrated in experiments that p-n wires can functionally model the nerve fibres. P-n wires possess the capability of integrating multiple inputs in space and time and regenerating pulses exceeding the voltage threshold [24, 30, 31]. Moreover, they are able to demonstrate stochastic phenomena like stochastic resonance [32], which was observed in biological neurons [33].

Lastly, a p-n wire is a monolithic neuron model for studying the spatial aspect of neurocomputation[15] and the structure of it is simple. Another way of emulating the spatial aspects of neurocomputation of single neurons, such as multiple inputs integration,

is introducing coupling between multiple compartments [12]. Each compartment is a neuron model that has only temporal parameters in it. By contrast, p-n wires provide with a straightforward way of studying the pulse propagation in space.

1.2.3 Computation in a Single Neuron: Hodgkin-Huxley Model

Hodgkin-Huxley (HH) neuron is neuron model that neglects the neuron's spatial structure and focus on how various ionic currents contribute to the generation of spikes [12, 17]. They transfer the effects of different ionic channels to the capacity and resistance of the membrane and build an equivalent circuit. They use a set of nonlinear equations to describe ionic mechanisms underlying the initiation and propagation of neural spikes in detail. The Hodgkin and Huxley neuron offers an accurate model of the physiological data. And it provides a quantitative description of the neural behaviour.

According to HH approach, the electrical properties of a neuron are modelled by an electrical equivalent circuit similar to that shown in figure 1.1 [17]. In the figure, capacitors represent the charge storage capacity of the cell membrane, resistors represent the various types of ion channels embedded in membrane, and batteries represent the electrochemical potentials established by differing intra- and extracellular ion concentrations. Current flow across the membrane has two major components, one is from charging the membrane capacitor, and the other is from specific ions across flowing across the membrane.
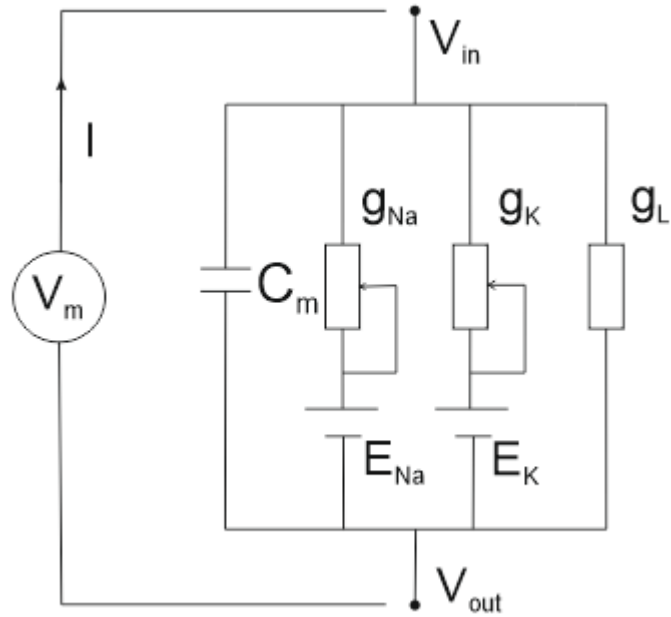
Figure 1.2 The electrical circuit proposed by Hodgkin and Huxley [17]. It is an equivalent circuit of bio-membrane. The capacitor represents the capacitance of the cell membrane. Two variable resistors represent sodium and potassium conductance respectively, which varies with time and membrane potential. The fixed resistor represents a constant leakage conductance, which represents channel types that are not described explicitly. The three batteries represent the electrochemical potentials for the corresponding conductance. The potentials are generated by the difference in ion concentrations between the outside and inside nerve membrane.

Applying the Kirchhoff's current law to figure 1.2, the behaviour of the electrical circuit can be described by a differential equation as below:

$$C_m \frac{dV_m}{dt} + I_{ion} = I \tag{1.2}$$

Where C_m is membrane conductance, V_m is membrane potential, I is the total membrane current. The ionic current I_{ion} is further subdivided into three distinct components, a sodium current I_{Na}, a potassium current I_k, and a small leakage current I_L which is primarily carried by chloride ions. Thus

$$I_{ion} = I_{Na} + I_K + I_L \tag{1.3}$$

The ionic current I_{ion} is assumed to be related to the membrane voltage through an Ohm's law relationship of the form $V=IR$. And this relationship is expressed in terms of conductance rather the resistance for the convenience, in which case Ohm's law becomes

I=GV, where *G* is the conductance of an ion channel and it is the inverse of resistance, *G=1/R*. In applying this relationship and the Kirchhoff's voltage law to ion channels, equation (1.3) can be expanded to the following expression:

$$I_{ion} = G_{Na}(V_m - E_{Na}) + G_K(V_m - E_K) + G_L(V_m - E_L) \qquad \textbf{(1.4)}$$

Where E_{Na}, E_K and E_L is equilibrium potential for each ion type. They are empirical parameters. Applying equation (1.4) to equation (1.2), we will obtain the fundamental equation relating the change in membrane potential to the currents flowing across the membrane [17]:

$$I = C_m \frac{dV_m}{dt} + G_{Na}(V_m - E_{Na}) + G_K(V_m - E_K) + G_L(V_m - E_L) \qquad \textbf{(1.5)}$$

In order to explain the experimental data, Hodgkin and Huxley proposed that G_{Na} and G_K were voltage-dependent quantities, whereas the leakage current G_L was taken as constant. Thus in figure 1.2, G_{Na} and G_K is represented by variable resistors and G_L is represented by a fixed resistor. Today we know that the conductance in HH model can be considered to arise from the combined effects of a large number of microscopic ion channels embedded in the membrane. Each type of ion channels contains physical gates that regulate the flow of ions through the channel. An individual gate can either be in 'open ' state or in 'close' state independently of one antoher. The total membrane conductance of a particular ion is the sum of the conductances from all the open gates corresponding to the ion. In HH neurons, the satistical model is used to calculate the channel conductance. We define p_i as the probability of an individual gate being in the open state. i represents the tye of the gate. P_i is a dimensionless variable which can vary between 0 and 1. If we consider a large number of channels, p_i then denotes the fraction of gates that are in the open state. $p_i(t)$ denotes the fraction of gates that in the open state at time *t*. Since there are only two possibilities for the states of the gates, $1 - p_i(t)$ denotes the the fraction of gates that are in close state.

The rate at which close gates transition to an a open state is governed by a variable $\alpha_i(V)$, which has units of 1/time. Here V is the displacement the membrane potential from its resting values. $\alpha_i(V)$ is known as 'rate constant'. Actually it is a function of membrane voltage but not of time. Similary, there is another rate constant $\beta_i(V)$ describing the rate at which open gates transition to an close state.Transitions between open and close states in the HH model can be described mathematically by using first-order kinetics:

$$\frac{dp_i}{dt} = \propto_i (V)(1 - p_i) - \beta_i(V)p_i \tag{1.6}$$

When the membrane voltage V_m is held at some fixed value V, then the fraction of gates in the open state will eventually reach a steady state value as $t \to \infty$. This is given by:

$$p_{i \to \infty} = \frac{\propto_i(V)}{\propto_i(V) + \beta_i(V)} \tag{1.7}$$

The time costant $\tau_i(V)$ for approaching the steady state is given by [17]:

$$\tau_i(V) = \frac{1}{\propto_i(V) + \beta_i(V)} \tag{1.8}$$

We say a channel is open when all the gates for the particular channel are open. When the particular channel is open, it contributes a fixed value to the total conductance . Otherwise it contributes zero. Therefore the conductance for a large population of chanels is proportional to the number of channels in the open state, which is in turn proportional to the probability that the associated gates are in the open state.

In HH model, the potassium channel is assumed to have only one type of gates based on experimental data. It is the activation gate. We lable it by the letter n. The rate constants for the activation gate of potassium channel are identified as $\alpha_n(V)$ and $\beta_n(V)$. Let $\overline{g_k}$ denote the maximum value of potassium channel conductance which corresponds to the state that all the gates are open, the potassium channel conductance can be expressed as the following equation [17]:

$$G_k = \overline{g_k}p_n{}^4 = \overline{g_k}n^4 \tag{1.9}$$

The sodium channel is assumed to have two types of gates according to experimental data, which are activation and inactivation gates. The activationi gate is identified by the letter m. The rate constants for the activation gate of sodium channel thus can be identified as $\alpha_m(V)$ and $\beta_m(V)$. The inactivation gate is labeled by the letter h. The rate constants for the activation gate of sodium channel thus can be identified as $\alpha_h(V)$ and $\beta_h(V)$. The conductance of sodium conductance is a function of both m and h. Let $\overline{g_{Na}}$ denote the maxium value of sodium conductance, the empirical expression of the sodium channel conductance is [17]:

$$G_{Na} = \overline{g_{Na}}p_m{}^3 p_h = \overline{g_{Na}}m^3 h \qquad \textbf{(1. 10)}$$

Summarizing euqations (1.2)-(1.10), a complete HH model consisting of the differential equation for the circuit of figure 1.2 and three differential equations describing the rate processes have been obtained [17]:

$$I = C_m\frac{dV_m}{dt} + \overline{g_{Na}}m^3\text{h}(V_m - E_{Na}) + \overline{g_k}n^4(V_m - E_K) + \overline{g_l}(V_m - E_L) \qquad \textbf{(1. 11)}$$

Where

$$\frac{dn}{dt} = \propto_n (V)(1 - n) - \beta_n(V)n \qquad \textbf{(1. 12)}$$

$$\frac{dm}{dt} = \propto_m (V)(1 - m) - \beta_m(V)m \qquad \textbf{(1. 13)}$$

$$\frac{dh}{dt} = \propto_h (V)(1 - h) - \beta_h(V)h \qquad \textbf{(1. 14)}$$

Equations (1.11)-(1.14) give the membrane current I as a function of time and membrane voltage. And Hodgkin and Huxley were able to experimentally determine the rate constants for potassium activation gate and sodium activation and inactivation gates as a function of membrane voltage. We summarize equations as follows [17]:

$$\alpha_n(V) = \frac{0.01(10-V)}{exp\left(\frac{10-V}{10}\right)-1} \qquad \textbf{(1. 15)}$$

$$\beta_n(V) = 0.125exp(-\frac{V}{80}) \qquad \textbf{(1. 16)}$$

$$\alpha_m(V) = \frac{0.1(25-V)}{exp(\frac{25-V}{10}-1)} \qquad \textbf{(1. 17)}$$

$$\beta_m(V) = 4exp(-\frac{V}{18}) \qquad \textbf{(1. 18)}$$

$$\alpha_h(V) = 0.07exp(-\frac{V}{20}) \qquad \textbf{(1. 19)}$$

$$\beta_h(V) = \frac{1}{exp\left(\frac{30-V}{10}\right)+1} \qquad \textbf{(1. 20)}$$

The units of the numbers in above equations are the same with the membrane voltage.

However, because of its complexity, HH model has difficulties in analysing and computation because they consume a lot of time when networks of two or three neurons need to be modelled [34]. For this reason, several simplification of the Hodgkin-Huxley equations have been proposed, such as series of integration and fire (IF) models [35-37], Fitzhugh-Nagumo model [38], Morris-Lecar models [39], etc. These models differ in their capability to reproduce firing patterns qualitatively and computational efficiency [40]. Usually the simpler model has better computational efficiency but provides poorer biological plausibility. For example, IF model with only one variable can be the simplest to implement. And it is the most efficient. Yet it lacks many fundamental properties of cortical spiking neurons, such as can only produce tonic spikes with constant frequency, etc.[40]. Thus it is suitable for the cases that require analytical results but do not need to realistically capture the spike generating mechanisms.

Neuron models are discussed and compared in papers [34, 40, 41] . Table 1.1 from Izhikevich [40] is provided for showing the comparison of the neurocomputational properties of spiking and bursting models.

Models	biophysically meaningful	tonic spiking	phasic spiking	tonic bursting	phasic bursting	mixed mode	spike frequency adaptation	class 1 excitable	class 2 excitable	spike latency	subthreshold oscillations	resonator	integrator	rebound spike	rebound burst	threshold variability	bistability	DAP	accommodation	inhibition-indiced spiking	inhibition-induced bursting	chaos	# of FLOPS
integrate-and-fire	-	+	-	-	-	-	-	+	-	-	-	-	+	-	-	-	-	-	-	-	-	-	5
integrate-and-fire with adapt.	-	+	-	-	-	-	+	+	-	-	-	-	+	-	-	-	-	+	-	-	-	-	10
integrate-and-fire-or-burst	-	+	+		+	-	+	+	-	-	-	-	+	+	+	-	+	+	-	-	-		13
resonate-and-fire	-	+	+	-	-	-	-	+	+	-	+	+	+	+	-	-	+	+	+	-	-	+	10
quadratic integrate-and-fire	-	+	-	-	-	-	-	+	-	+	-	-	+	-	-	+	+	-	-	-	-	-	7
Izhikevich (2003)	-	+	+	+	+	+	+	+	+	+	+	+	+	+	+	+	+	+	+	+	+	+	13
FitzHugh-Nagumo	-	+	+	-		-	-	+	-	+	+	+	-	+	-	+	+	-	+	+	-	-	72
Hindmarsh-Rose	-	+	+	+		+	+	+	+	+	+	+	+	+	+	+	+	+	+		+		120
Morris-Lecar	+	+	+	-		-	-	+	+	+	+	+	+	+		+	+	-	+	+	-	-	600
Wilson	-	+	+	+		+	+	+	+	+	+	+	+	+	+		+	+					180
Hodgkin-Huxley	+	+	+	+		+	+	+	+	+	+	+	+	+	+	+	+	+	+		+		1200

Table 1.1 Comparison of the neurocomputational properties of spiking and bursting models. This table is from ref. [40].

As the goal of our work in the thesis is to build a neural network which can generate physiologically realistic signals for medical applications, the HH model is well suited to this application. Implementing this scheme in analogue form frees computation from the prohibitive cost of integrating the Hodgkin-Huxley equations [17], which mathematically describe electrical properties of biological neurons, and realizes the real-time operation. Therefore the HH neuron model is the best choice for us. We will compute three coupled neuron together. This network is small enough to avoid the computational difficulty from the HH model.

1.2.4 Computation in a Neural Network: Dynamics of a Central Pattern Generator

One neural network whose dynamical properties are intensively studied is central pattern generators (CPGs) [42, 43]. The function of them are controlling rhythmic activities such as locomotion, breathing, heartbeat etc. [44]. Experiments have shown that CPG is a nonlinear network made of multiple coupled neurons whose output is spatiotemporal oscillations [8, 45]. A spatiotemporal oscillation is called a rhythmic pattern, or a rhythm. On one side, CPGs can functionally switch to generate spatiotemporal patterns with different rhythms in response to different sensory inputs, which are usually called initial conditions during experiments. This function allows animals to adapt their behaviour according to the environment. On the other side, CPGs display stable and reproducible rhythms that are robust against noise [46, 47].

A rhythm generated by a CPG corresponds to a limit cycle in the state space of the CPG output. In neuroscience, a limit cycle is a set of states toward which the outputs of the neural network will evolve. It is shown as a closed trajectory in the three dimensional projection of oscillation states of the neural network that other trajectories in the portrait will spiral into it as time approaches infinite [8]. An example of a limit cycle is given in figure 1.3 (a) [8, 48]. In the plot, x, y and z axis represents the oscillation state of LP, PD/AB, and VD neurons in pyloric CPG of lobster. Green trajectories indicate the irregular oscillation states of the CPG. And the blue limit cycle indicates the steady and periodic oscillation state of the CPG. The dynamic process that green trajectories eventually evolve into the blue limit cycle with time demonstrates how the CPG outputs evolve from irregular patterns into rhythmic patterns.
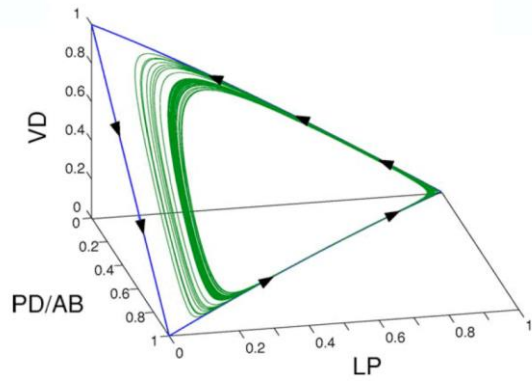
Figure 1.3 An example of a limit cycle. Axes in the plot are oscillation states of LP, PD/AB, VD neurons in pyloric CPG of lobster. Green trajectories correspond to irregular and aperiodic oscillation states of neurons. The blue trajectory is the limit cycle. It corresponds to steady and periodic oscillation states of neurons. This plot is from ref. [8].

A rhythm generated by a CPG also corresponds to an attractor in the phase space of the CPG output. In neuroscience, an attractor is a set of numerical properties toward which the neural system tends to evolve from various initial conditions [8, 49]. Attractors mentioned in the thesis specifically refer to fixed point attractors. An example of fixed point attractors is shown in figure 1.4. This plot is from a CPG consisting of three neurons. Axes in the plot are normalized time delays between oscillations from the three neurons. One of the neurons is chosen as the reference. During experiments, the CPG is stimulated by various initial conditions. Each initial condition leads to a specific orbit in the plot. Although orbits start from different coordinate points, they eventually converge to five fixed points, which are called attractors. Attractors are shown by red, green, blue, black and purple dots. These five attractors correspond to 5 different states when time delays between outputs of neurons are fixed such that the 5 attractors indicate 5 steady and periodic rhythmic patterns. An area in which all the orbits would converge to a common attractor is called an attractor basin. An attractor basin includes all the initial conditions that would lead to the common attractor. Plotting attractors tells which initial condition corresponds to which fixed attractor. Thus by reading this plot, we know how to switch between attractors by switching initial conditions. In other words, this plot tells how to switch between CPG output rhythms by switching initial conditions.

Artificial CPGs share the same dynamic properties with living CPGs, such as limit cycle dynamics, attractor dynamics, etc. Therefore they are often studied as models of neural network functions [50-52]. Depending on the aim of the study, CPG models have been designed at different levels of abstraction from biophysical models. To study the generation of rhythmic activity, usually networks with detailed neuron models like HH neurons are constructed [53, 54]. And numerical models have been used as tools for the study. The theories of dynamical systems have been proposed which can help in predicting dynamic behaviours, such as identifying when rhythms [55, 56] occur in the system depending on parameters such as coupling weights and intrinsic frequencies. In this thesis, we are going to construct CPG hardware with HH neurons and study the rhythmic patterns in it by studying limit cycle and attractor dynamics.

Structures of the CPGs have been studied for revealing the mechanism of regulating rhythms. Effect of different aspects, such as synaptic connections [57], sensory feedback [58, 59], etc. has been discussed. Of all the studies, the most common mechanism for generating rhythmic control is known as reciprocal inhibition, which will lead to a pair of neurons approximately firing out of phase with each other. Based on the previous theory and simulation work, we are going to construct CPG hardware by interacting HH neurons via inhibitory synaptic connections.
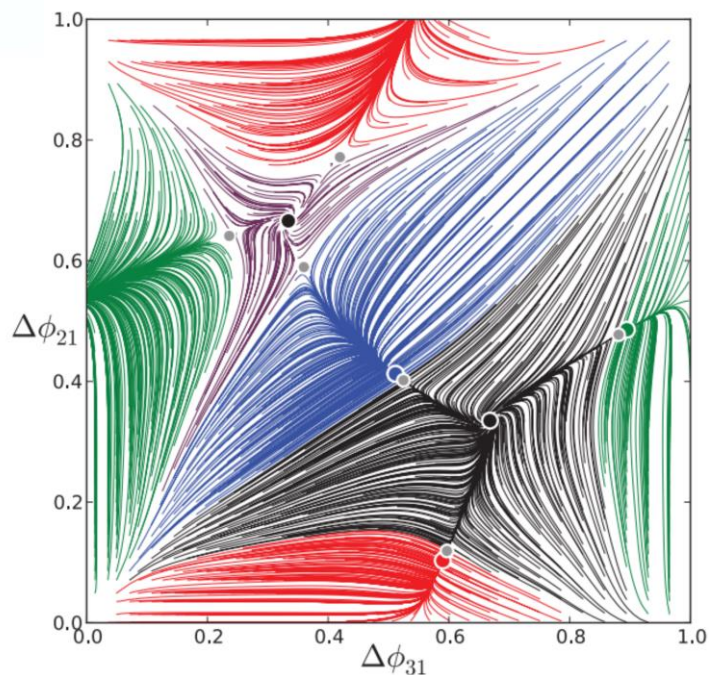

Figure 1.4 An example of fixed point attractors generated by a CPG consisting of 3 oscillating neurons. Axes in the plot are normalized time delays between oscillations from the 3 neurons. One

of the neurons, say neuron 1, is chosen as the reference. $\Delta\Phi_{31}$ is the normalized time delays between oscillations from neuron 3 and neuron 1. $\Delta\Phi_{21}$ is the normalized time delays between oscillations from neuron 2 and neuron 1. In the plot, there are 5 attractors. They are the red fixed point attractor at ($\Delta\Phi_{31} \approx \frac{1}{2}, \Delta\Phi_{21} \approx 0$), the green fixed point attractor at ($\Delta\Phi_{31} \approx 0, \Delta\Phi_{21} \approx \frac{1}{2}$), the blue fixed point attractor at ($\Delta\Phi_{31} \approx \frac{1}{2}, \Delta\Phi_{21} \approx \frac{1}{2}$), the black fixed point attractor at ($\Delta\Phi_{31} \approx \frac{2}{3}, \Delta\Phi_{21} \approx \frac{1}{3}$), and the purple fixed point attractor at ($\Delta\Phi_{31} \approx \frac{1}{3}, \Delta\Phi_{21} \approx \frac{2}{3}$). The five attractors correspond to five rhythmic patterns of the CPG. The area in which all the orbits would converge to a common attractor is called an attractor basin. There are 5 attractor basins in this plot: the red basin, the green basin, the blue basin, the black basin and the purple basin. An attractor basin includes all the initial conditions that would lead to the common attractor. This plot tells how to control the attractor of the CPG by switching initial conditions. This plot is from ref. [55].

1.3 Outline of the Thesis

Chapter 1 is the introduction. We demonstrate the motivation of the thesis, introduce information background, and outline the structure of the thesis.

In chapter 2, we are going to demonstrate spatially extended neuron based on magnetic semiconductor p-n wires. The wire mimics the action potentials of biological nerve fibres and supports the propagation of soliton. We also report on the different modes of soliton propagation as the temperature is varied through the Curie temperature of the material. Results from it will be compared to theoretical simulations.

In chapter 3, we are going to demonstrate how Hodgkin Huxley neuron and inhibitory synapses are constructed by silicon components. Response of a single neuron to current stimulus will be tested. We will show the intrinsic properties of a single silicon neuron, such as the amplitude of spikes, firing frequency, etc. Also, we will show spiking patterns from coupled neurons which are interacting with each other via either excitatory or inhibitory synapses.

In chapter 4, we go further by interconnecting these neurons via inhibitory synapses in networks of winnerless architectures. In this way, we built universal central pattern generator (CPG) hardware to demonstrate its adaptive behaviour by producing stimulus dependent rhythmic patterns. We are going to investigate the dynamics of neuron oscillations as a function of the time delay between current steps applied to individual

neurons. We demonstrate stimulus dependent switching between spiking rhythms and map the phase portraits of the neuron oscillations to reveal the basins of attraction of the system. We experimentally study the dependence of the attraction basins on the network parameters: the neuron response time and the strength of inhibitory connections.

In chapter 5, we demonstrate that the CPG hardware is potentially a new therapy for restoring the respiratory sinus arrhythmia in patients.

Chapter 6 is the conclusion. We will summarize the work in this thesis and discuss the future work.

Chapter 2 Modelling Propagation Delays Using GaMnAs/GaAs Solitonic Transmission Lines

2.1 Introduction

In this chapter, we will focus on the spatial aspect of neurocomputation by studying the propagation of soliton signals in a p-GaMnAs/n-GaAs wire.

It has been demonstrated in the subsection 1.2.1 that p-n wires can model biological neuron nerves. First of all, p-n wires can replicate physical properties of neuron membranes [15]. Secondly, analogue similarities exist between electrical properties of p-n wires and signalling characteristics of neuron nerves [15]. Thirdly, previous work on p-n wires has demonstrated experimentally that p-n wires can model functions of neuron nerves, such as integrating and regenerating electrical pulses in real time [24, 31], showing noise-controlled signal transmission [32], etc.

In this chapter, we carry on the study in GaAs based p-n wires. We aim to demonstrate that they support soliton propagation. Solitons are stationary pulses or wave packets which propagate in nonlinear dispersive media. They propagate without distortion of their forms. The stable waveforms result from a dynamical balance between the nonlinear and the dispersive effects. The possibility of soliton propagation in bio-membranes and nerves was proposed by Heimburg and Jackson in 2005 [60].

Our idea of modelling the soliton propagation in p-n wires is inspired by the proposal from T Kuusela et al in 1987 [61]. They showed propagation of solitons in LC transmission lines containing constant inductors and voltage-dependent capacitors. The nonlinearity in the system arises from the voltage-dependent capacitance. The inductance transformed the expression equations of the system from diffusion equation to wave equation. Nonlinearity together with the wave equation leads to Korteweg-de Vries (KDV) equation [62] which has soliton solutions. Then nonlinearity in the traditional GaAs based p-n wires arises from the voltage-dependent conductance of the p-n junction. We then improved the traditional GaAs based p-n wires by doping with Mn in order to induce inductance into the system. In this way, the p-GaMnAs/n-GaAs wires are equivalent to ladder type LC transmission line that supports soliton propagation.

We will report on how we fabricate the p-n wire and measure the wave propagation along the wire. We also report on the different modes of wave propagation as the GaMnAs/GaAs micro wires are magnetized. Results will be compared with theoretical results of KDV solitons.

2.2 Trials in an Electrical Transmission Line

In this subsection, we start with the equivalent circuit of the p-n wire that can model neuron nerves [15]. By combining it with the electrical transmission line that can support soliton propagation [63], we propose an improved electronic transmission line that can model neuron nerves as well as support soliton propagation. We also demonstrate the experimental results from the novel electronic transmission line.

2.2.1 Modelling the Nerve Fibres Using Electrical Transmission Line

In order to model pulse propagating along neuron nerves, a p-n wire was proposed in 2004 by A. Nogaret, et al [15]. An equivalent circuit of the p-n wire is shown in figure 2.1. In the circuit, resistors represent the axial resistivity along the nerve cell, diodes represent the nonlinear conductance across the membrane and capacitors mimic the membrane capacitance. In the figure, r is the resistance per unit length, c is the capacitance per unit length, and g is the conductance per unit length. The propagation of the pulse along the transmission line can be described mathematically by using Kirchhoff law.
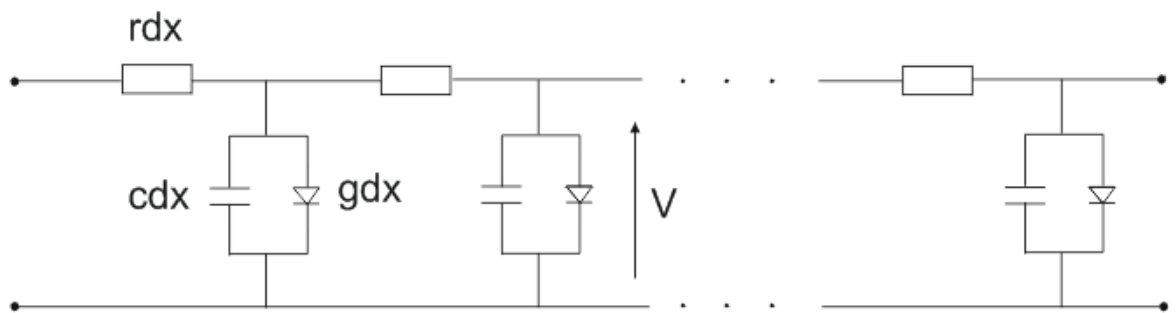

Figure 2.1 A transmission line circuit that represents the key electrical characteristics of the nerve fibre. In the circuit, the resistor mimics the axial resistivity of the capillary, the capacitor mimics the membrane capacitance, and the diode mimics the nonlinear conductance across the membrane [15].

The Kirchhoff voltage law shows that:

$$V(x) = rdxI(x) + V(x + dx) \tag{2.1}$$

The Kirchhoff current law gives:

$$I(x + dx) = I(x) - gdxV(x + dx) - cdx\frac{dV(x+dx)}{dt} \tag{2.2}$$

Since the length of each node is small, the distance x is small. We can deduce the equation (2.3) and (2.4) below

$$rI(x) = \frac{V(x)-V(x+dx)}{dx} = -\frac{\partial V}{\partial x} \tag{2.3}$$

$$\frac{I(x+dx)-I(x)}{dx} = -gV(x+dx) - c\frac{\partial V(x+dx)}{\partial t} \tag{2.4}$$

Combining the equation (2.3) and (2.4) gives:

$$-\frac{1}{r}\frac{\partial^2 V}{\partial x^2} = -gV(x+dx) - c\frac{\partial V(x+dx)}{\partial t} \tag{2.5}$$

Thus rearranging shows that the equation governing the transmission line is:

$$\frac{\partial^2 V}{\partial x^2} - rgV = rc\frac{\partial V}{\partial t} \tag{2.6}$$

This result can be compared directly to the one dimensional diffusion equation with decay, given below in equation (2.7):

$$D\frac{\partial^2 c}{\partial x^2} - Kc = \frac{\partial c}{\partial t} \tag{2.7}$$

Where both D and K are constants, D is the diffusion coefficient, and K is the decay constant.

The comparison between the equation (2.6) and (2.7) indicates that the transmission line should show diffusive behaviour. The pulse propagation along it will decay due to the resistance of the circuit. Therefore the transmission line in figure 2.1 shows only diffusive behaviours that can be described by a linear function. To induce the soliton propagation, we will need a nonlinear wave function which possesses soliton solutions [62, 64].

2.2.2 Soliton Propagation along a Nonlinear Electrical Transmission Line

In order to demonstrate KDV solitons, a transmission line as shown in figure 2.2 was built by Kuusela et al [61]. Electrical solitons were found in it. This is a ladder type LC circuits containing constant inductors and voltage-dependent capacitors. In the figure, L denotes the constant inductance. $C(V)$ denotes the nonlinear capacitance. V_{n-1} and V_n denote the

voltage propagating along the transmission line. I_n and I_{n+1} denote the current flowing along the transmission line.
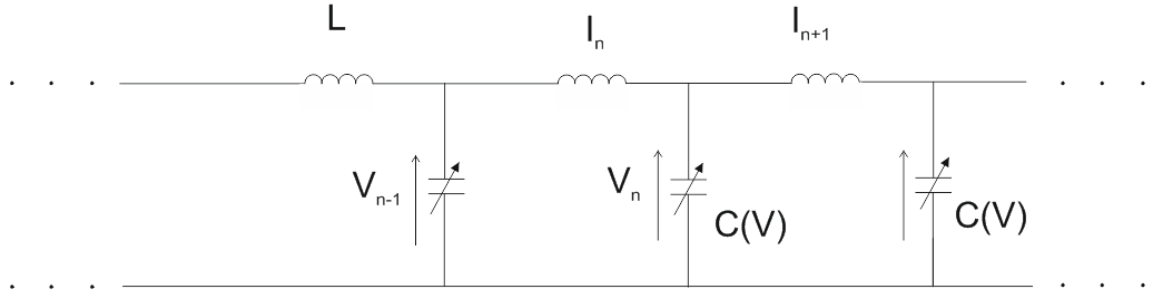
Figure 2.2 A discrete transmission line with constant inductions and voltage dependent capacitances [63]. The electrical solitons have been found in this transmission line. In the figure, L is the inductance. C (V) is the nonlinear capacitance. V_{n-1} and V_n denote the voltage across the transmission line. I_n and I_{n+1} denote the current flowing along the transmission line.

Each block in the transmission line can be described by the following equations:

$$V_{n-1} - V_n = L\frac{\partial I_n}{\partial t} \tag{2.8}$$

and

$$I_n - I_{n-1} = \frac{\partial Q_n}{\partial t} \tag{2.9}$$

Where Q_n is the charge stored in the nth capacitor.

Then we assume that over a given voltage range $(V_0, V_0 + V_n)$ the differential capacitance $C(V_n)$ can be approximated by

$$C(V_n) = \frac{Q(V_0)}{F(V_0) - V_0 + V}, \tag{2.10}$$

Where Q (V_0) and F (V_0) are parameters depending on V.

The equations (2.8)-(2.10) result in the following equation in terms of V[63],

$$LQ(V)\frac{\partial^2}{\partial t^2}\log\left(1 + \frac{V_n}{F(V_0)}\right) = (V_{n+1} + V_{n-1} - 2V_n) \tag{2.11}$$

The equation (2.11) is equivalent to the equation for the one dimensional Toda lattice [65], which is known that it has a stable travelling wave solution. For the present transmission line, the solution can be written as [61]

$$V_n(t) = F(V_0)\Omega^2 sech^2(\Omega v_0 t - Pn) \tag{2. 12}$$

With the velocity of the propagating wave

$$v_0 = \frac{1}{\sqrt{Lc(V_0)}} \tag{2. 13}$$

The solution to equation (2.11) has the same form with the solution of KDV equation, which is considered as the prototype of nonlinear differential equations having solitons. KDV can be written in the form of nonlinear equation

$$\frac{\partial u}{\partial t} - 6u\frac{\partial u}{\partial x} + \frac{\partial^3 u}{\partial x^3} = 0 \tag{2. 14}$$

With boundary conditions $lim_{z \to \pm\infty} u(z) = 0$, the equation has a solution as shown below [63]:

$$u_1(x,t) = -\frac{1}{2}a^2 sech^2(\frac{a(x - x_0 - a^2 t)}{2}) \tag{2. 15}$$

The solution (2.15) is a pulse shaped solitary wave with a velocity a^2 proportional to the amplitude and a width a^{-1} inversely proportional to the square root of the amplitude [61]. It suggests that in this system, larger amplitude solitons travel faster and are narrower than the smaller amplitude ones. This is the basic property of the KDV soliton. Another important property is that initial pulse decomposes into a set of solitons and a decaying background tail.

Comparing the equation (2.12) with (2.15), the equation (2.12) is a soliton solution. It indicates that the soliton wave can propagate through the LC transmission line.

In the ladder type LC transmission line shown in figure 2.2, the nonlinearity arises from the voltage dependent capacitance and the dispersion is related to both inductance and capacitance. If there is a particular waveform that causes the nonlinearity and dispersion in the system to exactly counteract each other, then the waveform will be able to propagate through the transmission line without changing shape. This is how the electrical soliton acquires a stable shape.

2.2.3 The Improved Electrical Transmission Line and Experimental Results from the Transmission Line

By combining ideas in circuits of figure 2.1 and figure 2.2, we propose an improved transmission line by incorporating inductance in the circuit of figure 2.1. In this way, we expect to obtain a transmission line that can model biological nerve fibres as well as

support the propagation of soliton. The improved transmission line is shown in figure 2.3. The capacitor represents the membrane capacitance. The conductor represents the conductance across the membrane. The resistor represents the axial resistivity along the nerve fibre. The inductor is for inducing inductance into the system. The inductance together with the nonlinear conductance provides the possibility of the propagating soliton wave through the line.

We built the improved transmission line on a prototype board. It is a repeated RLCG circuit consisting of twenty nodes. To keep the measurement easy, we do not want the travelling speed of the pulses too fast. According to the equation (2.13), big values of inductance and capacitance result in small speed. We then use capacitors of $1\,\mu F$ and inductors of 1mH because they have relative bigger values. We use BAT48 diode to provide nonlinear conductance because it has small leakage current.
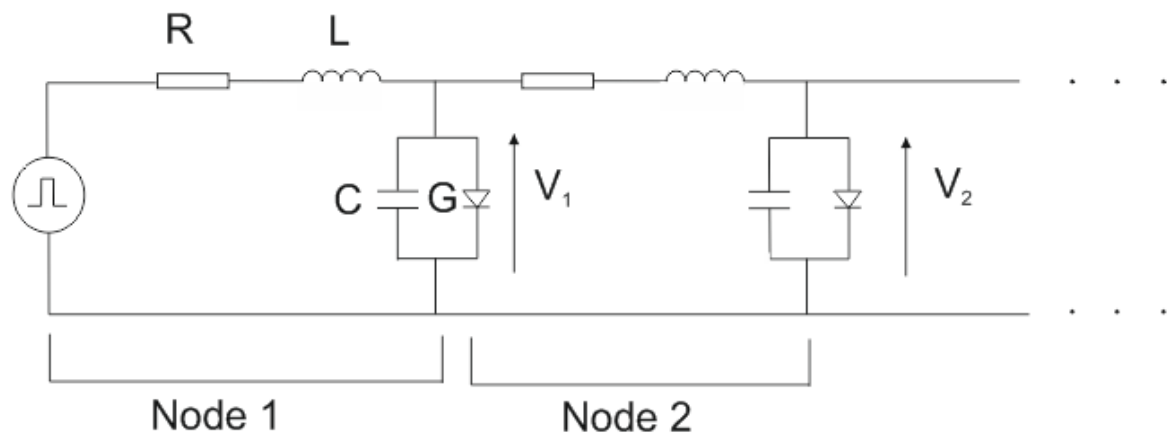
Figure 2.3 Schematic diagram of the transmission line for modelling the electrical characters of the nerve fibres as well as propagating the soliton wave. In each node, the conductor ($1\,\mu F$) mimics the membrane conductance (1mF), and the diode mimics the nonlinear conductance across the membrane. The resistors in figure 2.1 were removed for reducing the pulse decay along the line. The inductor together with the nonlinear conductance results in the dispersion and nonlinearity in the system. The balance between nonlinearity and dispersion will lead to the propagation of soliton waves. A rectangle pulses is fed into the circuit as the initial pulse.

After building the improved electrical transmission line, we measured pulse propagating along the line in order to find out if soliton can propagate along the line as proposed. Square pulses were fed into the first node of the circuit by a data acquisition (DAQ) card

controlled by the LabVIEW program. The electrical measurements from every other node were collected by the DAQ card.

The widths of input pulses have a significant impact on the morphologies of the output pulses. Figure 2.4 shows how the profiles of the propagated pulses vary as the widths of the input pulses are changed. Pulses in (a), (b) and (c) are collected from the first node of the transmission line and correspond to the input pulses with widths of 250 μs, 10 μs and 5 μs. When an input pulse as wide as 250 μs is used, the propagated wave displays a pulse profile very similar to that of the square input pulse and the pulse packet does not demonstrates the characteristic shape of a soliton. As the widths of the input pulse are decreased, profiles of the output pulses look more like a soliton. This is because in the circuit, the impulse response time is determined by the RC time constant. The width of the input pulse should be comparable to the time constant. $c = 10^{-6}F$, R is provided by the intrinsic resistance of inductors. The estimated value of the time constant is several μs. According to the experiment results, the best output profile result from the input of 5 μs. Therefore all experiments described later in this chapter use input pulses with 5μs pulse widths.
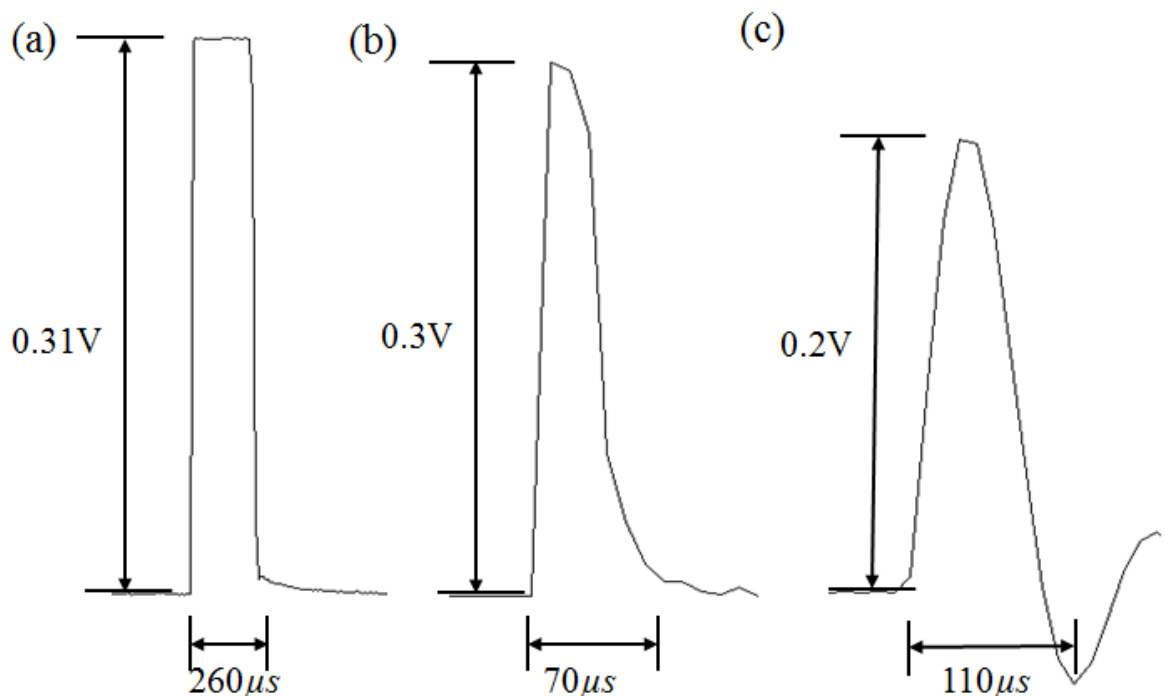
Figure 2.4 A plot to show the measured wave profiles of propagating waves created by input pulses with widths a) 250 μs, b) 10 μs and c) 5 μs. The amplitude of the input pulse is 2V. All the measured wave profiles are all collected from node 1 of the transmission line shown in figure 2.3.

Figure 2.5 plots profiles of the propagated pulses, which shows soliton-like characteristics: the input square wave decomposes into a large pulse shaped soliton wave before further decomposing into a set of smaller pulse shaped waves and a decaying background 'tail'. Also, it can be observed that the propagating waves show decay in amplitude, demonstrating the diffusive behaviour discussed in equation (2.6). This could be attributed to the intrinsic resistance of the inductors in the circuit. At node 20, a pulse that is bigger than the pulse from node 19 is observed. It could be due to the interference of the incoming pulse with the pulse reflected at the end of the transmission line. The amount of reflection can be tuned using a shut resistor at the end of the line.
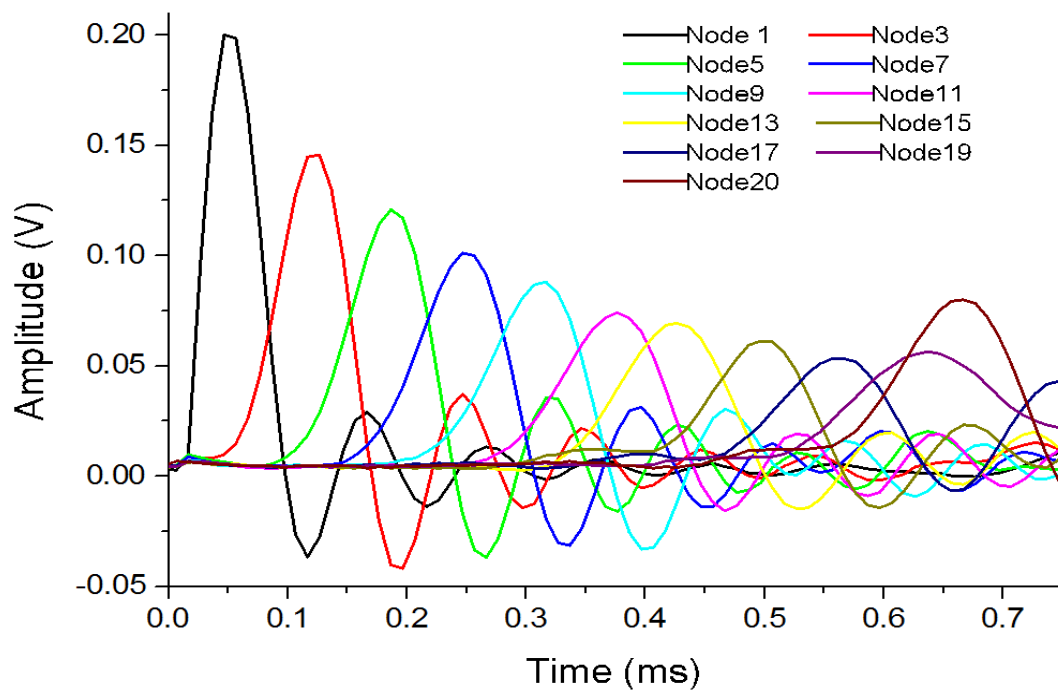
Figure 2.5 The measured wave profiles of wave propagating through the transmission line shown in figure 2.3. The amplitude of the input signal is 2V and the width of the input signal is 5 μs.

To further test for the propagation of solitons in the transmission line, the speed of the propagating waves is measured. As indicated in the equation (2.13), the speed of the propagating soliton wave should be equal to $\frac{1}{\sqrt{LC}}$ node/s, where L is the inductance and C is the capacitance in each node. Since we are using the capacitor of 1 μF and the inductor of 1mH, thus

$$v_0 = 3.2 \times 10^4 node/s \qquad \text{(2. 16)}$$

The real speed of the waves propagating through the transmission line can be calculated by measuring the time it takes for the wave to travel from the measurement point of one node to that of an adjacent node. The gradient of the curve would be equal to the average speed. This is shown in figure 2.6 below. For these measurements, the time of reaching each node is obtained from wave propagation plots as shown in figure 2.5. We varied the amplitudes of inputs in order to vary the amplitudes of output waves. For KDV solitons, usually bigger amplitudes correspond to bigger velocity. However, the linear trend lines shown in figure 2.6 indicate that all of the measured pulses propagate along the transmission line with a constant velocity. The average velocity of each pulse was calculated and is always 3.05×10^4 nodes/s. This value matches the theoretical value obtained in (2.16), showing only a small deviation from the theoretical value.
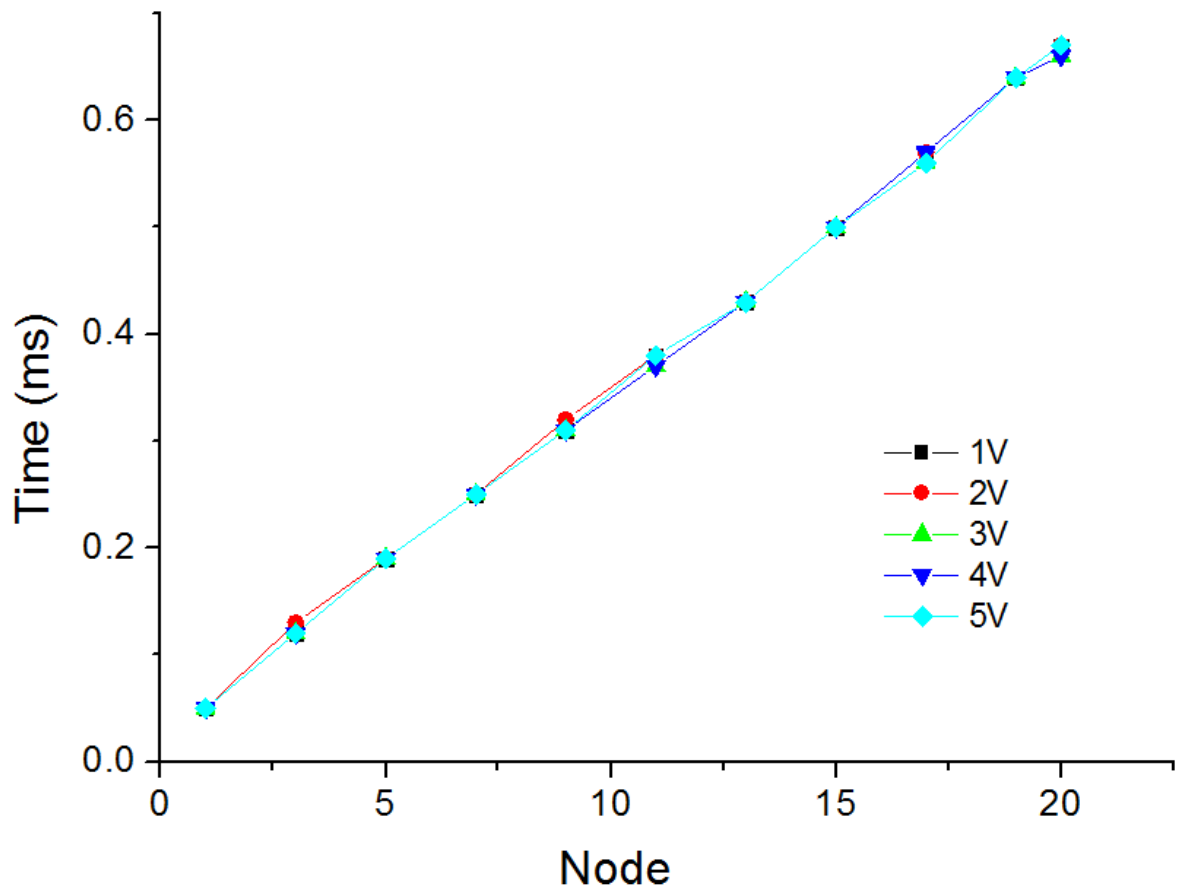
Figure 2.6 Plot of the time taken to reach each node for input pulses of varying amplitudes. All the data points in this plot are obtained from peak values of pulses in figure 2.5. The gradient of the curves plotted indicate the speed of the propagating waves, which is 3.05×10^4 node/s.

As indicated by the equation (2.15), there should be a strong link between the height and the width of the propagated pulses. Waves with larger amplitudes are narrower than waves with smaller amplitudes. In order to test this relationship, the full width at half maximum of propagating waves of amplitude V along the transmission line was calculated from figure 2.5. Results are shown in figure 2.7. We take the data point from node 1 as an example to explain how it is obtained. The value of y axis is obtained by measuring the pulse width at which the pulse amplitude is equal to half of its maximum value. The value of x axis is obtained by calculating the inverse square of the maximum amplitude. It can be observed in the figure that low amplitude waves have a higher full width at half maximum, and are therefore broader than the high amplitude pulses. Conversely, the plot indicates that high amplitude wave has a narrower wave profile. This is a key aspect of soliton behaviour.
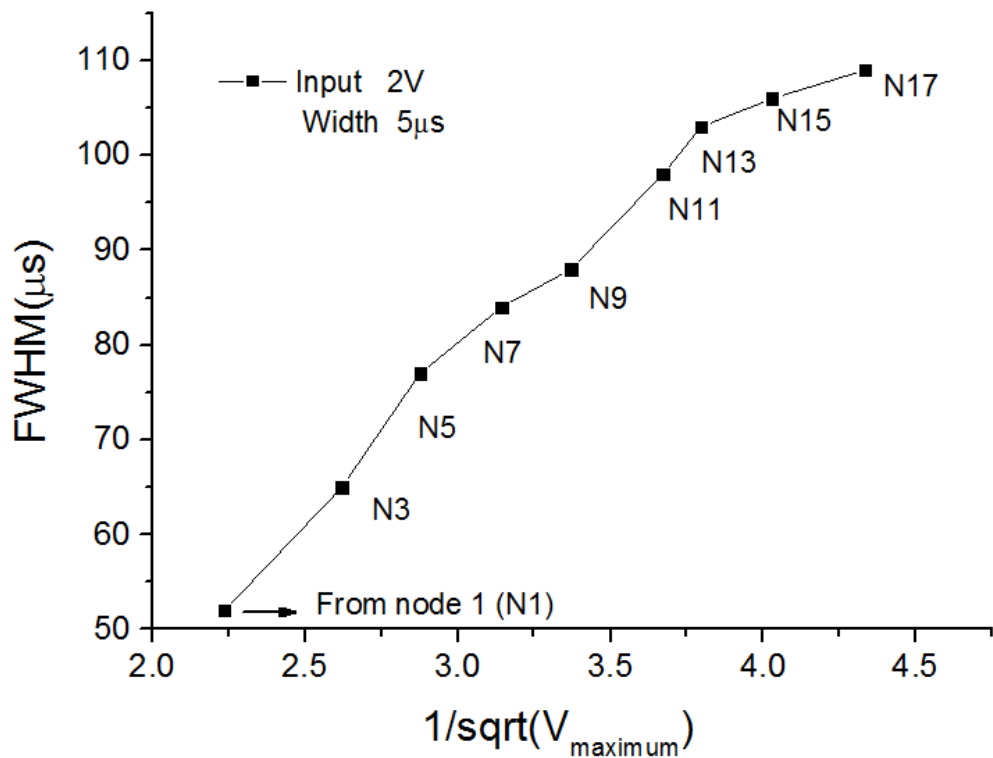
Figure 2.7 The full width at half maximum of amplitude of propagating waves plotted as a function of the inverse square root of the pulse amplitude. All the data points are obtained from pulses shown in figure 2.5. The curve in this plot indicates that low amplitude waves are broader than the high amplitude waves.

Results obtained from the electrical transmission line support the theory of soliton propagation. After the success in the circuit, we fabricated a micro transmission line according to the electrical properties of the circuit.

2.3 Micro Transmission Line Based on p-GaMnAs/n-GaAs Magnetic Semiconductor

In this subsection, we will demonstrate how we designed and fabricated the micro transmission line based on GaMnAs/GaAs p-n layers. The equivalent circuit of the p-GaMnAs/n-GaAs wire is the same with the improved transmission line shown in figure 2.3. Thus magnetic p-n wire can model neuron nerves and we expect to see soliton propagating along the wire.

2.3.1 The Design and Basic Parameters of GaMnAs/GaAs p-n Wires

The design diagram of the p-n wire is shown in figure 2.8. Structurally, the transmission line is designed to possess three function parts: dendrites, a soma and an axon because of previous research on spike regeneration [24]. The length of the transmission line is 5905.5 μs. Pairs of p type and n type electrodes are coupled across the line for us to feed signals into the line and measure the propagating signals along the line. In figure 2.8, the p type electrodes are marked by p_i (i=1, 2, 3…12) while the n-type electrodes are marked by n_i (i=1, 2, 3…12). Generally we use the first p-n pair p_1-n_1 to receive external signals. The distances from the first p-n pair to the nth pair are shown in table 2.1.
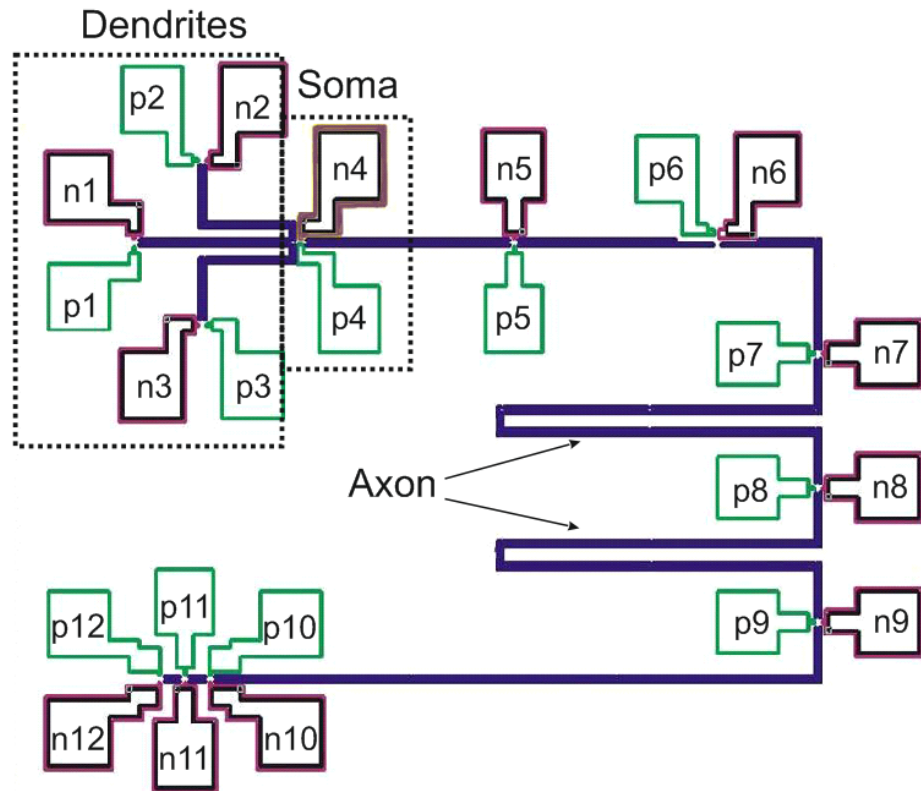
Figure 2.8 The designed structural patterns of the p-n wire. N type and p-type electrodes are coupled across the line. The contacts represented by p_i (i=1, 2, … 12) are p-type. The contacts represented by n_i (i=1, 2, …12) are n-type. The p-n wire has three dendrites terminated by contact pairs p_1-n_1, p_2-n_2, p_3-n_3, a soma connected with the contact n_4-p_4 and an axon showing eight contact pairs: p_5-n_5, p_6-n_6, … p_{12}-n_{12}. The length of the transmission line is 5905.5 μm. The width of the transmission line is 1.5 μm.

$D_{1 \to n}$(the first and the nth p-n pair)	Distances (μm)
$D_{1 \to 2}$	635.7
$D_{1 \to 4}$	310
$D_{1 \to 5}$	721
$D_{1 \to 6}$	1118
$D_{1 \to 7}$	1518
$D_{1 \to 8}$	3017
$D_{1 \to 9}$	4516
$D_{1 \to 10}$	5815.5
$D_{1 \to 11}$	5860.5
$D_{1 \to 12}$	5905.5

Table 2.1 Distances between the first p-n pair and the nth p-n pair.

A transmission line is made from the depletion region of a p-n junction. P-n junctions for fabricating the p-n wire were grown by a molecular beam epitaxy (MBE) in the group of Prof. Daniel Park at Seoul National University. We used two pieces of samples: sample A and sample B. They are grown under the same conditions. The layer structures of them are shown in figure 2.9. The figure show that the layer of (Ga, Mn)As is p-type and the thickness of this layer is 60 nm. The layer of Ga(As, Si) is n-type and the thickness of it is 50nm. To fabricate the n-type electrode, 80 nm of layers above the n-type layer will need to be removed in order to reach the n -type layer.
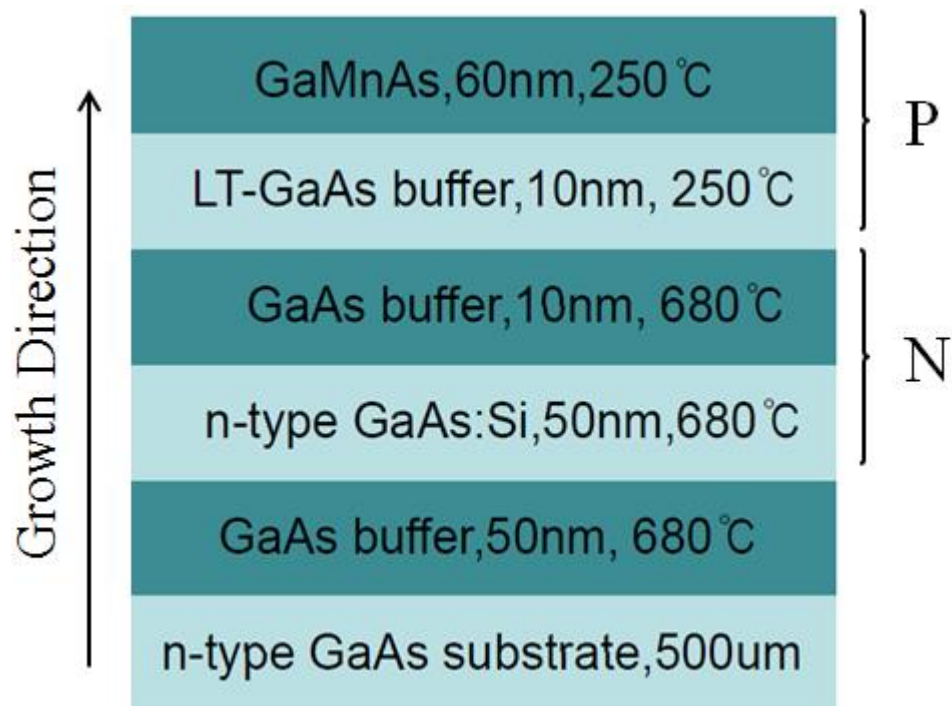
Figure 2.9 The layer structure of p-n junctions grown by MBE.

Important parameters of p-n junctions include the I-V curves and capacitance. I-V curves indicate the onset voltages of p-n junctions. And based on the equation 2.13, the capacitance is related with the propagation speed of waves along the p-n wire.

I-V curves of the p-n junction sample A and sample B are shown in figure 2.10. They indicate the onset voltages. For sample A, the onset voltage is about 0.7V. For sample B, the onset voltage is about 1V. After the fabrication, *IV* curves of p-n pairs on p-n wire samples will be measured again. We do this for two reasons. First, the measurement of *IV* curves can exam the quality of p-n pairs. We need to separate p-n pairs which possess

exponential conductance from the ones which have linear conductance because of the unsuccessful fabrication. Second, we need to obtain an accurate onset voltage of an individual p-n wire sample. The amplitude of the voltage we apply on the p-n wire should be around the onset value to assure that the conductive channel is open but the current flowing across it is not too big to cause leakage. If there is current leakage across the transmission line, electrical pulses will not be able to propagate along the line.
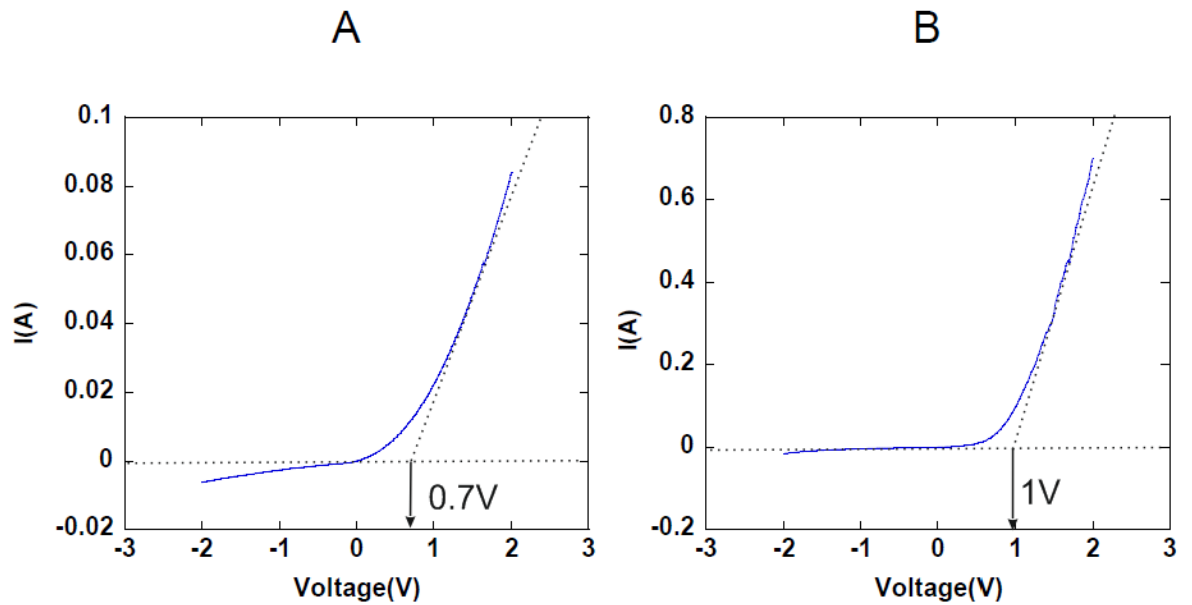
Figure 2.10 The I-V curves of p-n junction samples. They indicate the onset voltages of the junctions. The onset voltage of sample A is about 0.7V. And the onset voltage of sample B is about 1V.

In order to calculate the capacitance, we need to know some basic parameters, such as the carrier concentrations, etc. Based on the data sheets of samples, the values of carrier concentrations are shown in table 2.3.

Acceptor concentration N_A	$1 \times 10^{18} \ cm^{-3}$
Donor concentration N_D	$6 \times 10^{20} cm^{-3}$
Intrinsic carrier concentration N_i	$2.1 \times 10^6 \ cm^{-3}$

Table 2.2 Values of carrier concentrations.

According to these parameters, we now start with calculating the built in potential[66]

$$V_{bi} = \frac{kT}{q} ln \left(\frac{N_A N_D}{N_i{}^2} \right) = 1.56V \qquad (2.17)$$

The width of the depletion region is[66]:

$$d = \sqrt{\frac{2\varepsilon_r \varepsilon_0}{q} \frac{N_A + N_D}{N_A N_D}} V_{bi} = 47.2nm \qquad (2.18)$$

Then the capacitance of the wire per unit length is[66]:

$$c = \frac{\varepsilon_r \varepsilon_0 w}{d} = 3.62 \times 10^{-9} F/m \qquad (2.19)$$

Where w is the width of the p-n wire, ε_0 is the permittivity in free space, and ε_r is the permittivity in GaAs.

2.3.2 The Fabrication Process of the p-n Wire

All the fabrication work in this subsection was done by me in David Bullet nanofabrication laboratory in university of bath.

The aim of the fabrication is to make p-n wires with structures shown in figure 2.8 by using p-n layer samples shown in figure 2.9. The processes of the fabrication include photolithography, etching, thin film deposition and lift off. First lithographic steps are carried to make proper patterns on p-n layer samples. After that, Zn (30nm)/Au (150nm) will be deposited on p-type mesas in order to form p-type Ohmic electrodes while n-type mesas need to be etched to an appropriate depth of 90nm to reach the n type layer. Then Ti (30nm)/Au (150nm) will be deposited on the n- type mesa to form the n-type electrodes. Finally it is the lift off process. During this process, the rest of the resist will be washed away with the metallic layer attaching to it while the metallic layer bonded to the sample directly will stay. All the fabrication processes are performed in the David Bullet Nanofabrication Lab.

The process of photolithography consists of the following steps: firstly, the samples are cleaned with acetone and isopropanol. Any particle that lies on top of sample may result in failure of the photolithography process. Secondly, s1813, which is a positive photoresist, is spin coated uniformly on the sample surface. With spinning speed of 4000 rpm, a resist with the thickness of 1.4 μm can be achieved. Thirdly, if samples are going to be etched, they will be moved to a 90°C oven and baked for 30 minutes after spin coating; if samples are going to be prepared for metal deposition, they will then be moved to a

90℃ oven for fifteen minutes, dipped in chlorobenzene for three minutes and then baked for further fifteen minutes in order to harden the top surface of the resist and help with the lift off. The fourth step is placing samples into mask aligner for UV light exposure for roughly nine seconds. In this step, a chrome photo mask possessing the patters as shown in Fig. 8 is designed and used. The resolution of the mask is 0.1 μm. It is far better than the resolution of the mask aligner which is limited by diffraction of light, contact of the mask and the wafer, size of the pattern, etc. The fifth step is dipping exposed substrates in photoresist developer in order to remove the unnecessary resist. We use 351 solution (351: water=1:3.5) as the photoresist developed. The proper developing time is important. Insufficient developing time will leave unwanted resist on the sample. A longer development time will damage the resist structure. Various development times were tried and 40 seconds developing time provided the best pattern.

The process after the photolithography is wet etching for exposing the n-type mesa. The acid solution (NH_3OH: H_2O_2: H_2O=50:1:1) are used as etchants. A test sample will be needed for testing the etching rate. Profiles of the test sample before and after it is dipped into the acid solution for ten seconds are measured by stylus profiler. Thus the removed depth is obtained. The etching rate equals to the etching depth divided by the etching time. Theoretically, n type mesas can be reached after 80 nm is removed. However, it is difficult to get homogeneous as well as accurate etching depth by wet etching. If the removed thickness of some parts of the samples is less than 80nm, p-type and n-type electrodes can contact each other and result in short circuit. Therefore, we set 90 nm as the target thickness that is going to be removed to avoid this problem. After being etched, photoresist is washed away by acetone. Profiles of the samples are measured by stylus profiler. It is shown that the real etching depths range is 90-100 nm.

The process after etching is metal evaporation for depositing thin metallic films on the p-type and n-type mesas in order to form the p-type and n-type Ohmic electrodes. Ti (30nm)/Au (150nm) and Zn (30nm)/Au (150nm) layers are deposited on the n- type and p-type mesas respectively. Here Zn/Au layers play the key rode in forming high quality Ohmic contacts because they can reduce the mismatch between the Fermi energy of the metal and semiconductor. Ti is a glue allowing Au to stick to GaAs. The thickness of the metallic layer is decided by calculating the deposition rate.

After the metal evaporation process, the sample was fully covered by a thin layer of metal film. Therefore the process of 'lift off' is needed in order to remove the unwanted metal and create structures on the sample surface. To perform the lift off process, the samples are put into a solvent that can wash away the metal film which has the sacrificial photoresist layer underneath. The selection of the solvent mainly depends on the type of photoresist. Acetone is used for the s1813. The samples are dipped into acetone at room temperature overnight.

Fabrication work is done after lift-off. As each sample contains numbers of cells, they were cut into small pieces. Each piece has only one cell. A micrograph of one cell from p-n junction sample A is shown in figure 2.11. The dark yellow colour of p type electrodes is due to the oxidization during deposition.
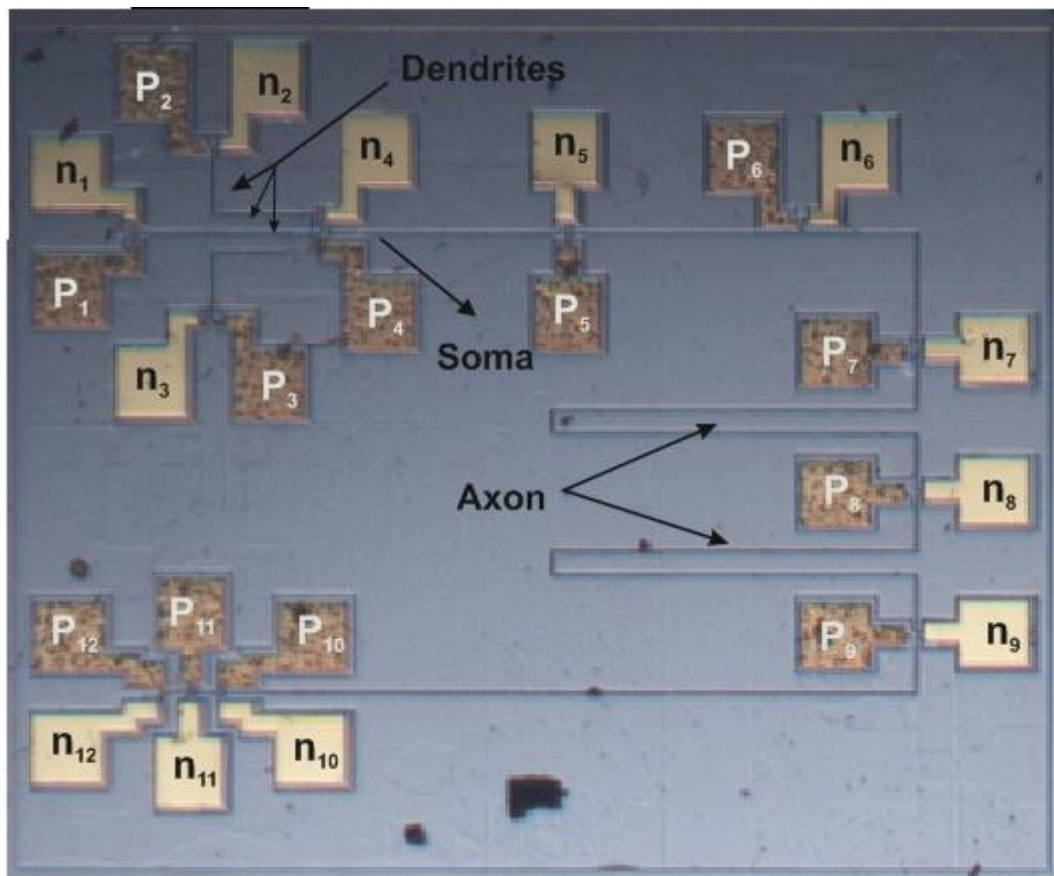
Figure 2.11 The micrograph of a fabricated p-n wire. The width of the wire is 1.5 μm. The length from p1-n1 to p12-n12 is 5905.5 μm. In the later measurements, we say each p-n pair is a contact.

The last process before measurements is the bonding work. Selected cells will be glued on chip package by epoxy. Bonding is used for connecting the electrodes of the cells with metal strips on the chip package. A corner of a well bonded sample is shown in figure 2.12.

Figure 2.12 A corner of a well bonded sample.

2.4 Characterization of the Micro Transmission Line

Soliton-like wave propagation is supposed to be the main function of our devices. In the experiments, we measure the pulse propagation along the p-n wire by feeding square pulses into the first p-n pair and collecting outputs from other p-n pairs. The process is carried out by using a programmed DAQ card. The card can generate a single rectangular pulse with set pulse width and amplitude.

All the results shown in subsections 2.4 and 2.5 are from the p-n wire sample A1, which is made from the p-n junction sample A, because it is the most successful sample.

As demonstrated in the subsection 2.2.3, in order to obtain the soliton like wave, the width of the input pulse should be comparable to the time constant of RC. The capacitance of the p-n wire has been deduced from the equation (2.17)-(2.19). The value of it is $3.62 \times$

$10^{-9} F/M$. The resistance per unit length is estimated by measuring the resistance along p type and n type metal strip lines, which are shown in figure 2.13. The resistance along the p-type strip line is higher than that along the n-type strip line. This can be explained by that in the semiconductor like GaAs, the n-type mobility is much higher than the p-type and therefore, p-type lines have higher resistance. Ideally, the resistance should increase with increasing distance. However, the real measured resistance is a combination of intrinsic resistance and contact resistance. The big contact resistance can lead to the linear negative correlation between the resistance and the distance. According to figure 2.13, we make a small estimated value and assume the intrinsic resistance is several tens of kΩ. Then the RC time constant should be several tens of μs. According to this estimation, we decide to use the input with pulse width of $50\,\mu$s.
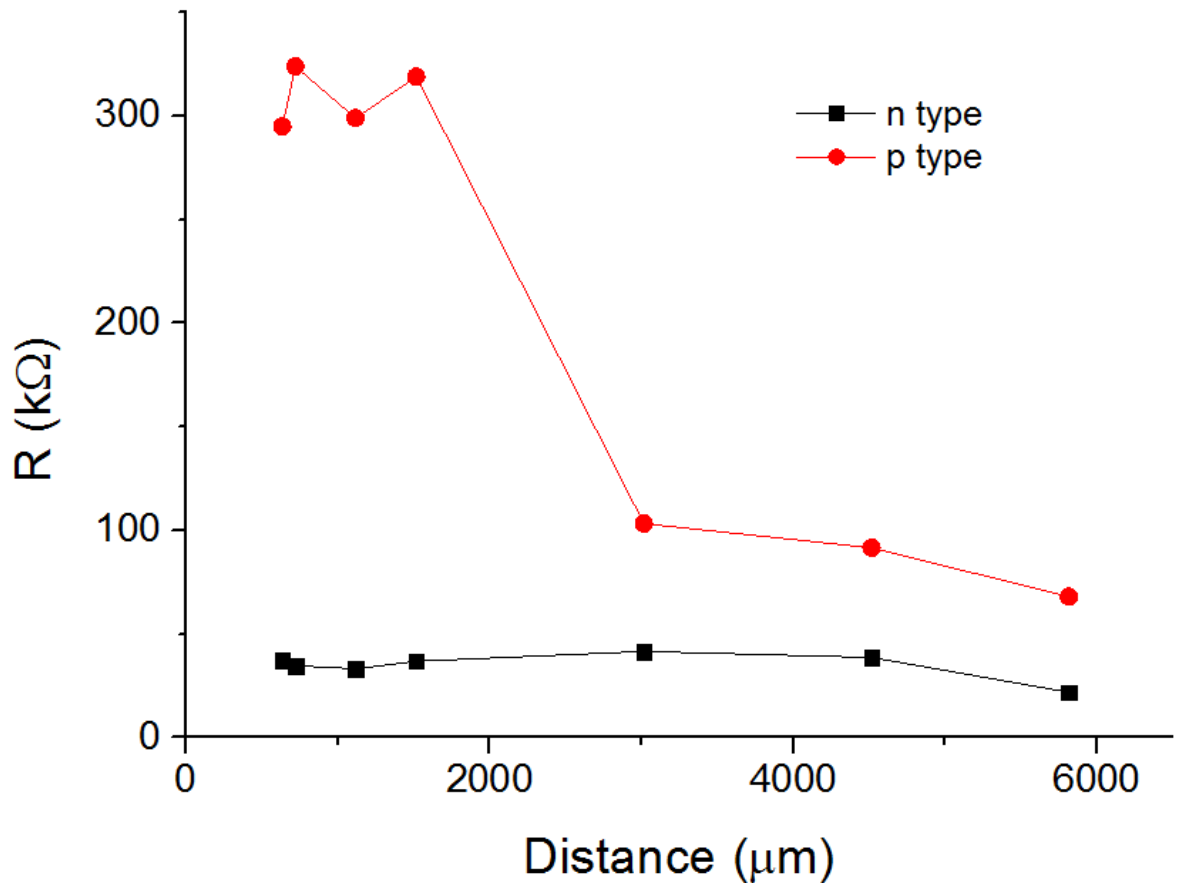
Figure 2.13 The resistance along p type electrodes and n type electrodes of sample A1.

The amplitude of the input pulse also matters. It should be big enough to be above the onset value of p-n pairs as well as small enough to avoid leakage current. In other words,

the amplitude of the input pulse should be around the threshold of the knee voltage of p-n junctions. Also, by measuring the I-V curves, we can know if samples have been damaged from the fabrication. Figure 2.14 shows the IV curve from a p-n pair of sample A1, which possesses the best quality. It indicates the onset voltage of the p-n pair is about 0.55V. According to the experiment design in 2.3.1, we need the value of the input voltage to be just above the onset voltage. We arbitrarily chose the value of 0.7V as the amplitude of the input pulse.

In comparison to the onset voltage of p-n junctions, the onset voltage of p-n pairs on the p-n wire is smaller. This is due to the diffusion of Mn induced by heat during the fabrication. The diffusion of Mn leads to the increase of conductivity.
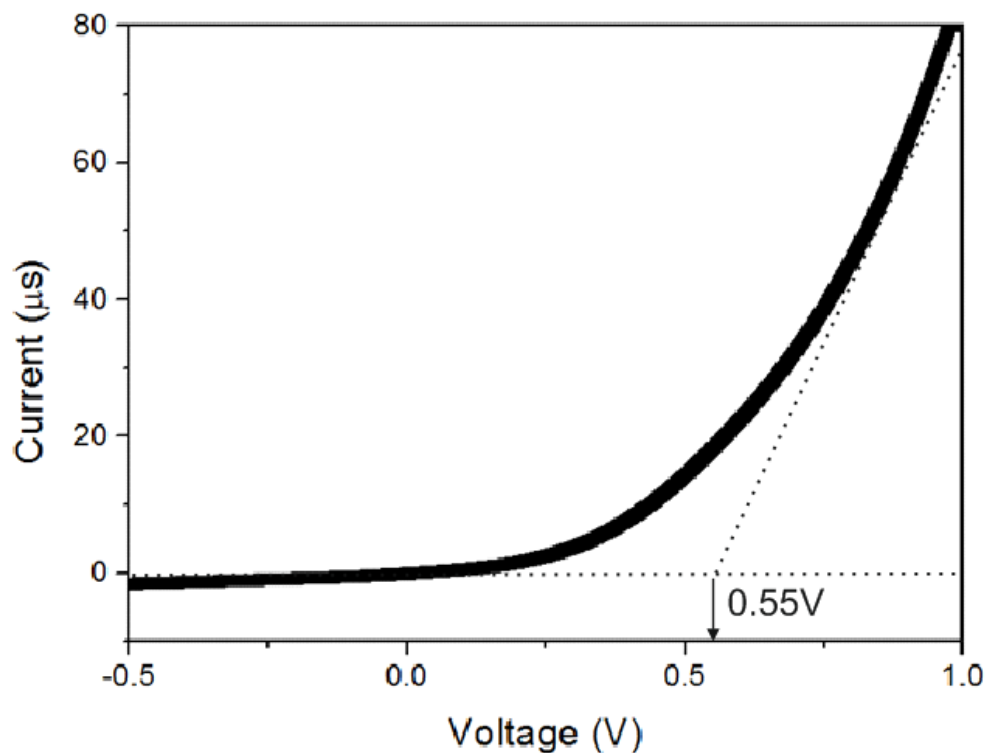
Figure 2.14 The I-V curve from the sixth p-n pair of sample A1.

2.5 Results from the Micro Transmission Line

In this subsection, we will show the wave propagation along the p-n wire at room temperature without and with applied magnetic field. We will characterize the propagating wave by calculating the propagating velocity, full width of the propagating pulse at half maximum as a function of propagating distance, etc. to demonstrate that it possesses

soliton properties. We will also demonstrate the influence of the magnetic field on the wave propagation by changing the tilt angle of the magnetic field.

We start with discussing the pulse propagation along the GaMnAs/GaAs micro p-n wire when there is no external magnetic field. The wave propagation is shown in figure 2.15. In the figure, the first rectangular pulse is the initial pulse. It is fed into the wire at the first p-n pair, say contact 1. Outputs are collected from the contact 2, 5, 6, 7, 8, 9 and 10. Along the wire, the initial pulse is transformed into an oscillatory wave train of gradually increasing width and decreasing amplitude. The decreasing amplitude is due to the resistivity to the pulse propagating along the transmission line. And the spreading out behaviour indicates that the system is dispersive.
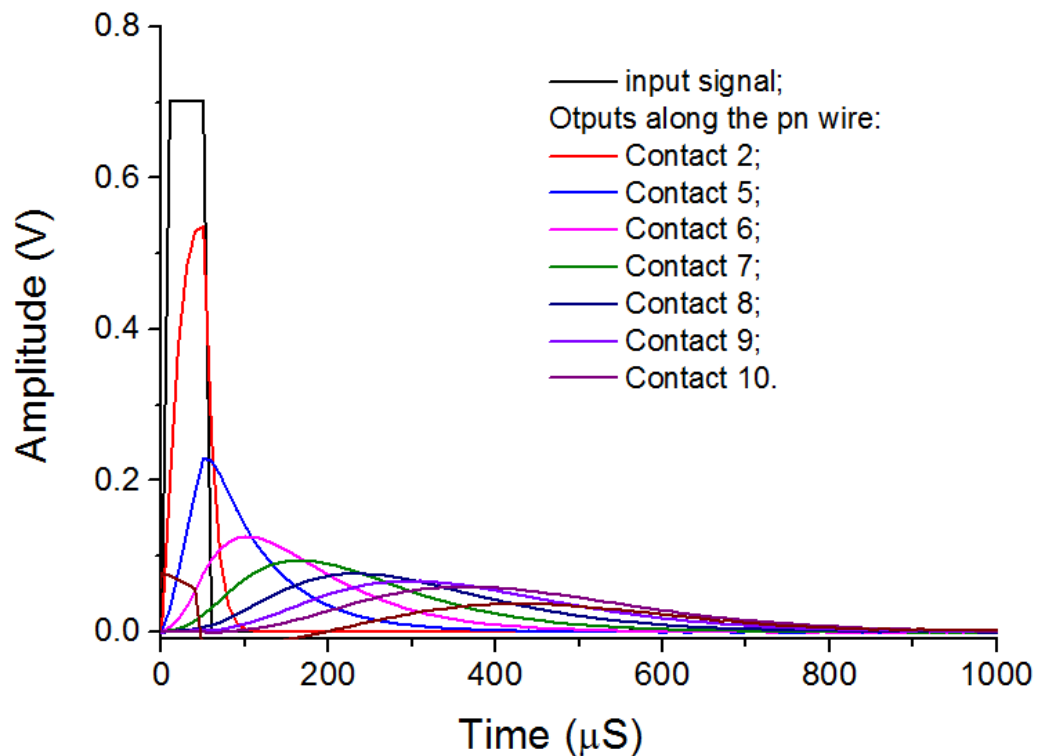
Figure 2.15 Pulse propagation along the micro p-n wire sample A1. There is no magnetic field applied to the sample. A square input pulse is fed into the first contact pair. The width of the input pulse is $50\,\mu s$. The amplitude of the input pulse is 0.7V. And pulses propagating along the wire are collected from contact pair 2, 5, 6, 7, 8, 9 and 10.

The travelling distance of the wave as a function of time is shown in figure 2.16. The points are obtained from figure 2.15 by recording at what time the propagating pulse arrives at each contact. The trend is nearly like linear and it is shown by the dash line in the

figure. It indicates that the wave is travelling at a constant velocity of 16.8 m/s. We tried initial pulse with various amplitudes and various pulse widths. They have influence on the amplitude and pulse widths of the travelling wave but lead to the same travelling speed.
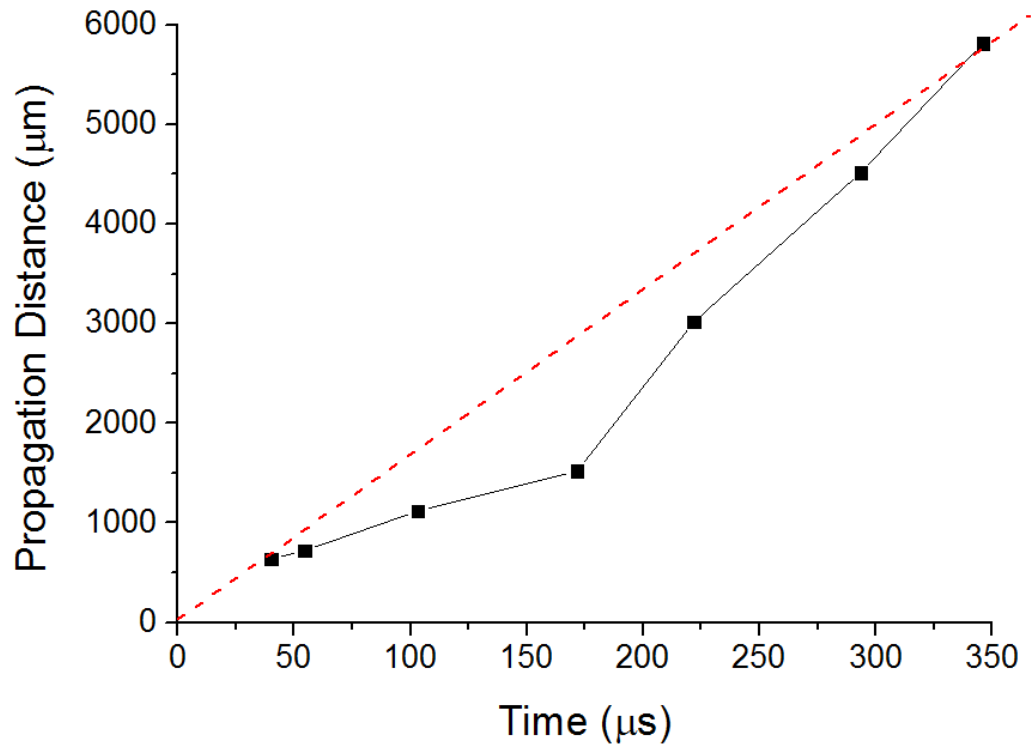
Figure 2.16 Pulse time delay plotted as a function of the distance from the first contact. The black symbols are measured results. The dashed line indicates the linear trend of the black trace.

The full width at half maximum of propagating waves of amplitude V along the transmission line is calculated from figure 2.15. Results are shown in figure 2.17. It can be observed in the figure that during the propagation, low amplitude pulses have a higher full width at half maximum, and are therefore broader than the high amplitude pulses. Conversely, the figure indicates that high amplitude pulse has a narrower pulse profile.
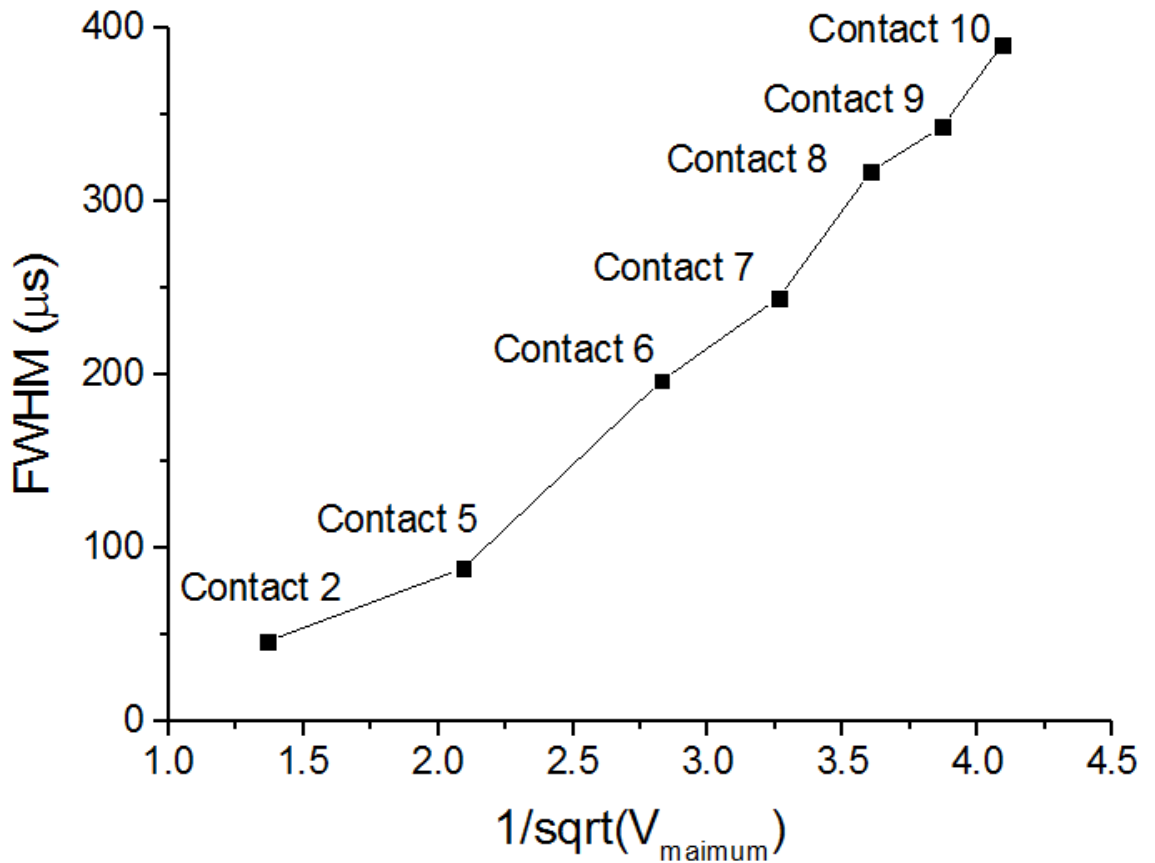
Figure 2.17 The full width at half maximum of amplitude of propagating waves as a function of the inverse square root of the pulse amplitude. The contact from which the data point was obtained is marked in the plot.

Then magnetic field of 0.06T is then applied to the sample to test the influence of magnetization on the pulse propagation.

In figure 2.18, the micro p-n wire is magnetized perpendicular to the long axis. In this plot, pulse propagation can be detected on contact 2 and contact 5. The pulses totally disappear after that. This indicates a stronger decay during the propagation. At room temperature, the magnetic moments from Mn in GaMnAs lie in random directions and the material is paramagnetic. The external magnetic field is supposed to align the magnetic moments perpendicularly and increase the dispersion of the system. A stronger dispersion can break the balance between nonlinearity and dispersion in the system and lead to propagation pulses which are decaying quickly.
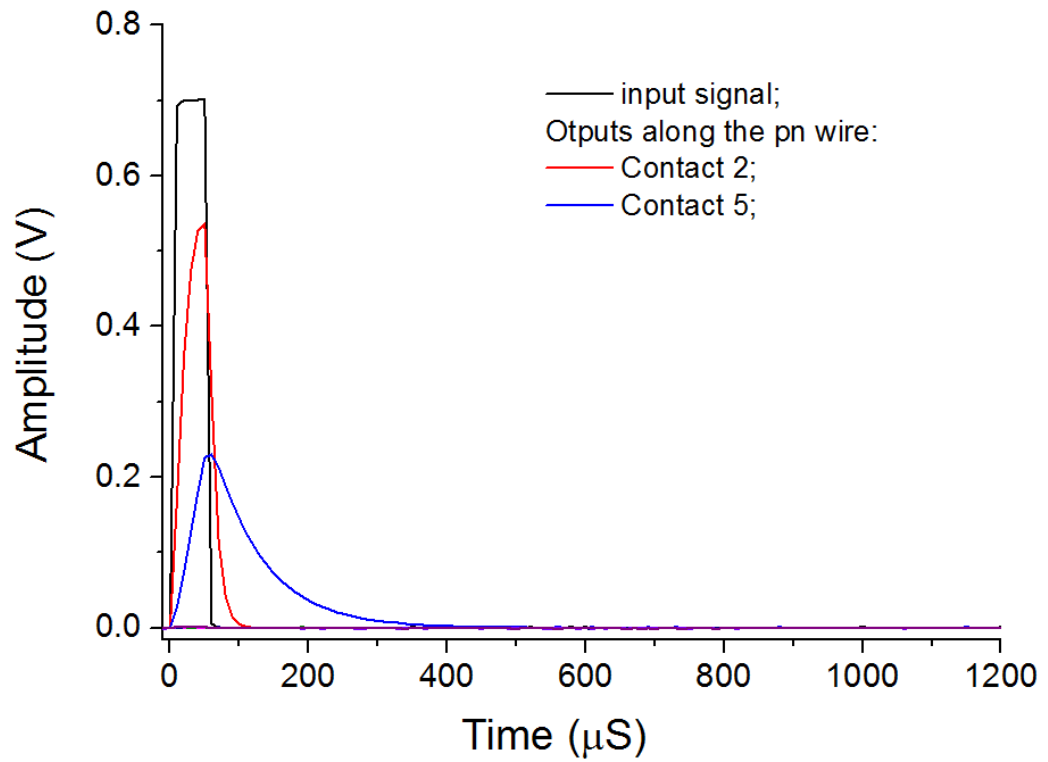
Figure 2.18 Pulse propagation along the transmission line when the micro wire is magnetized perpendicular to the long axis. The magnetic field applied on the sample is about 0.06T.

In figure 2.19, the tilt angle of the external magnetic field is changed from 90 degree to 45 degree to weaken the magnetization. It comes out that in this case, the pulse can propagate a longer distance comparing to that in figure 2.18.
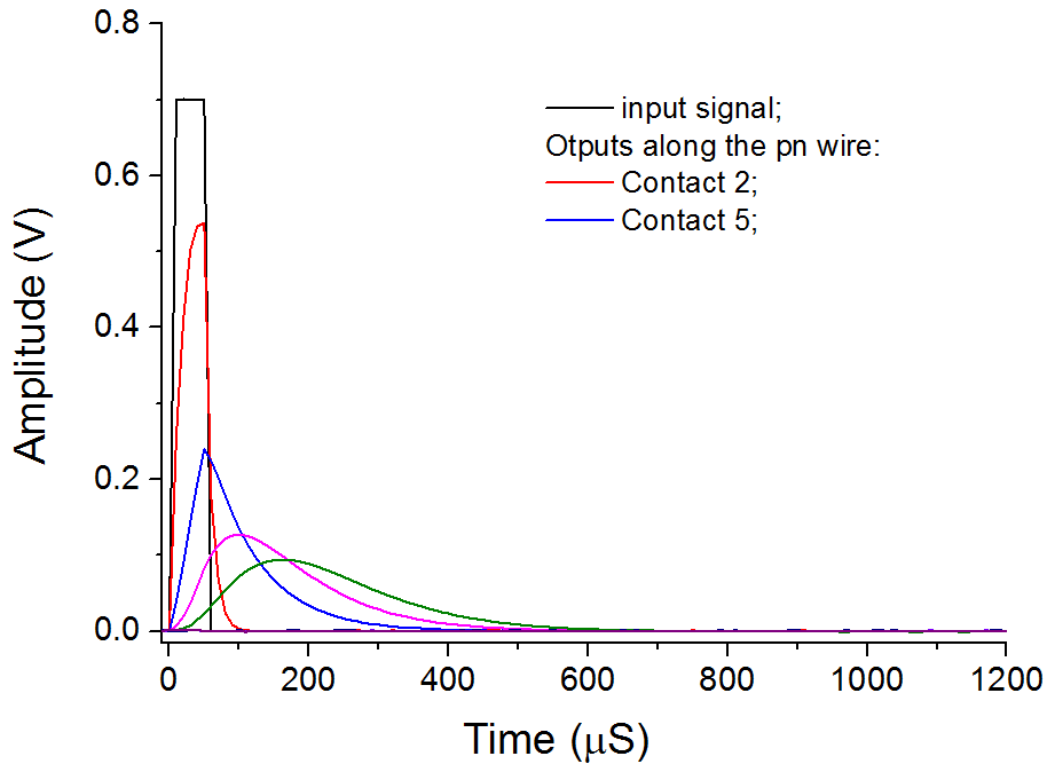
Figure 2.19 Pulse propagation along the transmission line when the magnetic field is tilted by 45 degrees to the normal.

2.6 Discussion and Conclusion

We have fabricated a p-GaMnAs/n-GaAs micro wire. The magnetic p-n wire can emulate physical properties of neuron membranes as well as model characteristics of electrical signalling along biological nerve fibres. Thus the p-n wire can be regarded as an artificial nerve fibre. Besides, there is both nonlinearity and dispersion existing in the magnetic p-n wire. The balance between them can lead to soliton propagation, which is a hypothesis in bio-membranes and nerves.

Experiments with the equivalent circuit of the magnetic p-n wire show two evidences on soliton propagating in the system. One is that the experimental value of propagating speed agrees to the theoretical value. And this value is determined by both the capacitance and inductance in the transmission line. The other is that during the propagation, larger amplitude pulses are narrower than the smaller amplitude ones.

We have also observed electrical wave propagating along the artificial nerve fibre at room temperature. During the propagation, pulses with larger amplitudes are narrower than

pulses with smaller amplitudes. This agrees to the key characteristic of a soliton wave. We have also obtained the experimental value of the propagating speed of waves through the wire. However, we did not manage to obtain the theoretical value because it is hard to calculate the value of inductance in the magnetic p-n wire.

In both the micro magnetic p-n wire and its equivalent circuit, the amplitude of propagating pulses decay along the transmission line. It does not agree to the common knowledge that soliton does not change its shape during propagation. This can be explained as two reasons. One is that we cannot avoid resistance in a real transmission line. Due to the resistance, the soliton measured in experiment differs from the idealized solitons and it decays. The other reason is that in the system, the balance between nonlinearity and dispersion is not perfect. If the dispersion is a bit stronger, it is reasonable that the wave decays and broadens while propagating.

External magnetic field is applied on the magnetic p-n wire and it leads to a strong decay of the propagating pulses. This is because the external magnetic field can align the magnetic moments perpendicularly and increase the dispersion of the system.

Chapter 3 Electronic Implementation of the Hodgkin-Huxley Model and Synaptic Links

3.1 Introduction

We produced an analogue neural network by interconnecting HH neurons with reciprocally inhibitory synapses. In this chapter we talk about how we implement the analogue neurons and electrical gap junction synapses.

As demonstrated in chapter 1, we choose the HH neuron model [17] because it is a suitable tool for quantitatively studying neural behaviours. This is a single compartment model that neglects the neuron's spatial structure and focus on how various ionic currents contribute to spike generation [12]. On one side, comparing with other spiking neuron models, it is accurate enough for replicating the spike generation in biological neurons in details [40]. On the other side, a network consisting of only six neurons is small enough for avoiding the complicated computation resulted from the accuracies of HH models. Also, a small neural network can keep the study simple and fabrication price low.

And analogue implementations are primary attractive to neural hardware developers because advantages of analogue devices, such as real-time operation, high processing speed, low power consumption, small size and easy incorporation, etc. can be incorporated into neural hardware [67].

The first successful analogue hardware of HH neurons is implemented by Mahowald and Douglas in 1991 [11]. They exploited the similarities of sigmoidal conductance-voltage relation between biological membranes and Metal-oxide-semiconductor field effect transistors (MOSFETs) [68] and built conductance-based single neuron circuits which are analogue approximations of HH neuron models. These circuits accurately reproduce the process of generating spikes with detailed control parameters by replicating the dynamics of ion channels. Benefits from this analogue neurons include: they are the most physiological meaningful which is important for neurostimulation [69]; moreover, these neurons are versatile in dynamic behaviours that it is possible to include additional ion channels to accurately describe the complex dynamics associated with the Calcium (L, T) currents or currents in real neurons, which gives rebound pulses and spike bursts not accounted for by the HH model. Finally, the parameters space of these neurons is quite

large which is important to 'program' them to replicate to the identical the dynamics of biological CPGs.

Because of the above benefits, we employed Mahowald and Douglas's neuron to build our neural network. However, here we only consider ion currents related to the nerve impulse itself, such as sodium current and potassium current. We do not consider ion currents for controlling impulse rate because we only need tonic spiking.

After building individual neurons, we then constructed circuits that are equivalent to synapses to link neurons together and form the neural network.

Synapses are gap junctions that enable a nerve neuron to be connected with another nerve neuron or effector cells. They allow neurons to form interconnected circuit networks within the nervous system. Functionally, they are dynamical nonlinear devices like neurons. They release the electrical or chemical transmitters from pre-synaptic membrane and act on the post- synaptic membrane. Pre-synaptic signals that drive the post- synaptic membrane toward threshold are said to be excitatory. Pre-synaptic signals that hold the post-membrane below the threshold are said to be inhibitory[70].

We connected the analogue neurons by electrical gap junction synapses. Compared with chemical synapses, the electrical ones are faster and support bidirectional transmission [71]. The electrical synapse works on the neurons by injecting currents into neurons. Determined by the current direction, a synaptic can either be excitatory or inhibitory. Here we use inhibitory synapse to achieve the winnerless competition architecture in the neural network because winnerless competition dynamic is crucial for our study of stimulus dependent spiking patterns in chapter 4. It can result from inhibitory connections between neurons [72, 73].

Single neurons linked by analogue synapses together allow the implementation of electronic spiking neural networks.

3.2 Electronic Implementation of the Hodgkin-Huxley Model

3.2.1 The Time Course of Biological Membranes

In this subsection, we show the voltage dependence of rate constants and the time course of potassium and sodium channels in HH neuron model [17]. This is crucial because we will need to model the correlation when implementing the neuron model in hardware.

Rate constants for potassium activation gate and sodium activation and inactivation gates as a function of membrane voltage have been shown in equations (1.15)-(1.20). We denote the steady-state open probabilities for the activation gate of potassium channel, the activation gate of sodium channel and inactivation gate of sodium channel by n_∞, m_∞, and h_∞. The steady state values as a function of relative membrane potential is shown in figure 3.1 below. All the lines are calculated from equations (1.15)-(1.20) and converted by the equation (1.7).

In figure 3.1, a positive V means the membrane is depolarized and a negative value means the membrane is hyperpolarized. The voltage dependence of rate constants of activation gate of both sodium channel and potassium channel is an exponentially increasing curve. This indicates the possibility of modelling the conductance by silicon components as transistors possess exponential IV curves.
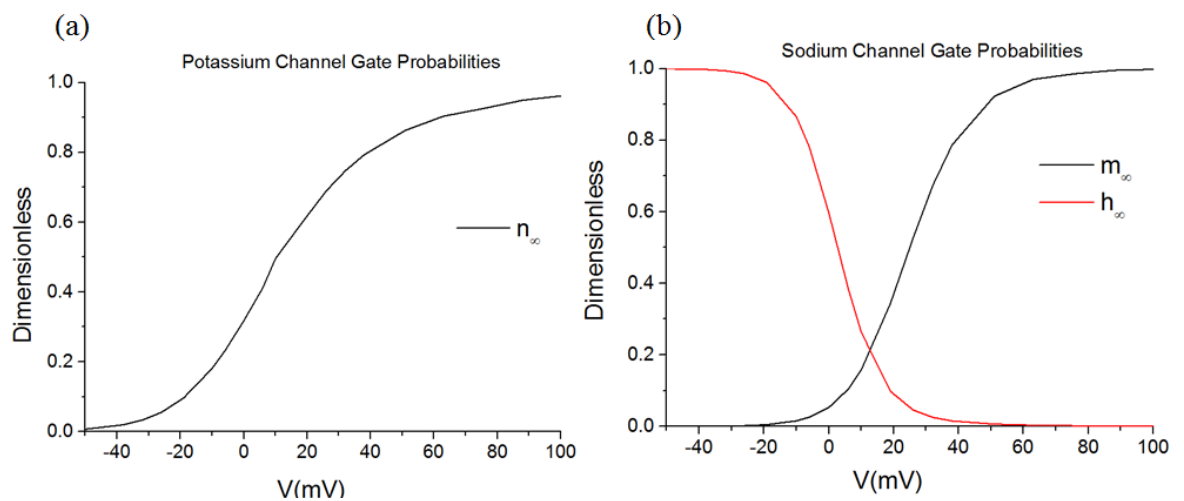
Figure 3.1 Steady-state gate probabilities of channels being open as a function of V. The resting potential is at $V = 0mV$. (a) Potassium channel gate probabilities; (b) Sodium channel gate probabilities. In this figure, all the line are calculated from equations (1.15)-(1.20) and (1.7). The equations are proposed by Hudgkin and Huxley in ref. [17] .

Besides the rate constants, the time constants of the gates of potassium and sodium channels that approch the steady state are also important parameters for us to model. The values of them are calculated from equations (1.15)-(1.20) and converted by the equation (1.8). They are shown in figure 3.2. At rest, τ_m is much smaller han the other other time

constants, approaximately 0.2ms compared to roughly 5.5 ms for τ_n and roughly 8.5 ms for τ_h. This means the sodium activation gate opens rapidly in response to depolarization compared to the other two gates. In addition, the time constants show the process of generating an action potential: when a sufficiently large stimulus is applied, the sodium activation gates will rapidly open and depolarize the membrane potential. This leads to the generation of an action potential. The potassium activation gate and the sodium inactivation gate lag behind this process by a few milliseconds. And when $V > 15mV$, τ_h drops below τ_n. Thus for depolarization greater than 15mV, $\tau_n > \tau_h > \tau_m$. This correlation is what we need to obtain in hardware.
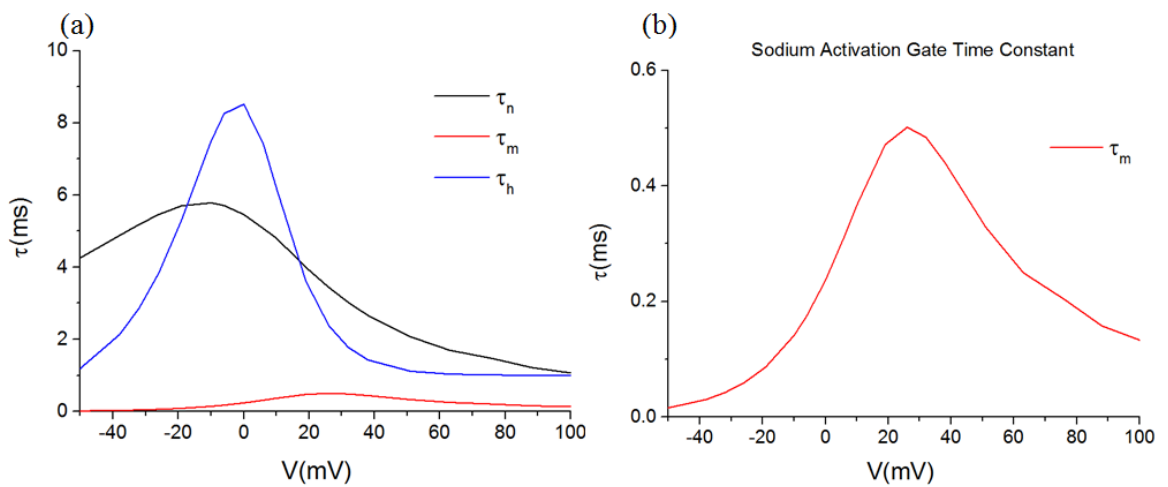
Figure 3.2 Time constants for the potassium activation gate and sodium activation and inactivation gates. The resting potential is at $V = 0mV$. (a) Time constants; (b) A scale enlargement of the sodium activation gate time constant. In this figure, all the lines are calculated from equations (1.15)-(1.20) and (1.8). The equations are proposed by Hodgkin and Huxley in ref. [17] .

3.2.2 Implementing Neural Architectures

After describing the voltage dependence of rate constants and time course of ion channels in HH mode [17], We now demonstrate that how we implement them in the analogue neuron.

The design of the analogue neuron is based on the circuit of HH neuron shown in figure 1.2. When implementing, a fixed capacitor of 10nF is used to represent the cell membrane; a resistor of 10KΩ is used to represent the constant leak conductance; and two MOSFET circuits to represent the potassium and sodium ion currents respectively. Together they

produce pulses which oscillate between the equilibrium potentials of the sodium and potassium ions. The MOSFET circuits mainly consist of two basic building blocks. One is a transconductance amplifier circuit which provides the sigmoid voltage dependence of the ion conductance. The other is a RC delay circuit which provides the time constant $\tau(V)$.

We begin with building a transconductance amplifier circuit. It is used to control conductance transistors which represent the conductance of the ion concerned. The circuit is shown in Figure 3.3(a). This circuit consists of a differential pair Q_1-Q_2 and a single current mirror Q_3-Q_4. According to the basic information of operating a differential pair[68], in the differential pair, the bottom transistor Q_b is used as a current source and I_b sets the total current. Transistors Q_1 and Q_2 compete for a fraction of I_b. The current I_1 drawn out of Q3 is reflected as an equal current out of Q4. Thus I_{out} equals to the difference between the two drain currents from Q_1- Q_2 pair [68]:

$$I_{out}(\Delta V) = I_1(V_1) - I_2(V_2) \tag{3.1}$$

Where ΔV is the differential input voltage. $\Delta V = V_1 - V_2$.

I_{out} as a function of ΔV was measured and shown in figure 3.3(b). According to the plot, I_{out} is activated when $\Delta V=0$. The transconductance G_m of the amplifier can be calculated from the slope of the curves in the plot. And it can be expressed by the following equation [68]:

$$G_m = \frac{\partial(I_1 - I_2)}{\partial(V_1 - V_2)} \propto I_b \tag{3.2}$$

Thus in the circuit, both the maximum value of the activation current and the transconductance G_m can be set by the transistor Q_b.

Technically, transistors in the differential pair Q_1-Q_2 and the current mirror Q_3-Q_4 should be matched to avoid offset voltage and provide precise reflection. Therefore we use ALD1107/ALD1106, which are monolithic P-channel/N-channel matched MOSFET transistor pairs.

The form of the current voltage relation of the differential pair shown in figure 3.3(b) can be regarded as an analogue to the conductance-voltage relation of an ionic conductance. When applying the transconductance amplifier circuit to generating sigmoid voltage dependence of the ion conductance, we fix values of gate voltage of Q_b and Q_2, and use the gate voltage of Q_1 as the input voltage. We regard Q_2 as the knee transistor. It determines the analogue membrane voltage at which the conductance is activated. We regard Q_1 as the

activation transistor for both potassium channel and activation conductance of sodium channel. The activation current increases sigmoidally towards its maximum value as the analogue membrane voltage applied to the activation transistor increases with respect to the knee voltage.

The transconductance amplifier circuit will be finally connected with a conductance transistor, which regulates the flow of ion current oscillating between equilibrium potential of sodium channel (set as 5V) and potassium channel (0V).
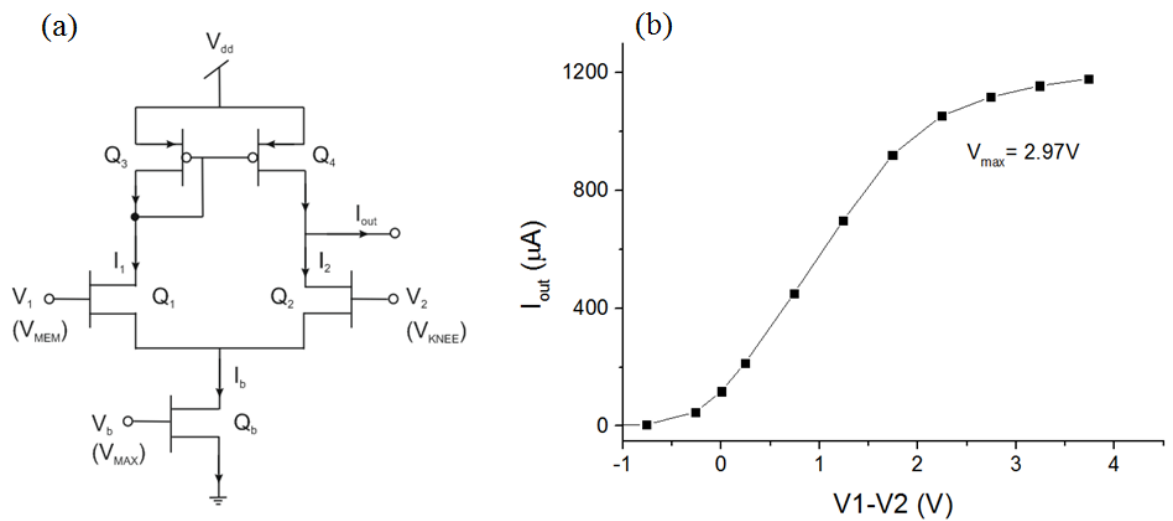
Figure 3.3 Schematic diagrams of the transconductance amplifier circuit and IV curves from the circuit. (a) the transconductance amplifiere circuit. It provides volatege dependent analogue ion current. The circuit consists of a bias transistor Q_b, a differential pair Q_1-Q_2 and a current mirror Q_3-Q_4. V_{dd} is the power supply trial (+5V). In the differential pair, V_1 represents the analogue membrane voltage V_{MEM}. V_2 represents the knee voltage V_{KNEE} at which the membrane is activated. The bias transistor Q_b sets the maxium current I_b through the differential amplifier and controls the transconductance G_m. The output current I_{out} increases sigmoidaly towards the maximum bias current I_b set by V_b. (b) The sigmoid voltage dependence of the output current from the transconductance amplifier. The form of current-voltage relation of the differnetial pair is analogue to the conductance volatge relation of a real ionic conductance. We use the current from the differential pair to control the conductance transistor, which represents the potassium or sodium conductance.

Besides the transconductance amplifier circuit, the other important building block is a RC delay circuit shown in figure 3.4. It provides time-dependent behaviour. This circuit

consists of a transconductance amplifier and a capacitor. Together they work as a low pass filter for the membrane voltage. The filtered outputs with possesses a time constant τ_i then control the activation or inactivation transistors. Unlike the real τ_i shown in figure 3.2 which are functions of V, the analogue τ_i is a constant. The analogue time constants setup is: $\tau_n = 0.10ms$; $\tau_m = 0$; $\tau_h = 0.02$ms. It is not necessary to set them as these specific values. The key thing is the correlation between them. We set these values according to the analysis of figure 3.3, which suggests that $\tau_n > \tau_h > \tau_m$.
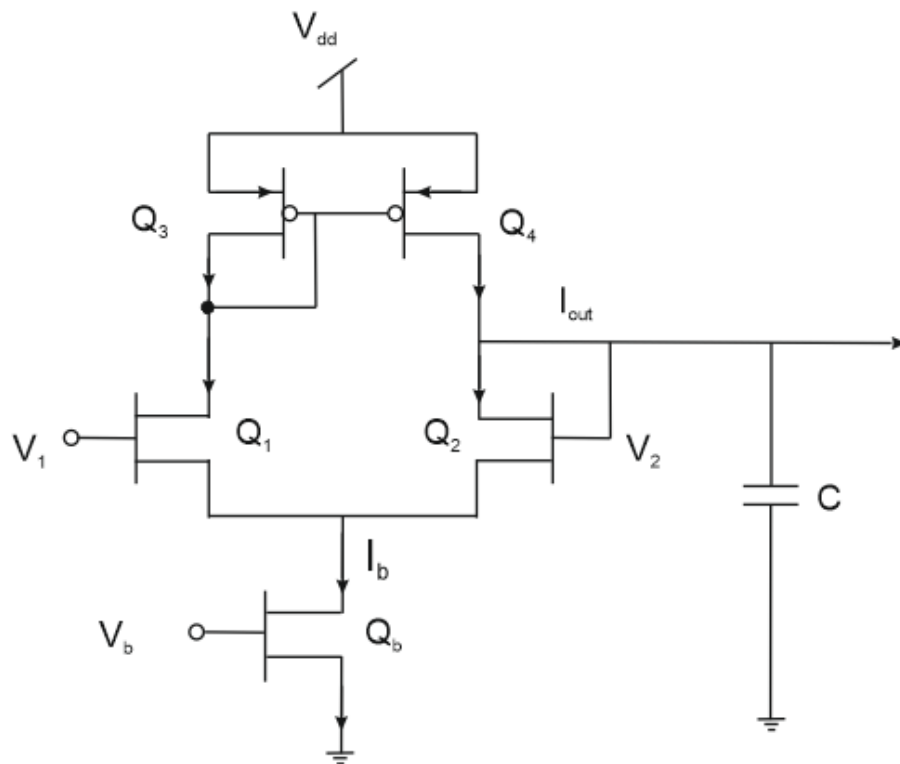
Figure 3.4 Schematic diagram of the RC delay circuit. It acts as a low-pass filter for the membrane voltage. The filtered output controls the activation or inactivation transistors and provides the time constant τ (V). $\tau = \frac{C}{G}$, where G is the tranconductance of the amplifier.

So far, by using CMOS transistors, we have built basic circuit blocks such as the transconductance amplifier, which provides voltage dependence, and the RC delay circuit, which provides time dependence. Now we combine these ideas in the circuits of figure 3.3 and figure 3.4 to construct ion current generation circuits proposed in 1991 [11].

Figure 3.5 is the circuit that generates the potassium current IK. The circuit represents the conductance of potassium channel. It mainly consists of a low pass filter, a

transconductance amplifier and a conductance transistor, which represents the potassium conductance. In this analogy, the activation of the potassium conductance is represented by the time- and voltage- dependent output currents of the differential pair. The knee transistor of the pair determines the threshold value of the membrane voltage for activating the conductance. The membrane voltage V_{MEM} is low pass filtered by a RC delay circuit. These implement the time dependence. The time constant of filtering determines the time delay of the activation gate variable τ_n. It can be tuned by tuning the KDTAUM parameter. The output current of the RC delay circuit KDM controls the activation transistor of the differential pair. This implements the voltage dependence. KDM is then reflected by a current mirror and transformed into the gate voltage K_{DVG} that controls the conductance transistor. EK represents the potassium equilibrium potential. Here we set it as 0V.
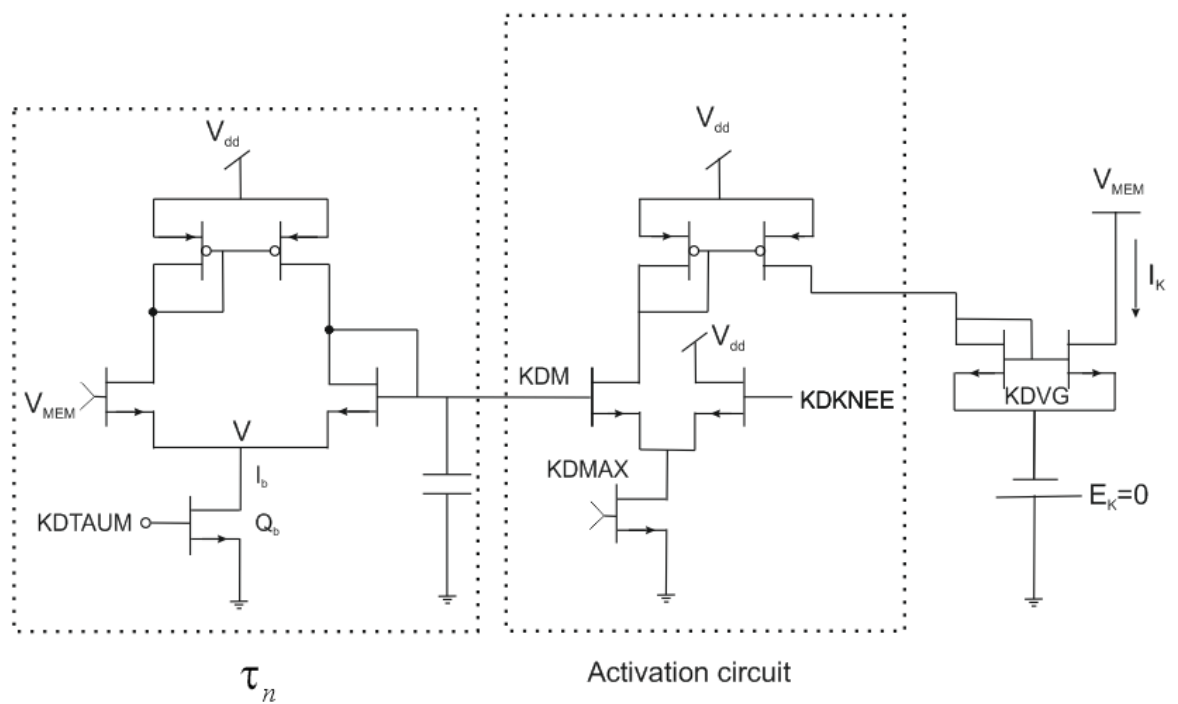
Figure 3.5 The analogue circuit that can model the potassium channel in biological membranes. It consists of a RC delay circuit, a transconductance amplifer and a conductance transistor. The RC delay circuit is marked as activation circuit in the figure. The transconductance amplifier is marked as τ_n in the figure. V_{dd}: the power supply rial (+5V). VMEM: The membrane voltage; KDTUM: acivation time constant; KDM: the output current of the low pass filter; KDMAX: maximum activation; KDKNEE: half-activation membrane voltage; KDVG: gate voltage that controls the conductance transistor; E_k: the potassium equilibrium potential. KDVG: gate voltage of the potasium conductance conductance transistor; I_K: analogue potassium current. Initial setup: KDTAUM=4.16V, C_k=100nF; KDMAX=2.97V, KDKNEE=1.26V. $\mathbf{\tau_n = 0.10ms}$.

Figure 3.6 is the circuit that generates the sodium current I_{Na}. The circuit represents the conductance of sodium channel. Unlike the potassium conductance which doesn't have the inactivation channel, the sodium conductance is the combination of both the activation and inactivation channels. As the activation channel responses rapidly, we directly apply V_{MEM} to the differential pair of the activation sub circuit rather than connecting it with a RC delay circuit. In this case, there will be no time delay for opening the activation gate of sodium channel. NaONMAX is the maximum activation voltage. NaONKNEE is the half maximum activation voltage. The output of the sub circuit is the sodium activation current. V_{MEM} for the inactivation sub circuit is low-pass filtered by a RC delay circuit. NaTAUH controls the time constant of filtering, which is the time delay of the inactivation gate variable for sodium channel τ_h. The output current NAH controls the inactivation differential pair. NaOFFMAX is the maximum inactivation voltage. NaOFFKNEE is the half maximum inactivation voltage. The output current of the inactivation differential amplifier is reflected by a current mirror and then combined with the output current of the activation differential pair. $I_{Na} = I_{activation} - I_{inactivation}$. The combination current is transformed into gate voltage NaVG and controls the sodium conductance transistor. ENA represents the sodium equilibrium potential. Here we set it as 5V.

Without considering the time constant, V_{MEM} will vary between the 0V and the 5V levels which are the analogue of the sodium action potential (+55mV) and the potassium action potential (-72mV) in real neurons. However, limited by the time constants, V_{MEM} actually oscillates between 0V and 3.7V. Spikes generated by silicon neurons will be shown in 3.5.2.
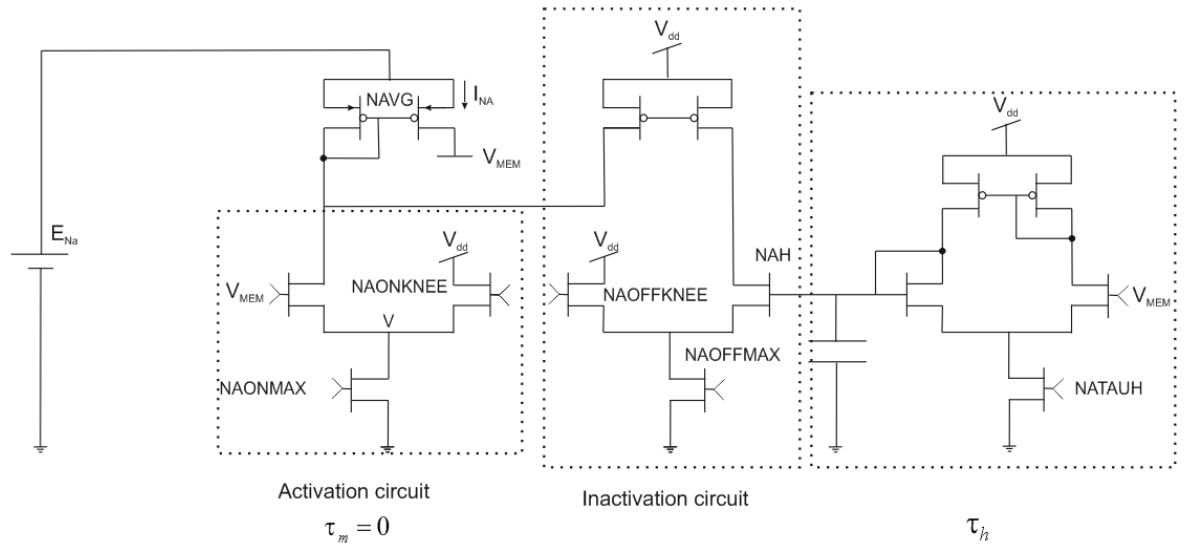
Figure 3.6 The analogue circuit that can model the sodium channel in biological membranes. It consists of an inactivation subcircuit and an activation subcircuit. Both of the subcircuits are implemented by using transconductance amplifieres. τ_h is implemented by using a RC delay circuit. V_{dd}: the power supply rial (+5V). E_{Na}: sodium equilibrium potential; V_{MEM}: the membrane voltage; NaONMAX: the maximum activation voltage; NaONKNEE: the half maximum activtion voltage; NAOFFMAX: the maximum inactivation voltage; NaOFFMAX: the half maximum inactivation voltage; NaTAUH: inactivation time constant; Na_{VG}: gate voltage of the sodium conductance; I_{Na}: analogue sodium curent. $I_{Na} = I_{activation} - I_{inactivation}$. Initial setup: NaONMAX=3.74V, NaONKNEE=1.52V; NaOFFKNEE=4.76V, NaOFFMAX=2.84V, NaTAUH=1.72V, C_{Na}=10nF, $\tau_h = 0.02ms$

We summarize all the parameters we used for the analogue ion in table 3.2. The activation and inactivation knee voltages of the sodium and potassium ion channels are set by scaling the known biological thresholds to the 0-3.7V interval [18]. Ideally, V_{MEM} will oscillate between the 0V and the 5V levels which are the analogue of the sodium action potential (+55mV) and the potassium action potential (-72mV) in real neurons. The real amplitude of spikes is affected by time constants and values of them are obtained experimentally in subsection 3.5.2. The frequency of the spiking patterns is determined by the time constants of the sodium and potassium gates, τ_h and τ_n, together with the membrane charging time $\tau_{membrane}$ which is determined by the value of membrane capacitance. During experiments we tune the frequency of spikes by tuning the values of capacitance C_{Na}, C_K and C_m.

	Analogue Neuron	Real Neuron
$\overline{g_m}$	0.40mS	80mS/cm^2 [17]
NAONKNEE	1.52V	-64mV [74]
τ_m	0	0-0.5ms [17]
$\overline{g_h}$	0.97mS	160mS/cm^2 [17]
NAOFFKNEE	4.76V	-26mV [74]
τ_h	0.02ms	0-9ms [17]
$\overline{g_n}$	0.32mS	36mS/cm^2 [17]
τ_n	0.10ms	0-6ms [17]
KDNEE	1.26V	-78mV [75]

Table 3.1 Parameters for an analogue neuron and bio-membranes. All the analogue parameters are obtained in my lab. All the parameters from bio-membranes are from references mentioned in the table. Analogue parameters should agree to the correlation of parameters in bio-membranes, such as $\tau_n > \tau_h > \tau_m$, NAOFFKNEE>NAONKNEE>KDNEE.

3.3 Synapses

Our synaptic circuits are actually variable coupling conductance rather than realistic synapses. They translate the voltage differences between membranes of two isolated analogue neurons into synaptic current with a gain typically referred to as the synaptic conductance or synaptic weight *g*. This is implemented using the VLSI differential current amplifiers.

We take synapse which provides the synaptic weight *g₁₂* as an example. The circuit is shown in figure 3.7. It consists of a differential amplifier that supplies a current $I_{12} = I_1 - I_2 = g_{12}(V_1 - V_2)$. *V₁* and *V₂* represent the presynaptic and post synaptic voltages respectively. We switch the state of the synapse between 'excitatory' or 'inhibitory' by switching the direct of *I₁₂*. If neuron 2 is inhibited by neuron 1, then the synaptic current will be injected from neuron 2 into neuron 1 ($I_{1\leftarrow2}$); if neuron 2 is excited by neuron 1, then the synaptic current will be injected from neuron 1 to neuron 2 ($I_{1\rightarrow2}$).

In the thesis we focus on inhibitory coupling between neurons. We define inhibitory synaptic current I_{12} is originally from neuron 1 and acts on neuron 2. The related synaptic conductance is denoted by g_{12}.
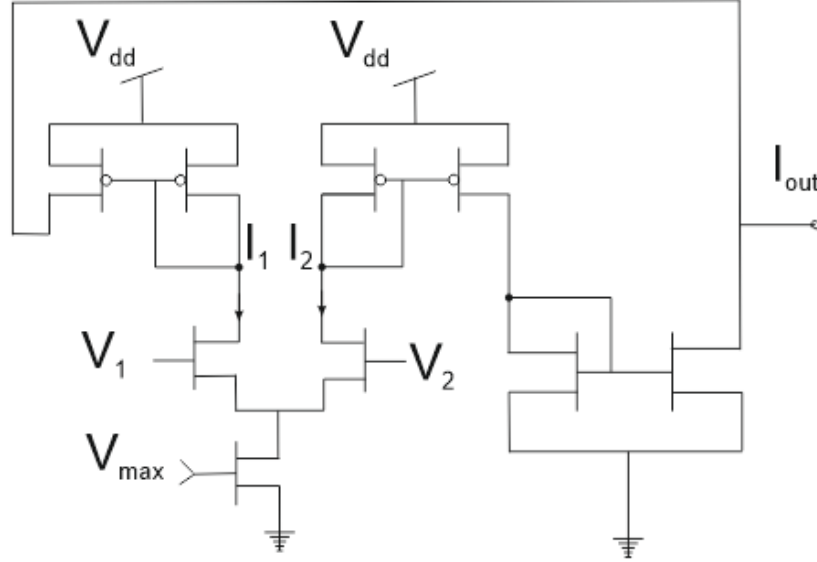
Figure 3.7 The circuit of an analogue gap junction synapse. V_1 and V_2 are the pre- and post-synaptic neuron membrane voltages. V_{max} determines the gain between I_{out} and (V_1-V_2).

The operation of the differential pair in figure 3.7 is the same with the operation of the differential pair in figure 3.3 (a). The synaptic conductance can be expressed by the equation below:

$$g_{12}(V_{max}) = \frac{\partial(I_1 - I_2)}{\partial(V_1 - V_2)} = \frac{I_{out}}{\Delta V} \tag{3.3}$$

Where I_{out} is the output current of the circuit in figure 3.7 and ΔV is the differential voltage. The strength of the synaptic conductance g_{12} can be controlled by tuning V_{max}. The value of it can be obtained by measuring the output current and differential voltage. I_{out} as a function of ΔV is shown in figure 3.8 (a). g_{12} equals to the slope coefficient of curves in figure 3.8 (a). Synaptic conductance as a function of V_{max} is shown in figure 3.8 (b). It gives the range of the value of g_{12}. The minimum value of g_{12} is $16\,\mu S$, which results from V_{max} of 0.8V. 0.8V is the minimum gate to source voltage of ALD1106/1107 transistor pairs that is needed to create conducting paths. 0.9V is the maximum value of V_{max} that we used for experiments in this thesis.
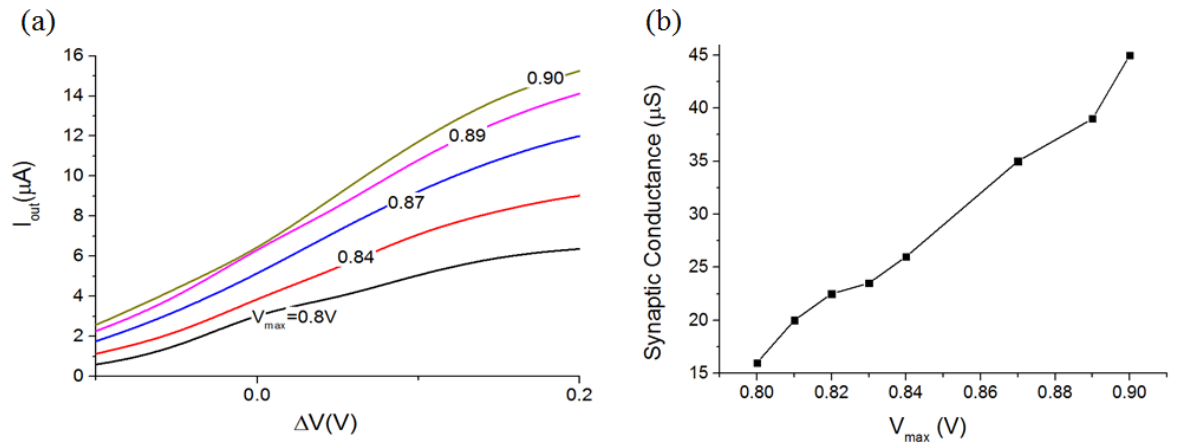
Figure 3.8 (a) Output current of the synaptic conductance amplifier as a function of differential input voltage. $\Delta V = (V_1 - V_2)$. V_{max} is the gate voltage that determines the maximum value of I_{out} and the synaptic conductance. The synaptic conductance equals to the slope coefficient of the curves. (b) Synaptic conductance as a function of V_{max}.

Finally, we summarize the design of the neural network that has been demonstrated in subsections 3.2 and 3.3. In order to construct a silicon neuron, an analogue membrane capacitor of 10nF, a resistor of 10KΩ which represents constant leak conductance, a circuit block which represents the potassium conductance as shown in figure 3.5 and a circuit block which represents the sodium conductance as shown in figure 3.6 are connected in parallel according to the circuit shown in figure 1.2. In order to inhibitory connected silicon neurons, circuits that represent electrical synapses as shown in figure 3.7 are inserted between neurons. In this way, an analogue neural network is constructed.

3.4 Fabrication of the PCB board

We manufactured the electronic circuits though the use of printed circuit boards (PCBs).

The manufacture begins with making the PCB mask. We designed the circuit by the software 'destools'. The designed circuits were then exported to the PCB layouts. As we were going to manufacture a double sided PCB, there were two layouts: one is for the soldering side and the other is for the component side. The layouts were printed on transparent films and become PCB masks.

The next stage is the manufacture of a printed circuit board. We placed the PCB mask underneath the photo-resist board. Both sides of the photo-resist board are copper clad the copper has a photosensitive coating, which touched the PCB masks. The PCB masks and board are then transferred to the UV light box and exposed for 3 minutes. After the UV exposure, the photo-resist board is placed in a tank filled with solution of sodium hydroxide photo developer (NaOH: H_2O=1:200). After the board is taken out of the developer, it is washed in clean water and then transferred to the etching tank. Ferric chloride is used for etching. In this step, the unwanted copper is slowly etched away, leaving the copper tracks only. The etching process lasts about 5 minutes. It is important to keep checking to prevent the board from over etching. If the board is over etched, the copper tracks will be damaged. When removed from the etching solution, the PCB board is washed under tap water. The cleaning work must be done carefully to make sure that any film has been removed from the tracks because the film will prevent good soldering to the PCB. The tracks are checked. If there are gaps in the tracks, they can be repaired by using soft solders.

The last stage is fixing all the components on the PCB board. Holes are drilled through the board by using a small PCB drill. Components are located and soldered in position. A photo of the prepared PCB board is shown in figure 3.9. Six analogue neurons are constructed on the board. 30 inhibitory synapses are inserted in-between the neurons. A block diagram for explaining the construction of each analogue neuron is shown in figure 3.10. A block diagram for explaining the configuration of the neural network is shown in figure 3.11.

Current stimulus
was injected into
the board

Membrane voltage of
analogue neurons
were measured
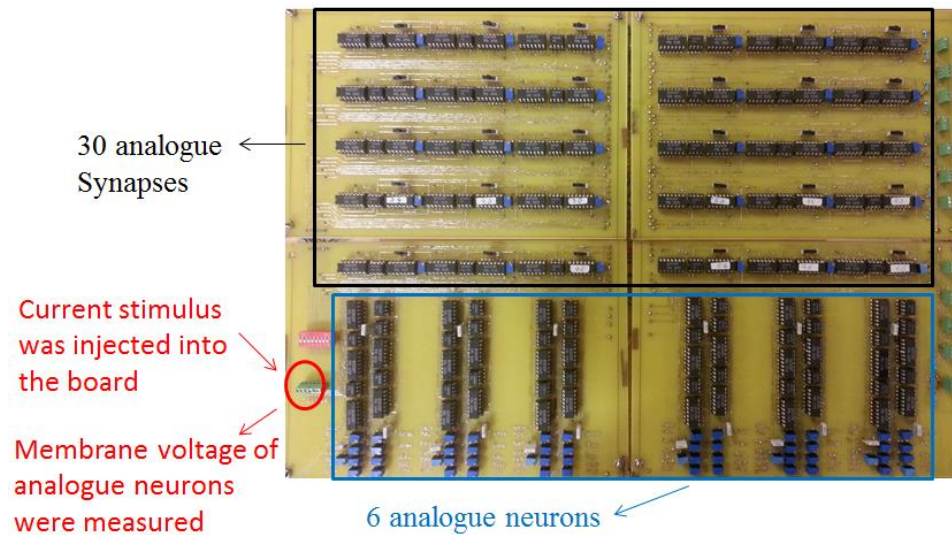
6 analogue neurons

Figure 3.9 The photo of the prepared board. It shows 6 analogue neurons and 30 analogue synapses on the board. It also shows where we inject current stimulus into each neuron and where we measure the membrane voltage of each analogue neuron.
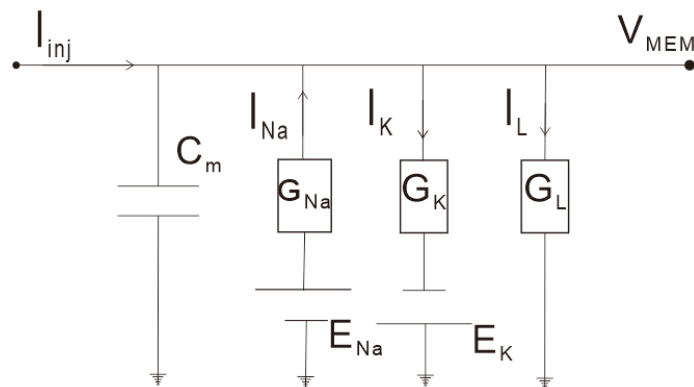
Figure 3.10 A block diagram for explaining the construction of an analogue neuron. In the diagram, G_{Na} and E_{Na} are achieved by the circuit shown in figure 3.6. G_K and E_K are achieved by the circuit shown in figure 3.5. C_m is the analogue membrane capacitor and is achieved by a capacitor of 10nF. G_L is the constant leak conductance and is achieved by a resistor of 10KΩ. All of the elements, including the capacitor, the sodium conductance, the potassium conductance and the leak conductance, are attached to the horizontal wire such that they are connected in parallel. Stimulus current is injected into the horizontal wire. The potential of the horizontal wire relative to the ground is measured as the analogue membrane voltage V_{MEM}. When stimulus current injection drives membrane potential above NaONKNEE, the activation current part of Ina drives V_{MEM} to near E_{Na}. After τ_h, the inactivation current part of Ina turns on and V_{MEM} starts to decrease. And After τ_n, I_K turns on and pulls V_{MEM} back down toward E_K. NaONKNEE, τ_h and τ_n has been explained in figure 3.5 and figure 3.6.
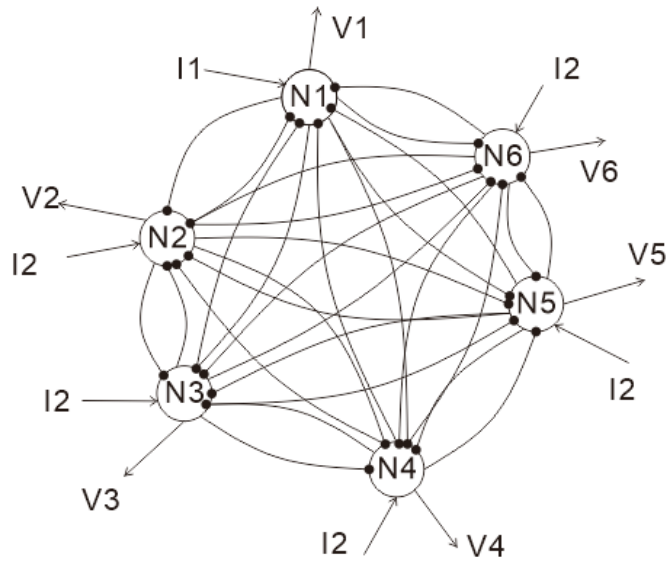
Figure 3.11 A block diagram for explaining the configuration of the neural network. In the diagram, large circles marked by N1-6 represent 6 analogue neurons. In order to active the analogue neuron, direct current is injected into each neuron respectively. I1-6 represents the stimulus current. During experiments, analogue membrane voltage of each neuron is measured. V1-6 represents the analogue membrane voltage. Curves with solid dots at one end represent the 30 analogue synapses. They are inserted in between analogue neurons. There are two synapses between every two neurons. They carry synaptic current with opposite directions. We use black dots at the end of curves to indicate that neurons are inhibitory connected as well as indicate the direction of the synaptic current. The synaptic current is flowing from the end without the black dot to the other end of the curve. Every single neuron is inhibited by the other five neurons in the network.

3.5 Dynamics of Silicon Neurons

In this subsection, we study the dynamics of the HH model neuron by examining the response of its membrane voltage to external direct current with different values. Also, we study the inhibitory interaction between neurons via gap junction synapse by producing antiphase spiking trains.

3.5.1 Experimental Setup

We used depolarizing current to activate the analogue neurons. In order to generate stimulus current, voltage to current converter circuits shown in figure 3.12 are built for operating ion conductance circuits. The function of this circuit is controlling the output current by the small input voltage V_{in}. The output current is equal to the current through R.

The voltage drops in the circuit can be neglected because the currents through R_1 and R_2 are essentially zero. The op-amp's negative feedback adjusts the current thought the MOSFET until the voltage across R is equal to the control voltage. C provides some low pass filtering of the feedback. Therefore, the voltage across R is equal to the input voltage V_{in}.

$$I = \frac{V_{in}}{R} \qquad (3.4)$$

The conductance circuits can be operated like this: the DC voltage V_{in} is converted to the input current I_{in} by the voltage to current converter. I_{in} is set by tuning V_{in}. Then I_{in} is injected into to the silicon neuron circuits and leads to the oscillations of the analogue neurons. The silicon neurons are driven by a power supply.
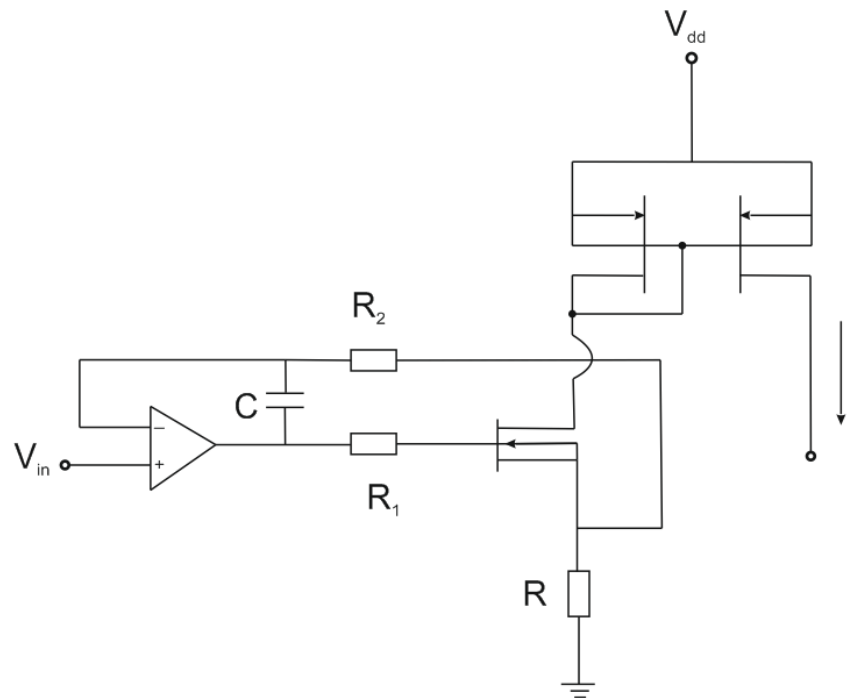
Figure 3.12 The voltage to current converter circuit. This circuit allows the the output current to be controlled with a small input voltage V_{in}. R1=100Ω; R2=10KΩ; C=10nF.

A block diagram for explaining the whole setup is shown in figure 3.13. Voltage supply is from a power supply and converted into current by voltage-to-current converter circuits. The current stimulus is injected into the analogue neural network and analogue membrane

voltages are measured. Both the current injection and voltage measurement is controlled by LabVIEW programs wrote by me.
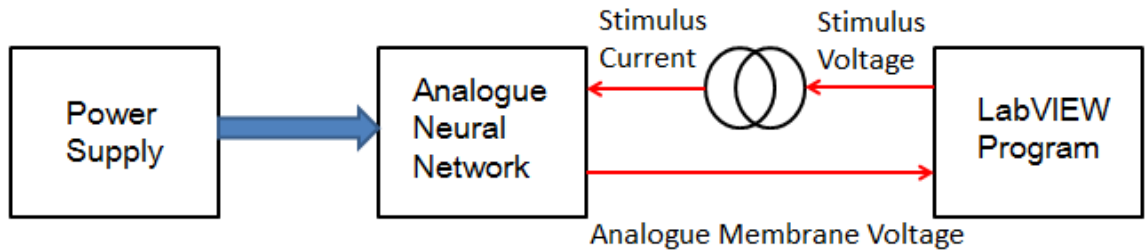
Figure 3.13 A block diagram for explaining the experimental setup. The whole setup includes a power supply, a voltage to current converter circuit, a PCB board on which the analogue neural network is constructed and LabVIEW programs for controlling the current injection and voltage measurement.

3.5.2 Dynamic Properties of an Individual Neuron

In this subsection, we check the dynamic properties of a single silicon neuron, such as firing threshold, firing frequency, etc.

The current threshold for firing the silicon neuron is $86\,\mu A$. Figure 3.14 shows that subthreshold current can only evoke a passive charging response. Spikes arise when the injected current is 86 μA, which is just on the threshold. Spikes generated by the silicon neuron oscillate between 0 and 3.7V.
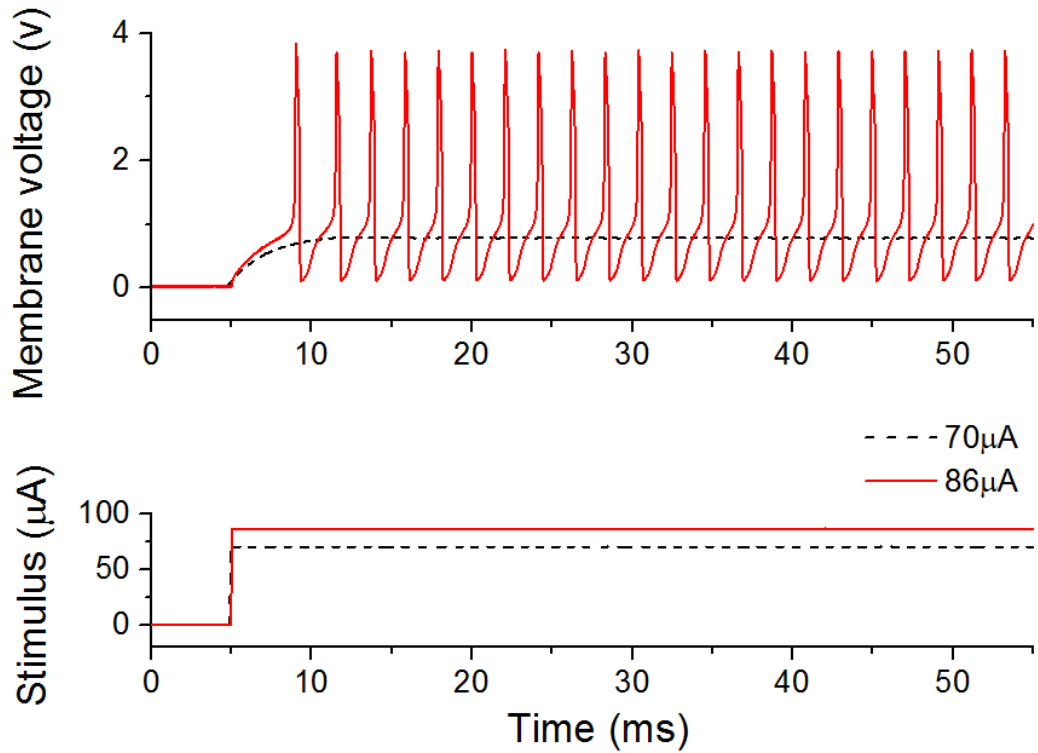
Figure 3.14 Response of a silicon neuron to direct current stimulus with different values. The trace represented by dash lines results from the stimulus of 70 μA; the trace represented by solid lines results from the stimulus of 86 μA. Spikes arise only when the input current is above the threshold of 86 μA. The amplitude of the spikes is 3.7 V.

As indicated in figure 3.4, we can use the time constant in RC delay circuits in V_{MEM}, NAOFFKNEE and KNEE to control the spiking rate. They correspond to $\tau_{membrane}$, τ_h, and τ_n respectively. The time constant is proportional to the capacitance. Therefore we can control the spiking rate by varying the values of the capacitance C_{Na}, C_K and C_m. Figure 3.15 shows that the firing rate can be reduced when increasing the value of the capacitance. For all the measurements, the magnitude of stimulus current is fixed at 100 μA. For obtaining the firing rate of 654Hz in bottom trace, $C_m=C_{Na}=10$nF, $C_K=100$nF. We then increase C_m and C_{Na} to 20nF, and increased C_K to 200nF. In this way, the time constant was doubled by doubling the value of capacitors C_m, C_{Na} and C_K. The firing rate is then reduced by about half to 326Hz. The full width at half maximum of spikes is doubled. This is because that increasing the time constant can slow down the process of charging the membrane and allows the conductance to slowly inactivate. Table 3.2 summarizes values of capacitance and the corresponding frequencies.
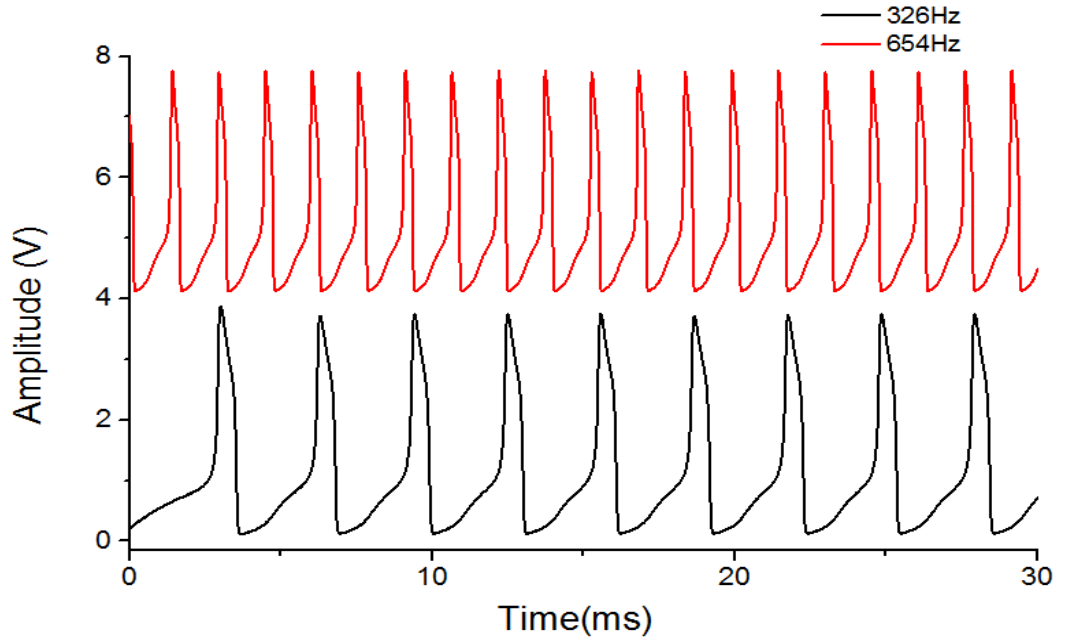
Figure 3.15 Firing frequency can be tuned by changing the time constant of $\tau_{membrane}$, τ_h, and τ_n in individual neurons. To eliminate the influence of current, the magnitude of current stimulus is fixed at $100\,\mu A$. From bottom trace to top trace, the time constant is doubled by doubling values of capacitors C_m, C_{Na} and C_K. In the bottom trace, $C_m=C_{Na}=10nF$, $C_K=100nF$; in the top trace, $C_m=C_{Na}=20nF$, $C_K=200nF$. The frequency is decreased from 654Hz to 326Hz. Besides, the full width at half maximum of spikes is doubled.

$C_m/C_{Na}/C_K$ (nF)	Frequency (Hz)
10/10/100	667
20/20/200	323
30/30/300	217
40/40/400	161

Table 3.2 Values of capacitors and corresponding firing frequencies. C_m is the membrane capacitance related to membrane charging time $\tau_{membrane}$. C_{Na} is related to τ_n. C_K is related to τ_h.

Figure 3.16 shows that the firing frequency of an analogue neuron is increased when increasing the magnitude of the external current. For all the points in this plot, $C_m=C_{Na}=20nF$, $C_K=200nF$. We choose results resulted from this set of capacitance to show here because it is related to the experiments in chapter 4. Starting from $0\,\mu A$, the stimulus

current is gradually increased by an increment of $2\,\mu A$/step until we find the threshold of $86\,\mu A$. Then starting from $90\,\mu A$, the stimulus current is increased by an increment of 10 μA to plot the firing frequency vs. current. The plot shows that no spike is generated when current is lower than the threshold. The spiking frequency is a nonlinear increasing function with respect to the current. From current of $86\,\mu A$ to $180\,\mu A$, the frequency is increased from 233Hz to 505Hz.
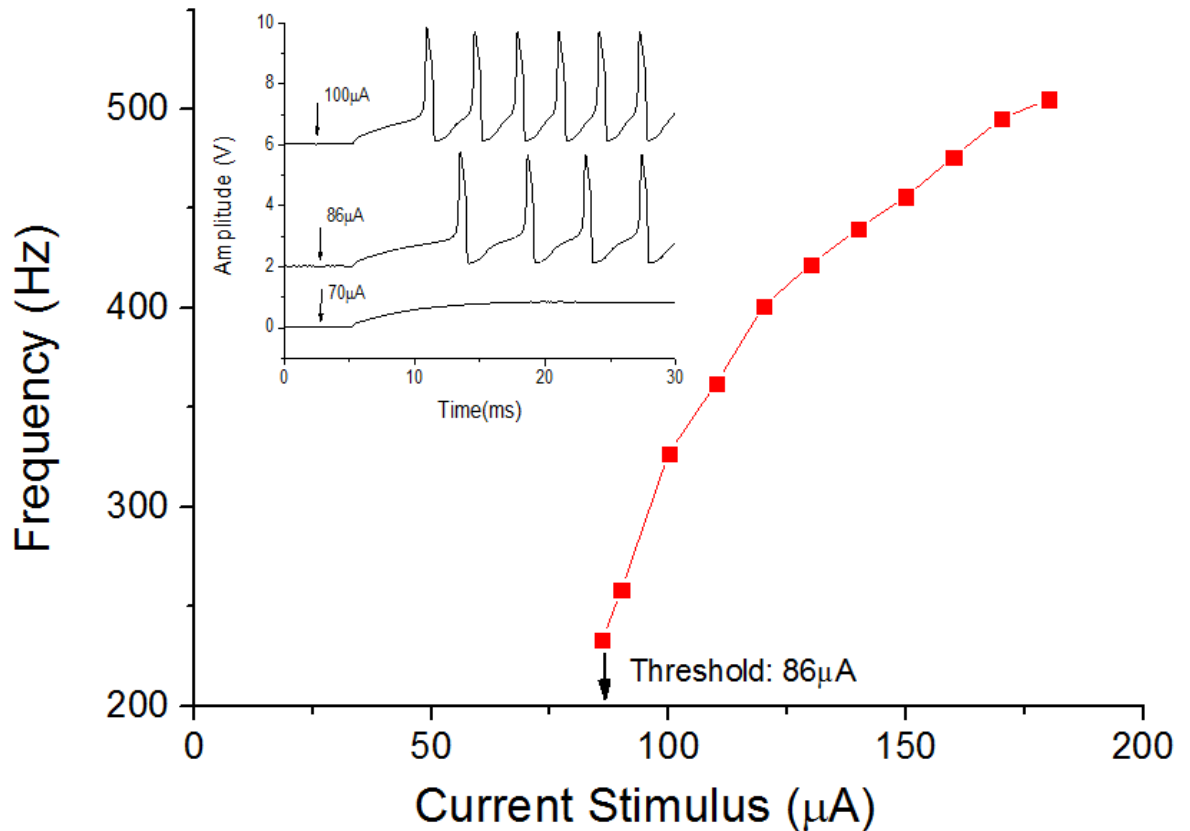
Figure 3.16 The firing frequency as a function of current stimulus. Insert: Spiking patterns corresponding to current stimulus of $70\,\mu A$, $86\,\mu A$ and $100\,\mu A$.

3.5.3 Synchronization of Coupled Neurons

After checking dynamical properties of individual neurons, we now use a mutually excitatory/inhibitory synapse to couple two neurons together and check the firing sequence of coupled neurons.

Figure 3.17 shows the firing sequence of two decoupled neurons as a comparison of results from coupled neurons later. The parameters of the two neurons are the same. $C_m=C_{Na}=20$nF, $C_K=200$nF. One neuron is excited by a direct current of $100\,\mu$A and the other is excited by a direct current of 105 µA. We use stimulus current with different values such that the two neurons have slightly different firing frequency. In this way, it is easier to see the time difference of spikes from the two neurons. Each neuron is oscillating at its own natural frequency. We name the two neurons neuron 1 (N1) and neuron 2 (N2). The spikes from an individual neuron are continuous and even distributed. The time delay between spikes of the two neurons, which has been marked in the plot, is changing gradually and irregular thus the two neurons are not synchronized.
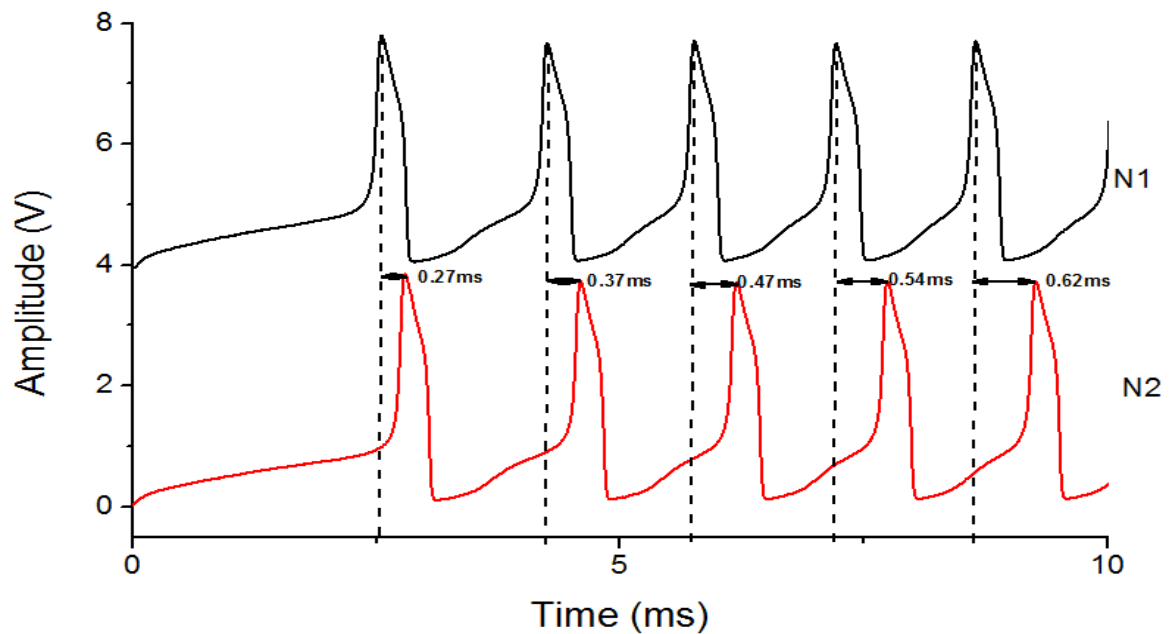
Figure 3.17 Firing sequence of two decoupled neurons. Each neuron is excited by a direct current of $100\,\mu$A and oscillates at its own natural frequency. Time delays between spikes of the two neurons have been marked in the plot.

Figure 3.18 shows the spiking pattern produced by neurons coupled via mutually excitatory synapses. In this case, when N1 is firing, it injects current into N2 via the excitatory synapse. The injected synaptic current will be added on the stimulus current for N2 and increase its probability of firing and vice versa. In this way, the two neurons are synchronized and firing with no phase lag. However, in this research, we do not study the excitatory synapse because it induces the synchronized stage. Instead we focus on the

inhibitory synapse, which is the key to produce winnerless dynamics and flexible rhythmic pattern generation.
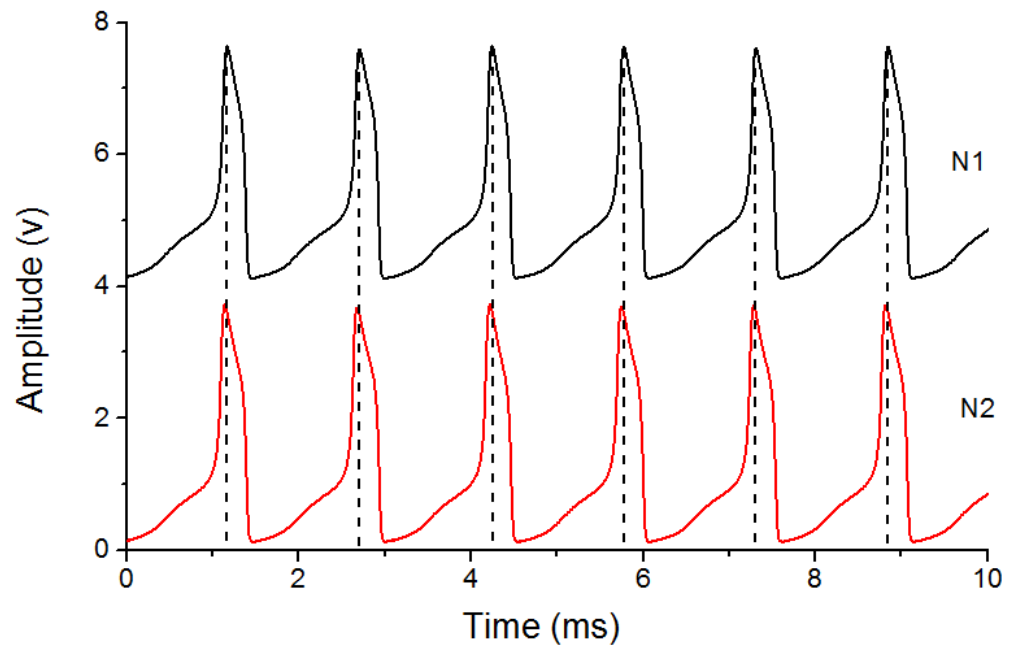
Figure 3.18 In phase synchronization of neurons coupled via mutually excitatory synapses. The synaptic strengths are arbitrarily set as g_{12}=23.5 μS, g_{21}=37.2 μS.

Figure 3.19 shows the out-of-phase spiking patterns from three neurons which are interconnected by mutually inhibitory synapses. Each neuron is excited by a direct current of 100 μA. The synaptic strengths are arbitrarily set as g_{12} =23.5 μS, g_{21}=37.2 μS. Time delays between spikes of the two neurons are marked in the plot. At the beginning, there is a transient time during which the time delay is varying. This indicates the spiking pattern produced by the coupled neurons is not periodic. After the transient time, time delay between spikes from the two neurons is fixed. The two neurons acquire identical frequencies. In this way, they generate periodic spiking patterns with a certain rhythm. The dependence of properties of rhythmic patterns on parameters such as synaptic conductance, current stimulus, etc. will be discussed in details in chapter 4.
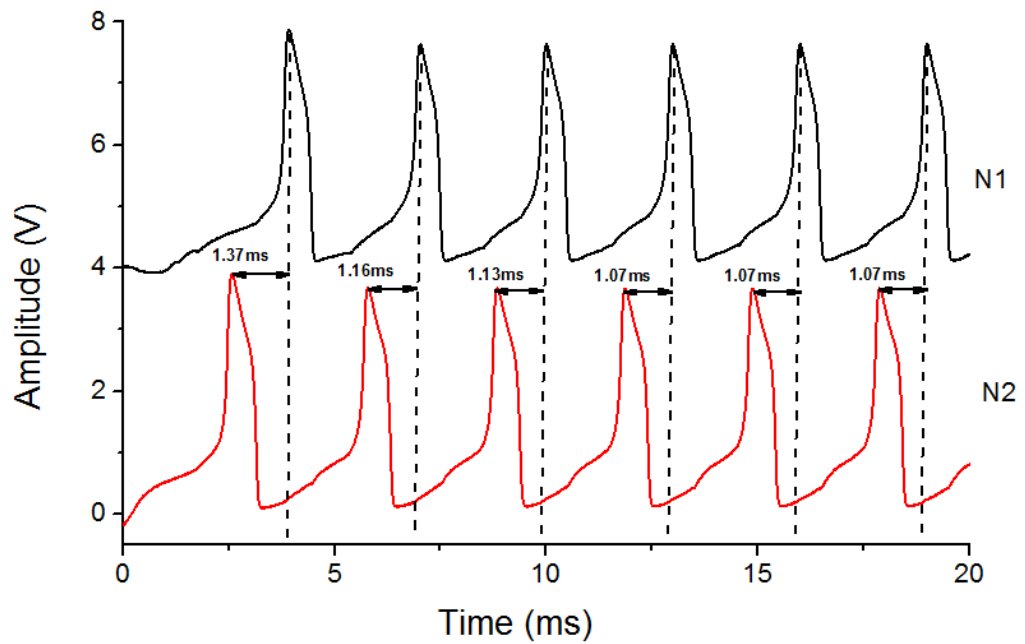
Figure 3.19 Out-of-phase synchronization of neurons coupled via mutually inhibitory synapses. Stimulus current for each neuron: $100\,\mu A$. synaptic conductance is changed. The synaptic strengths are arbitrarily set as $g_{12}=23.5\,\mu S$, $g_{21}=37.2\,\mu S$.

3.6 Summary

We have fabricated six silicon neurons based on HH neuron model by replicating ion channels in hardware. The neurons are operated in real time and show realistic neuronal behaviours such as producing action potentials. We have tested the intrinsic dynamic properties of the neurons, such as the firing threshold, frequency, etc.

Besides, we have also fabricated electrical synapses in order to connect the six silicon neurons together and build a neuron network. The synaptic current can induce either excitatory or inhibitory behaviours in the network. We focus on the inhibited effect of the synapses and the resulting rhythmic patterns generated by the neural network. This will be further discussed in details in chapter 4.

Chapter 4 Stimulus-dependent Rhythms in Central Pattern Generator Hardware

4.1 Introduction

4.1.1 Multifunctional Central Pattern Generators (CPGs)

A multifunctional (CPG) is able to produce multi-stable rhythmic patterns [79]. In neural dynamics, each stable rhythmic pattern generated by a neural network is called an attractor and it can be a fixed point in the phase space because many choices of initial conditions will evolve toward it. Each attractor is conjectured to be associated with a particular locomotive activity of the CPG [80]. The coexistence of attractors as well as the switching between them have been intensively studied in CPG models by simulation [55, 56, 79]. The basic building block of many CPGs is a half-center oscillator composed of two neurons [44]. The two neurons interact through reciprocal inhibitory synapses and produce antiphase or in-phase bursting patterns. Increasing the number of neurons in CPG circuits can enrich the dynamical information capacity, such as increasing the number of attractors. It has been shown in theory that a system of three neurons possesses five attractors corresponding to stable rhythmic patterns resulted from neurons fring in a sequence of two neurons firing in phase and out of phase with the third [55]. Whether the system converges to one attractor or another depends on the initial conditions defined by the relative timing of the current steps stimulating the neurons. In ref [55], basins of attraction of the CPG consisting of three neurons have been mapped.

In this chapter we first study the stimulus dependent rhythms in CPG hardware. The hardware consists of three Hodgkin-Huxley silicon neurons [11]. Each can produce tonic spiking patterns. Neurons are connected via mutually inhibitory gap juntion synapses with asymmetric conductance. We find that maximum three stable rhythmic patterns based on magnitude of synaptic conductance are generated by our neural circuit in the steady state. Switching between thesee patterns depend on the choice of the initial conditions represented by the relative timing of the current stimuli.

We study the stimulus-dependent dynamics by recording spiking patterns generated by the neural system. When individual neurons are stimulated by a current step, a transient interval occurs during which the spiking patterns are not periodic. For different initial

conditions, we expect the spiking patterns to evolve towards the same steady state regime which is an attractor in a phase space and strongly depends on initial conditions. We map the transient dynamics of the experimental CPG and show that stable attractors can be identified in a phase lag map.

4.1.2 Dynamics in the CPG: Winnerless Competition Principle

We employ winnerless competition principle to understand the attraction dynamics of the network.

Winnerless competition (WLC) principle was first proposed to interpret the phenomenon that the olfactory neurons can transform odours stimuli into deterministic stimulus-specific firing patterns [81]. In their model, a winnerless competition neural system requires many neurons constructed in a closed loop and these neurons interact at least partly through inhibitory connections. The transformation of incoming stimulus into spatiotemporal output patterns can result from the interaction through inhibitory connection among neurons. The output spatiotemporal patterns correspond to trajectories of electrical activity bouncing through the network from one neuron to the other. The activating sequence of neurons is determined by the strength of the inhibitory connections between neurons.

The WLC dynamics has been studied in neuron models in theory to show how the external stimulus can be coded into action generations and discuss the stability of the attractors [82-85]. And based on the computation study, Rabinovich et al. [18] demonstrated that the key features of WLC neural network are robustness and sensitivity. More precisely, a good WLC system should be robust under small perturbation and meanwhile, it should be very sensitive to input signals.

We first demonstrate WLC dynamics in the CPG hardware. We use step currents as the external stimulus and our CPG network can transform them into deterministic stimulus specific spatiotemporal patterns. The patterns are sensitive to stimulus so we can switch between attractors by selecting stimulus. Meanwhile, the patterns are insensitive to noise because small changes in stimulus which work as noise perturbation can only cause the system to gravitate around the attractor. We plot phase lag maps to express this process: in the map, trajectories can be swithced by selecting initial conditions and different trajectories can converge to the same attractor. In this way, the winnerless competition system show sensitivity and robustness.

4.2 Experimental Details

4.2.1 The Configuration of the CPG and Initial Conditions for Stimulation in the CPG

The configuration of our neural network is an inhibitory triangle loop consisting of three silicon neurons connected by reciprocal synapses. This is shown in figure 4.1(a). Three neurons in the network have the same time constants (C_m=C_{Na}=20nF, C_K=200nF). External current stimulus (I_1, I_2 and I_3) is injected into the three neurons respectively. The amplitude and time delay of the current stimulus is controlled by a LabVIEW program. Gij (i≠j) is tuneable synaptic conductance, which represents the coupling strengths between neurons. It can be varied by tuning the gate voltage as demonstrated in chapter 3. We use asymmetric coupling strength (g_{ij}≠g_{ji}) in order to prevent the automatic in-phase spiking of neurons [8].

Every single neuron is triggered by a current stimulus of 100 μA, which is just above the firing threshold of 86 μA. When the stimulus is 100 μA, the intrinsic firing frequency of an individual neuron is 323Hz. However, the firing threshold and frequency of individual neurons in the network will be different from that of an isolated neuron due to inhibitory connection. We choose current stimulus of 100 μA because this value is strong enough to make sure that all the neurons in the network can be fired. In the meantime, it is weak enough to keep firing frequency of the neurons at its lowest value. The low frequency can prolong the evolution towards the attractor and hence permit us to see smooth trjectories with details in a phase lag map. During the experiments, we will increase the frequence by increasing magnitude of current stimulus to study the dependence of attraction basins on the spiking frequency.

We use the time delay between the current steps as the parameters that regulate the rhythmic patterns of the neural network. This is shown in figure 4.1(b). Step voltage stimulus is generated by a NI6259 DAQ card and then converted into direct current stimulus by voltage to current converters. Every single neuron is triggered by a particular current stimulus at its own timing. The time delay is controlled by the DAQ card. It is varied between 0 and the period of oscillations of the independently firing neuron. If t_n (n=1, 2, 3) is the time when the current step is applied to nth neuron. $\Delta t_1 = t_2 - t_1$, $\Delta t_2 = t_3 - t_1$, where Δt_1 and Δt_2 are the time delays between applying current to neuron 2 or neuron 3 and applying current to neuron 1. We the normalize Δt_1 and Δt_2 over the period

of the steady oscillations. We define $\Delta T_1 = \frac{\Delta t_1}{T}$; $\Delta T_2 = \frac{\Delta t_2}{T}$, where T is the period of steady patterns. $\{\Delta T_1, \Delta T_2\}$ represents the initial conditions.
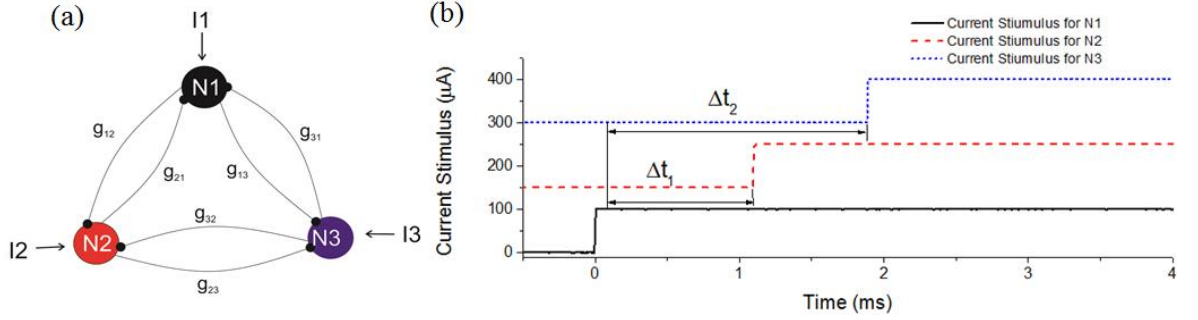
Figure 4.1 (a) Proposed asymmetric inhibitory triangle architecture of network model for generation of rhythms. N1, N2 and N3 represent the three neurons. Black dots represent electrical inhibitory synapses. g_{12}, g_{32}, g_{13}, g_{31}, g_{23}, g_{32} is the synaptic conductance. Each neuron is stimulated by an independent direct current (I1, I2, and I3 for N1, N2 and N3 respectively). Neurons compete with each other for firing due to the inhibitory connection. The firing sequence is determined by both coupling strengths and the current stimulus. (b) Input current steps at 100 µA are applied to neuron 1, 2 and 3 with offsets of Δt_1 (between N1 and N2) and Δt_2 (between N2 and N3). These delays are varied from 0 to one steady oscillation period to change the initial conditions of individual neurons in the CPG.

4.2.2 How to Map the WLC Dynamics

We use a phase lag map to demonstrate the dynamics of outputs of the CPG hardware and identify the stable attractors.

We plot the phase lag map by calculating the delays between peaks of spikes from neuron 2 and 3 relative to that from the reference neuron 1. We define ΔT_{i1}^n (i=2, 3) as the time position of the nth peak of neuron i relative to the time position of the nth peak of neuron 1. Figure 4.2 shows how we calculate ΔT_{21}^1 and ΔT_{31}^1 as an example. ΔT_{i1}^n is then normalized over the period of oscillations of the independently firing neuron as follows:

$$\Phi_{i1}^n = \frac{\Delta T_{i1}^n}{T} \tag{4. 1}$$

Where T is the period of steady oscillations of firing neurons in the network.
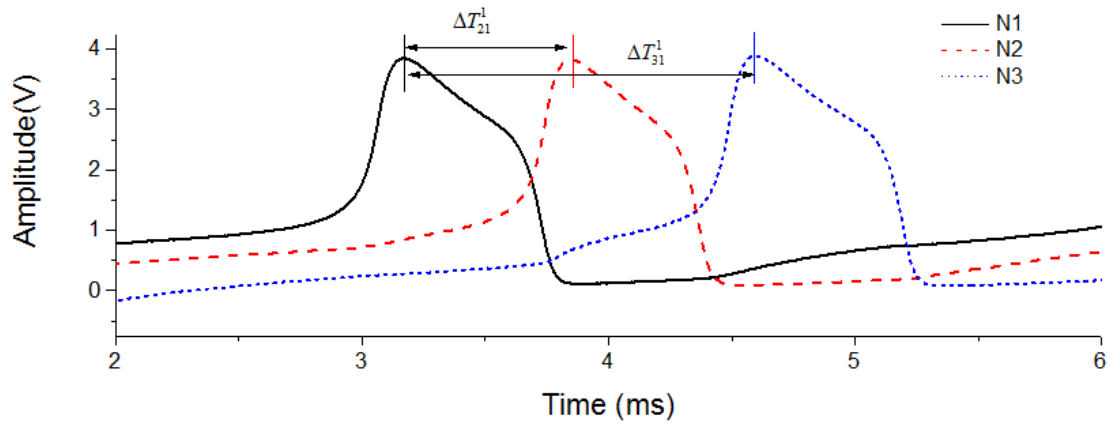
Figure 4.2 The time delay between the first peaks from different neurons. We use N1 as the reference neuron.

$\{\Phi_{21}^n, \Phi_{31}^n\}$ is the forward trajectory of the firing sequence. The maps are show in figure 4.4-4.6 and 4.8-4.9. We study the dynamical properties of the maps, including locating attractors, identifying corresponding rhythmic patterns, and seeking the possible number of attractors under particular coupling strengths, etc.

4.2.3 Preparation of the LabVIEW Program

We used a NI6259 DAQ card controlled by the LabVIEW software to generate step Voltage stimulus and collect the electrical measurements. The DAQ card had three outputs which were programmed to apply step voltage with tuneable amplitudes and different timings. The input timing determines the time delay of inputs between neurons. Step voltage stimulus is then converted into direct current stimulus by voltage to current converter circuits. The circuits were discussed in Chapter 3. Besides the outputs, the DAQ card had three inputs for collecting the spiking trains produced by the three neurons. The spiking trains were then analysed by a threshold peak detector LabVIEW program. This program scanned the input spikes, searched for valid peaks and returned the locations of the peaks. Information on peak locations was then sent to the LabVIEW calculator for analysing the phase lag of the outputs from different neurons.

4.3 Results and Discussion

4.3.1 From Spiking Patterns to Limit Cycles

We are going to demonstrate in figure 4.3 that output patterns of the neural network have transient state and steady state. Patterns in steady state are corresponding a limit cycle in phase space. In this thesis, a limit cycle is a closed trajectory in phase space having the property that other trajectories spiral into it as time approaches infinity. And we express the dynamic process by showing $\{\Phi_{21}^n, \Phi_{31}^n\}$ trajectories.

Figure 4.3(a) shows a typical set of neuron oscillations from the time at which the current stimulus is applied to the time at which the system oscillates in the steady-state. Current steps of $100\,\mu A$ are injected into individual neurons at the same time. The initial condition is (ΔT_1=0.6, ΔT_2=0.7). The coupling strengths between neurons are g_{12}=g_{23}=g_{31}=16$\,\mu S$, g_{21}=g_{13}=g_{32}=45$\,\mu S$. The time course of the plot is 25ms. During the 25ms, there are eight periods of spiking patterns. The periods of patterns from N1, the time delay between spikes from N2 and N1 and the time delay between spikes from N3 and N1 in each period is marked in the plot. The time delays are normalized over the period of steady patterns T.

We show this set of neuron oscillations as an example because it presents obvious transient dynamics. The transient time lasts about 17ms. During the transient time, the frequencies of neurons are changing with time and the oscillations are aperiodic. We take N1 as an example. The initial period is about 3.3ms. It corresponds to the frequency of 303 Hz. Then the frequency gradually increases. In the steady state, the frequency of the periodic patterns is about 357 Hz. This is about 10% bigger than the frequency of isolated firing neurons, which is 323Hz. In addition, the amplitude of the spikes abruptly jumps at the beginning of the transient time. The first spike has amplitude of 3.9V. Then it returns to the normal amplitude of 3.7V after the second spike.

The time delay between spikes from N2 and N1 and time delay between spikes from N3 and N1 in each period has been marked in the plot and they are normalized by the period of steady patterns T. The fluctuation of the time delays during transient time indicates that the firing sequence of neurons intends to change. This results from the competition for firing between neurons. After transient time, the temporal winner has come up, the firing sequence is decided and output pattern of the network becomes regular.

Figure 4.3(b) shows the three dimensional projection of the CPG output. Each axis represents the oscillation voltage of one of the three neurons. The red dash line shows the limit cycle corresponds to the periodic patterns in the steady state in figure 4.3(a). The other parts of the projection show the chaos which is corresponding to irregular firing pattern in transient state. The whole orbit results from electrical activities bouncing from one neuron to another. It shows how the system evolves from transient state towards the steady state. The arrows along the trajectory indicate the direction of the evolution.

Figure 4.3(c) shows the forward trajectory $\{\Phi_{21}^n, \Phi_{31}^n\}$ according to time delays shown in figure 4.3(a). The length of the trajectory indicates the length of the transient time. The length of the transient time may vary with initial conditions. This will be demonstrated in phase lag maps in figure 4.4-4.6 and 4.8-4.9. The points from n1 to n5 correspond to the oscillations with varying periods in figure 4.3(a) and chaotic projection in figure 4.3(b). The points from n6-n20 correspond to the oscillations with a constant period in steady state in figure 4.3(a) and the limit cycle in figure 4.3(b).

Some properties of oscillation dynamics, such as the length of transient time, a $\{\Phi_{21}^n, \Phi_{31}^n\}$ trajectory, etc. may vary with initial conditions. However, patterns result from different initial conditions may have a common limit cycle and therefore $\{\Phi_{21}^n, \Phi_{31}^n\}$ trajectories result from different initial conditions may fall into the same attraction basin and converge at a common point, which is an attractor. We will demonstrate attractor dynamics in figure 4.4-4.9.
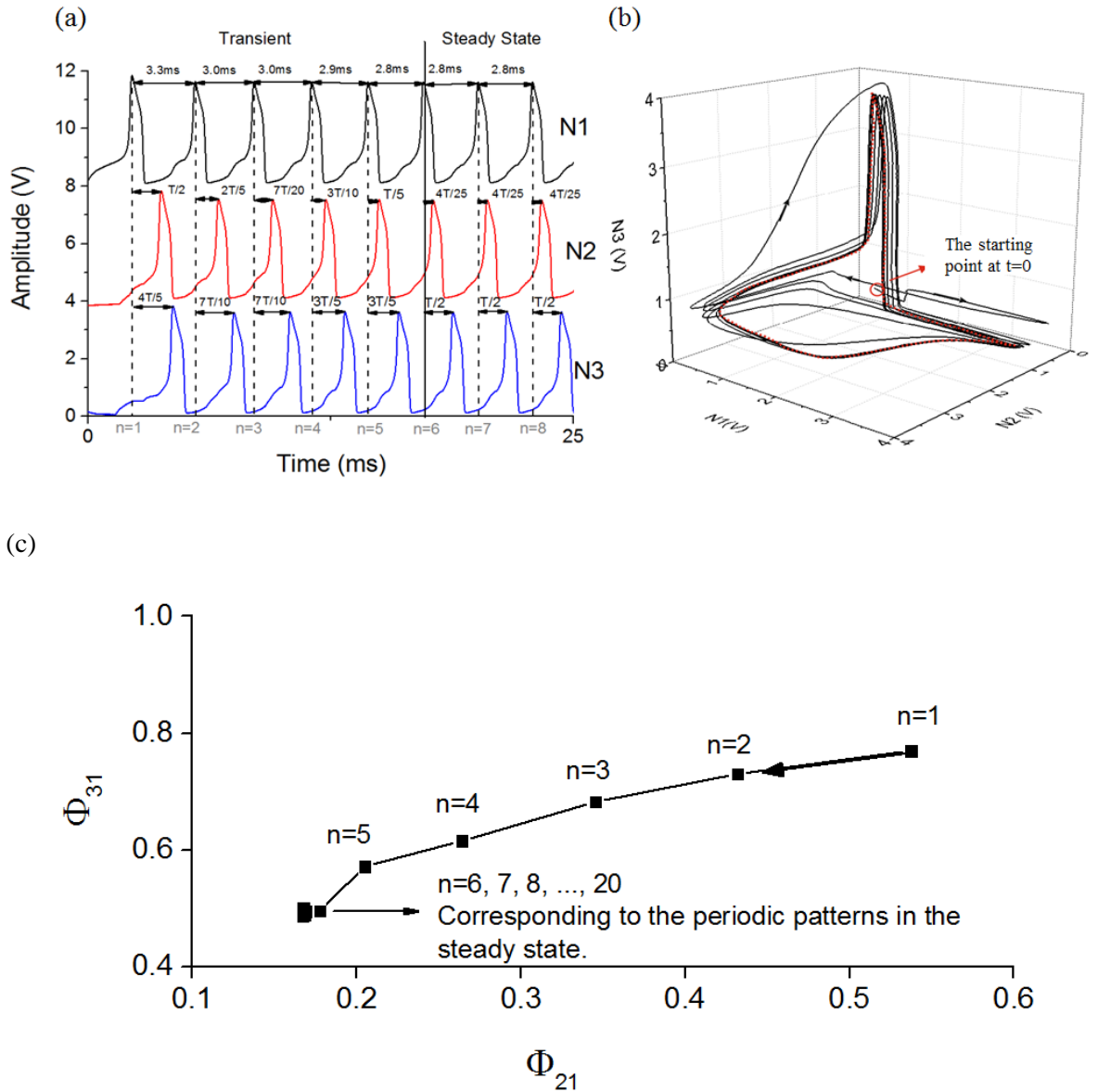
Figure 4.3 (a) Rhythmic patterns generated by the CPG when $g_{12}=g_{23}=g_{31}=16\,\mu s$, $g_{21}=g_{13}=g_{32}=45\,\mu S$. The magnitude of the stimulus current is $100\mu A$. The initial condition is ($\Delta T_1=0.6$, $\Delta T_2=0.7$). The sequential activity of the neurons results from the competition without winner in the system. There is a transient region at the beginning in which the firing sequence is irregular. In the following steady region, the firing sequence is cyclic and periodic patterns are generated. (b) The three dimensional projection corresponding to the oscillations shown in (a). In the plot, each axis represents an oscillation voltage from one individual neuron. The steady patterns in (a) are shown as a limit cycle in this phase portrait. It is highlighted by a red dash line. The other part of the orbit that looks chaotic corresponds to the transient regime. (c) The forward trajectory of the firing sequence $\{\Phi_{21}^n, \Phi_{31}^n\}$ (n=1, 2, 3…20). It is plotted according to the time delays shown in (a). N1-n5 indicates the transient time during which the time delays are varying. N6-n20 corresponds to the steady patterns which possess constant period and time delays. Spiking patterns in n9-n20 are not shown in (a) due to the limited space.

4.3.2 Mapping the Limit Cycle/Attractor Dynamics

In all the maps in figure 4.4-4.6 and 4.8-4.9, initial conditions are varied from ($\Delta T_1=0$, $\Delta T_2=0$) to ($\Delta T_1=1$, $\Delta T_2=1$) at the step of 0.05. There are about 20×20 trajectories in each map. Each trajectory corresponds to a specific initial condition.

Figure 4.4(a) shows the $\{\Phi_{21}, \Phi_{31}\}$ phase lag map when the coupling strength $g_{12}=g_{23}=g_{31}=45\,\mu S$, $g_{21}=g_{13}=g_{32}=16\,\mu S$. The coupling strength indicates that the neuron sends a stronger synaptic current in the direction of N1➔N2➔N3.

We highlight four trajectories by green colour in the map to demonstrate that the length of trajectories can vary with initial conditions. The number of data points along the trajectory indicates the number of periods that the spiking pattern has in transient time.

There is a phase shift in y-axis values in the map. The range of Φ_{31} of trajectories is between 0.1-1.1 rather than between 0 and 1. Some of the trajectories even possess a value of Φ_{31} that is beyond 1.1. This is because in comparison to spiking patterns in steady state, spiking patterns in transient state have longer period. And during transient time, time delays between spikes from different neurons can be bigger than one steady period. We take a pattern results from the initial condition ($\Delta T_1=1$, $\Delta T_2=1$) as an example to demonstrate this. As shown in figure 4.4(b), the first period of spikes of N1 is 3.5ms. It is 25% bigger than the period of steady patterns. Spikes of N3 also have longer transient periods. The time delay between spikes from N1 and N3 in the first oscillation period is about $\frac{11}{10}T$. This is shown as a data point with y-axis value of 1.1 in the right green line in the map. The phase shift resulted from longer periods of firing neurons in transient time indicates that electrical activation of neurons are delayed. It can be a evidence of inhibitory effect in the neural network.

Totally two attractors are found in the map. One is 'a1' at $\{\Phi_{12} \approx 0.16, \Phi_{31} \approx 0.49\}$, the other is 'a2' at (0.62, 0.30). They represent activation paths (N1➔N2➔N3) and (N1➔N3➔N2) respectively. The two steady patterns corresponding to the two attractors are shown in figure 4.4(c). In the map, (0, 0) is avoided as the neuron cannot fire all in phase due to the inhibitory connections. The two attractor basins are divided by a space (marked by dash lines in the map) where there are no trajectories. The trajectories are repeatable in other quadrants (not shown in the map). The black attractor basin possesses a

bigger area than the red one. It indicates that the system prefer generating the rhythmic pattern corresponding to attractor a1.

The geometry of the map demonstrates the sensitivity and robustness of the dynamics of the system. The output of the system is sensitive to external stimulus as stimulus with different initial conditions will lead to different trajectories. It is robust because small noise perturbation will only cause the system to gravitate around the attractor. And every trajectory is stimulus deterministic and reproducible. Therefore we are able to select rhythmic outcomes by selecting initial conditions. It indicates that we can control the rhythm of the neural system by timing the input pulses.

All these dynamical properties, including the stimulus determined spatiotemporal patterns, robustness, sensitivity, suggest that the system is a winnerless competition system [18]. Competition between neurons results in the sequential activation of neurons. The activation path in the network is unique for every stimulus. In this way, similar stimulus can be distinguished as they correspond to different patterns during transient time. However, the transient activation paths will fall into an attraction basin and converge at an attractor. This process can be applied to explaining the brain functions such as neocognitron [86], associated memory [87], etc.

We then tune the asymmetry of the coupling strength to study the influence of it on the characteristics of the map, such as changing in the area of attraction basin, resolution of boundaries, and the number of attractors.

Figure 4.4 (a) Phase lag map for the synaptic conductance $g_{12}=g_{23}=g_{31}=45\,\mu S$, $g_{13}=g_{32}=g_{21}=16\,\mu S$. The magnitude of the current stimulus we used for obtaining this map is $100\,\mu A$. The frequency of the steady pattern is 357Hz.Two attractors are found in the map: a1 (0.16, 0.49), a2 (0.62, 0.30). (b) The spiking pattern results from the initial condition ($\Delta T1=1$, $\Delta T2=1$). It shows longer period in transient state. And the time delay between spikes from N1 and N3 can be bigger than one steady period. (c) Rhythmic patterns correspond to the two attractors.

The map in figure 4.5 is obtained by exchanging the values of g_{13} and g_{31}. The current stimulus is the same as in figure. 4.4. For neuron 1, the synaptic current sent out is stronger than received. For neuron 3, the synaptic current received is stronger than sent out. Thus the activation of neuron 3 is more inhibited. The time delays between spikes from neuron 1 and neuron 3 in transient time are smaller. In the map, this is demonstrated as trajectories intend to start from the locations above the attractors.

In the map, still two attractors are found. One is 'a1' at $\{\Phi_{12} \approx 0.16, \Phi_{31} \approx 0.36\}$, the other is 'a2' at (0.64, 0.30).In comparison to the attractors in figure 4.4 (a), the location of a1 is slightly lower while the position of a2 moves slightly to the right. Besides, the a1

85

attraction basin seems to grow at the expense of the a2 attraction basin. This means that the limit cycle represented by the attractor a2 is becoming increasingly fragile. The firing sequence of N1→N2→N3 represented by attractor a1 may be easier than the firing sequence of N1→N3→N2 represented by attractor a2.
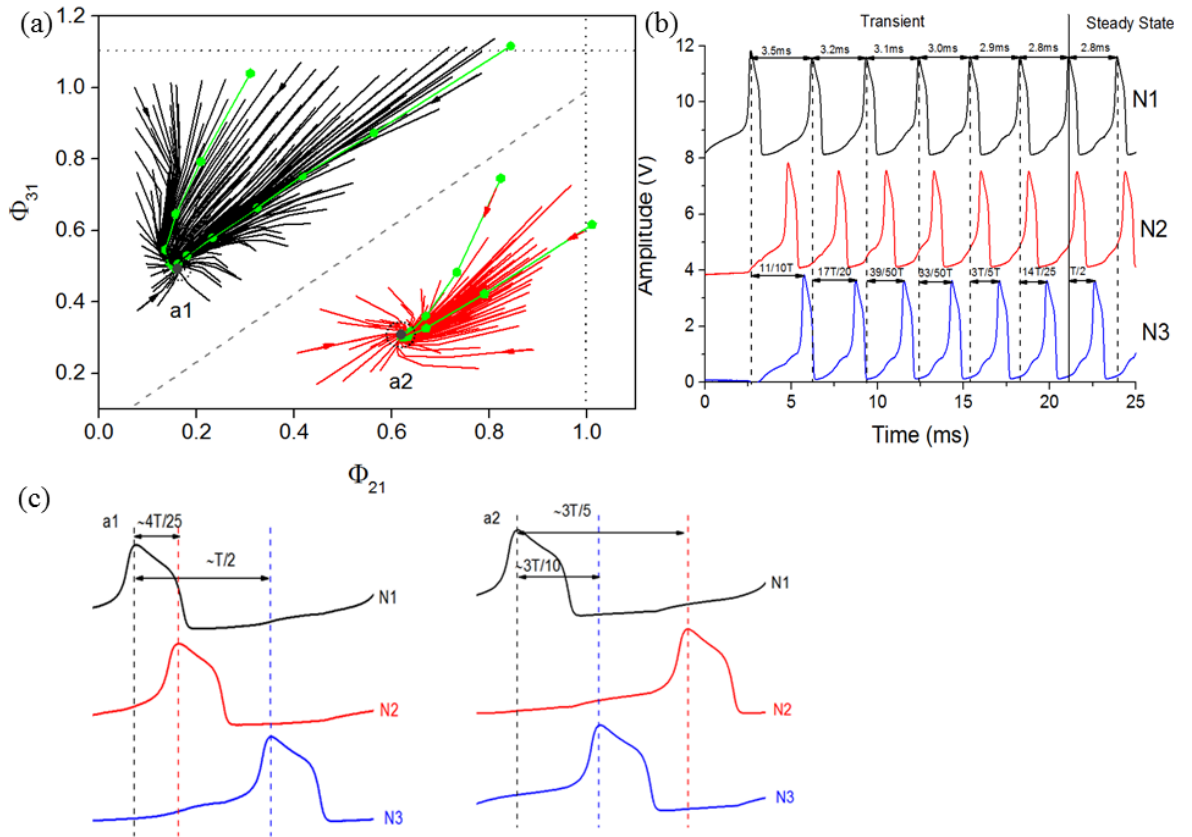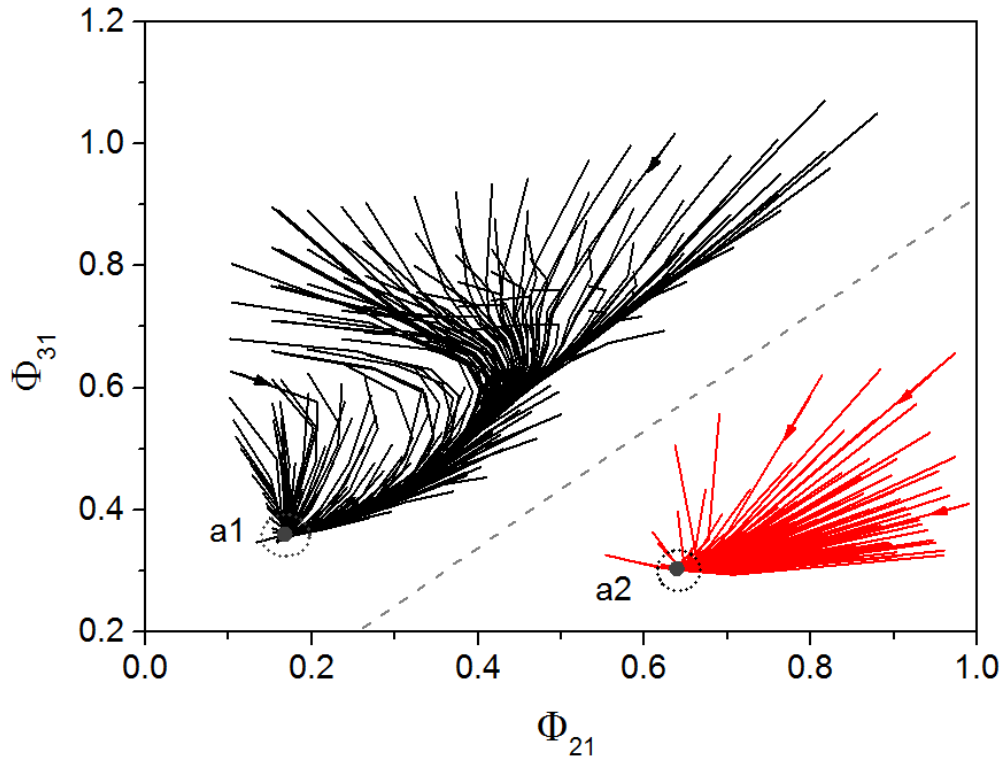

Figure 4.5 Phase lag map for the synaptic conductance $g_{12}=g_{23}=g_{13}=45\,\mu S$, $g_{31}=g_{32}=g_{21}=16\,\mu S$. The magnitude of the current stimulus we used for obtaining this map is $100\,\mu A$. The frequency of the steady pattern is 357Hz. Two attractors are found in the map: a1 (0.16, 0.49), a2 (0.64, 0.30). The locations of them are nearly the same with that in Fig. 6(a).

The map in figure 4.6(a) is obtained by weakening the asymmetry of the synaptic strengths. $g_{12}=37.2\,\mu S$, $g_{21}=23.5\,\mu S$, $g_{13}=20\,\mu S$, $g_{31}=45\,\mu S$, $g_{23}=39\ \mu S$, $g_{32}=20\,\mu S$. This set of synaptic values introduces a third attractor in the map. The locations of them are: a1 (0.21, 0.56); a3 (0.43, 0.61); a2 (0.74, 0.34). Rhythmic patterns corresponding to the three attractors are shown in figure 4.6(b). Attractors a1 and a3 suggest that two neurons intend to fire in phase while the third one fires out of phase with the other two. The map possesses longer

trajectories which demonstrate longer transient regimes associated with more symmetric coupling strengths.

The area of the attraction basin that represents the activation path N1→N3→N2 possesses almost the same shape with that in figure 4.4 and figure 4.5. The attraction basin for the activation path N1→N2→N3 collapses into two areas. The attractor a1 represents a pattern in which the N1 and N2 intends to be synchronized. The attractor a2 represents a pattern in which the N2 and N3 intends to be synchronized. There is no space between attraction basin a1 and ad although the boundary between them is clear.

This map suggests the possibility of increasing the number of rhythms of the neural network by tuning the asymmetry of coupling strengths.

In comparison to the map in figure 4.5, the attraction basin for the activation path N1→N2→N3 is obviously growing. And the attraction basin for the activation path N1→N3→N2 is reducing. It indicates that the firing sequence of N1→N2→N3 is easier than the other one when the synaptic strengths are less asymmetric.
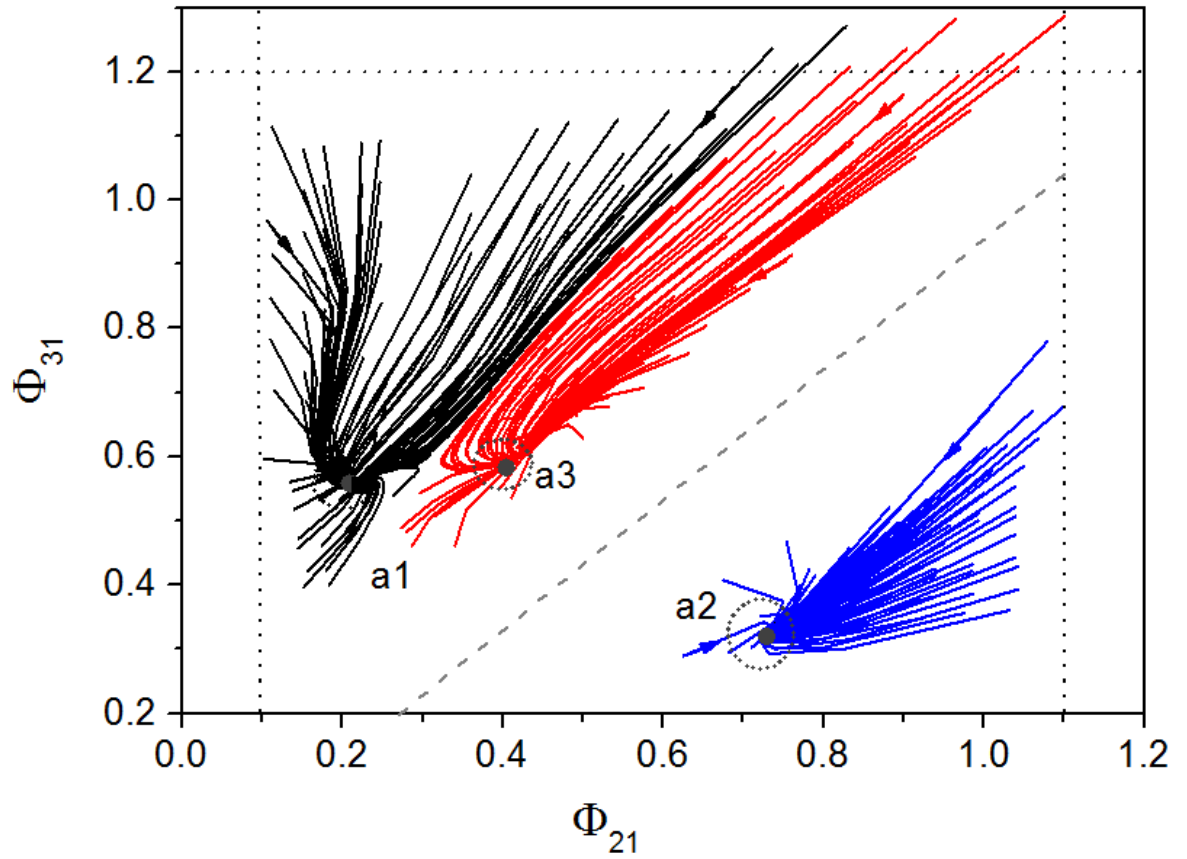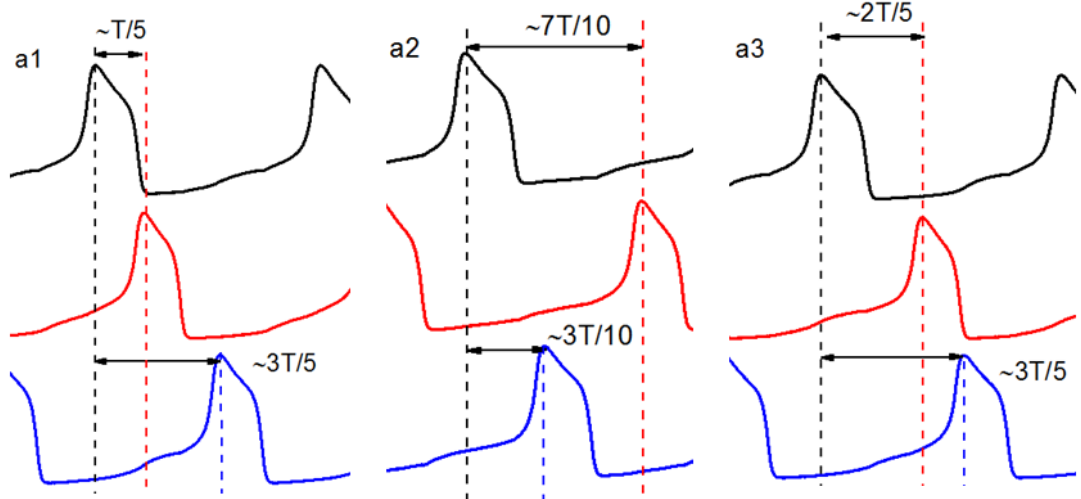
Figure 4.6 (a) The phase lag map resulted from the coupling strength g_{12}=37.2 μS, g_{21}=23.5 μS, g_{13}=20 μS, g_{31}=45 μS, g_{23}=39 μS, g_{32}=20 μS. The magnitude of the current stimulus we used for obtaining this map is 100 μA. The frequency of the steady pattern is 357Hz. Three attractors are found in the map: a1 (0.21, 0.56); a2 (0.74, 0.34); a3 (0.43, 0.61). (b) Rhythmic patterns correspond to the three attractors.

The changing in areas of attraction basins and number of attractors have been reported in theory in Wojcik's paper in 2011[55]. The configuration of their three neuron motif, stable spiking-bursting patterns generated by the motif and phase-lag maps are shown in figure 4.7 as a comparison to our experimental results.

Figure 4.7(a) is the three neuron motif. Wojcik et al proposed three spiking-bursting neurons reciprocally coupled by inhibitory synapses. The initial synaptic strengths are symmetric and $g_{syn} = 5 \times 10^{-3}$nS. The asymmetry of the motif is governed by another bifurcation parameter $g_\circlearrowleft$, which enforces/weakens counter-clockwise/clockwise coupling strengths $g_c^{cc} = 5 \times 10^{-4} \times (1 \pm g_\circlearrowleft)$ $(0 \le g_\circlearrowleft \ll 1)$. The initial conditions of the phase-lag maps are the timing of injecting synaptic currents.

Figure 4.7(c) shows the phase-lag map for the symmetric bursting motif at $g_{syn} = 5 \times 10^{-3}$nS. It shows five attractors corresponding to the five stable patterns shown in figure 4.7(b). The geometry of the map suggests that the five robust rhythms have nearly equal odds.

Figure 4.7(d) shows the phase-lag map for the asymmetric bursting motif at $g_\circlearrowleft = 0.154$nS. In this map, the attractor corresponding to the rhythm $(1 < 2 < 3)$ expands its attraction basin at the expense of the other four. And as $g_\circlearrowleft$ increases to 0.154nS, the three attraction basins related to rhythms $(1 \perp \{2 \parallel 3\})$, $(2 \perp \{1 \parallel 3\})$ and $(3 \perp \{1 \parallel 2\})$ move toward to the attraction basin related to the stable pattern $(1 < 3 < 2)$ and therefore narrow its area. Figure 4.7(e) shows that increasing $g_\circlearrowleft$ makes the attraction basin related to rhythm $(1 < 2 < 3)$ globally dominant after the three nearby attraction basins collapse onto the attraction basin related to rhythm $(1 < 3 < 2)$.
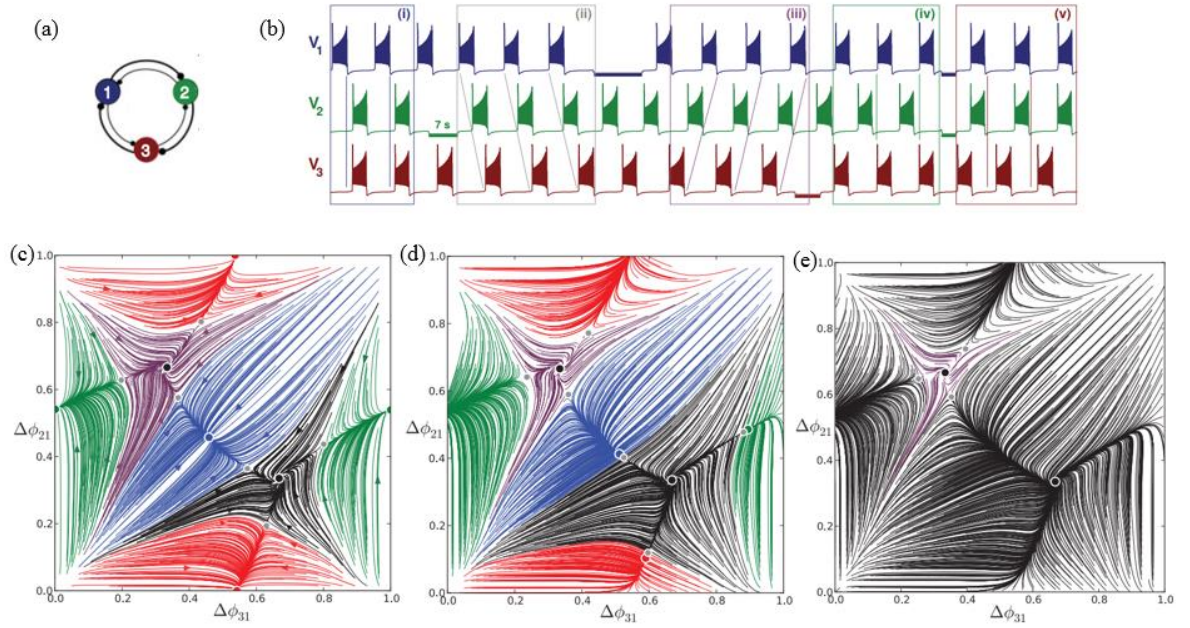
Figure 4.7 The configuration of the motif with three inhibitory connected neurons and the results showing changing in areas of attraction basins and the number of attractors from Wojcik's theory [55]. (a) The three neuron motif with asymmetric clockwise vs counter clockwise connection strengths. The neurons are spiking bursting neurons. (b) Five rhythms in the bursting motif at $g_{syn} = 5 \times 10^{-3}$nS: $(1 \perp \{2 \parallel 3\})$ in episode (i), travelling waves $(1 < 2 < 3)$ in (ii), $(1 < 3 < 2)$ in (iii), $(2 \perp \{1 \parallel 3\})$ in (iv), and $(3 \perp \{1 \parallel 2\})$ in (v). (c) Phase-lag map for the symmetric bursting motif at $g_{syn} = 5 \times 10^{-3}$nS showing five attractors corresponding to the five patterns in (b); (d) Phase-lag map for the asymmetric bursting motif at $g_\circlearrowleft = 0.154$ nS; (e) Phase-lag map for the asymmetric bursting motif at $g_\circlearrowleft = 0.3$ nS. Plots in this figure is from ref. [55].

After a brief review of Wojcik's theory work, we carry on with our experimental maps. In the maps in figure 4.8, the coupling strengths are the same as in figure 4.6 while the magnitude of current stimulus is increased to it influence on the maps.

The map in figure 4.8 (a) results from current of 1.2 μA. The firing frequency of the steady pattern is 417Hz. The map in figure 4.8(b) results from current of 1.4 μA. The firing frequency of the steady pattern is 455Hz. Corresponding to the bigger firing frequency, we expect to obtain shorter transient regime, which will be expressed in the form of rapid convergence from the edges of the basin to the attractor. However, in both of the maps, trajectories become even longer while firing frequency is increasing. Also, the distribution of trajectories is more disperse. The possible reason for longer and more dispersed

trajectories is that increasing current stimulus can increase the synaptic current and finally result in a stronger inhibition effect. Enforcing the inhibition effect can delay the firing of neurons and increase time delays between spikes from different neurons and lead to slower convergence from the edges of the basin to the attractors.

Both of the maps in figure 4.8(a) and (b) demonstrate two rhythms: (N1→N2→N3) and (N1→N3→N2). In comparison to figure 4.6, the attractor that indicates N2 intends to firing in phase with N3 has disappeared. Only two attractors are left. Locations of the two attractors in figure 4.8(a) are: a1 (0.19, 0.55); a2 (0.68, 0.25). Locations of the two attractors in figure 4.8(b) are: a1 (0.20, 0.67); a2 (0.75, 0.27). From figure 4.6 to figure 4.8 as the synaptic strengths are stronger, the attraction basin a1 seems expanding and annexed the nearby attraction basin. And from figure 4.6(a) to (b), as the synaptic strength is even stronger, the attraction basins are moving towards the right of the map.
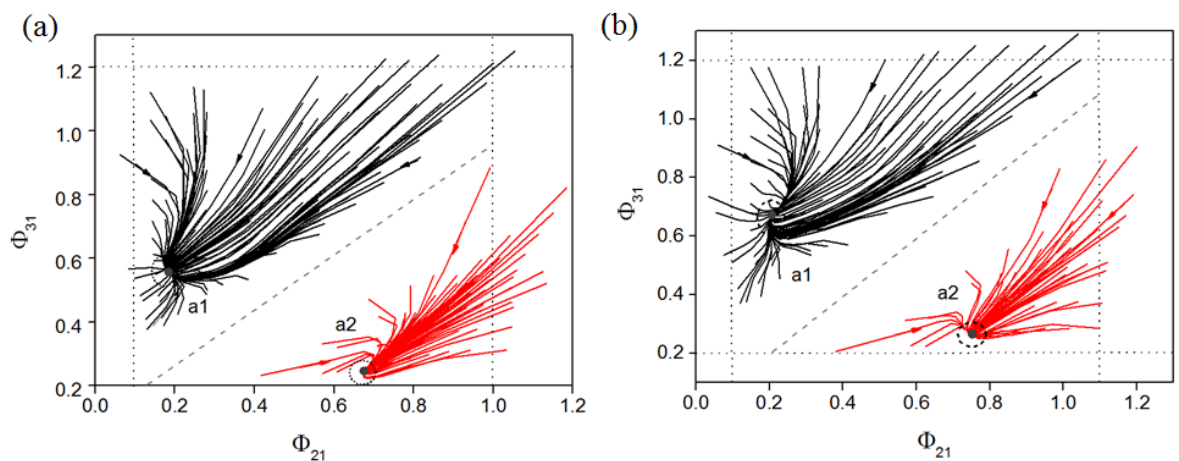
Figure 4.8 The coupling strengths are the same with that in figure 4.6. (a)The frequency of the steady pattern is increased from 357Hz to 417Hz as the magnitude of current stimulus is increased from 1V to 1.2V. Two attractors are found in the map: a1 (0.19, 0.55); a2 (0.68, 0.25). (b) The frequency of the steady pattern is increased from 417Hz to 455Hz as the magnitude of current stimulus is increased from 1.2V to 1.4V. Two attractors are found in the map: a1 (0.21, 0.67); a3 (0.75, 0.27).

4.4 Summary

We made a multifunctioal CPG consisting of three analogue neurons interacting with each other via inhibitory synapses in hardware. A maximum of three rhythms can be produced

by the hardware. The mechanism underlying the producing of rhythmic patters is the winnerless competition principle. The capability of producing rhthms is sensitive to the coupling strenghs as well as the intensity of current stimulus. Less asymmetry coupling strengths can lead to more steady rhythms. Swithing between rhythms can be controlled by initial conditions represented by the time delay between input current.

Varying the strenghs and asymmetry properties of synaptic strenghs can lead to the changing in numbers and areas of attraction basins. This result agrees well with the theory propsed by Wojcik et al[55].

Chapter 5 Modulation of Respiratory Sinus Arrhythmia in Rats

5.1 Introduction

As discussed in chapter 4, CPG can regulate biological rhythms and coordinate motor activity [44, 78]. One kind of rhythm generators is a half-centre oscillator [88]. It consists of two neurons that are reciprocally inhibitory connected. When one neuron fires, the other is hyperpolarized and vice versa. In this way the two neurons burst out of phase with each other and generate biphasic rhythm. These neurons regulate behaviours in invertebrate such as Clione swimming [89], leech heartbeat [57, 90], etc. We have demonstrated in chapter 3 that we have fabricated artificial neurons in hardware, which can produce realistic spiking patterns in real time, and reciprocally connected them via inhibitory synapses. In this way, the artificial neural network can generate out of phase rhythm patterns. As demonstrated in chapter 4, maximum tri-phasic rhythms can be generated by an artificial CPG board. The study in chapter 3 and chapter 4 indicates that our CPG can potentially model the function of generating rhythms of biological CPGs such as half-centre oscillators.

Another example of a biological CPG, which is crucial for our experiment in this chapter, is the respiratory CPG located in the lower brain stem [91]. It can generate motor patterns during respiratory cycles in mammals. In biology, a part of a respiratory cycle is called a phase. A respiratory cycle is considered to consist of three phases: inspiration, post-inspiration and expiration [92]. These respiratory phases can be recognized in the activities of three neurons of the pre-Bötzinger centre in the medulla which are coupled via mutually inhibitory synapses [93] as in the CPG shown in chapter 4. One of these neurons control respiration by controlling the diaphragm through signals sent via the phrenic nerve. Phrenic nerve recordings show activity peaks during inspiration.

In this chapter, we design an artificial CPG which can generate tri-phasic rhythms [69]. In vivo experiments, we use phrenic signal to stimulate the CPG and synchronize motor patterns output by the CPG to respiration. The output patterns by the CPG are used to modulate the heart rate by stimulating the cardiac vagal moto neurones.

The aim of the modulation is to restore the coupling between the heart rate (HR) and the respiratory cycle. The coupling makes the heart beats faster during inspiration than that in expiration. This phenomenon is known as respiratory sinus arrhythmia (RSA). Because of

RSA, blood can be pumped faster to facilitate oxygen exchange with the blood during inspiratory phase. Therefore RSA is believed to increase blood pumping efficiency and improve cardiac function [91, 94-97]. RSA is found in healthy and fit subjects. The loss of RSA can lead to cardiovascular diseases, including heart failure [98], hypertension and even sudden cardiac death [99]. Research on medical side has revealed that the RSA in animals is achieved by synchronizing the cardiovascular and respiratory oscillators through phase or frequency locking [100-103]. In this chapter, we will use the artificial CPG to generate two and three phase rhythms and assess whether it could control the heart rate of rats such that the heart rate could be lowered in each of the three respiratory phases.

By artificially inducing the RSA, we will demonstrate that the artificial neuron stimulation may provide novel therapies aimed at either retraining natural central pattern generators or even substituting them with prosthetic CPG implants. The artificial CPG has advantages of being easy to program and to modify [104-106], etc.

All the surgeries on rats were done by Professor Julian Paton's group, who work in school of physiology and pharmacology in university of Bristol and hold the permission for animal experiments.

5.2 Experimental Methods

5.2.1 Information Background

RSA is pronounced in fit, healthy subjects: the heart rate (HR) increases during inspiration and decreases during expiration. In this way, the HR is coupled to the respiratory cycle. RSA is understood to be the modulation of cardiac vagal efferent activity by the respiratory rhythm[107]. It can be measured by measuring periodic changes in the HR during the respiratory cycle.

Phrenic nerve (PN) is important for keeping the body breath because it passes motor information to the diaphragm and receive sensory signals from it. Phrenic signal is synchronized with inspiration phase of a respiratory cycle. Therefore in the experiments we use the phrenic signal to stimulate N1 on the CPG board in order to synchronize N1 with inspiration phase. An example of phrenic signal after being rectified and filtered is shown in the top panel in figure 5.1. The figure also demonstrates how we divide a respiratory cycle into three phases: inspiration ($\varphi1$), early expiration ($\varphi2$) and late expiration ($\varphi3$). This is different from that in medical science as they divide a respiratory

cycle into phases of inspiration, post inspiration and expiration. Our dividing method is for the technique convenience.

The heart rate (HR) is controlled by the vagal signals, which are conducted from the medulla to the atrioventricular node and have the effect of lowering HR. Therefore we are able to modulate HR in the experiments by using output of the CPG to stimulate the vagus nerve (VN). Besides, the vagal signal starts at the end of inspiration phase. In this experiment, we use vagal signal to determine the duration of early expiration phase. An example of vagal signal and its position relative to phrenic signal is shown in the bottom panel in figure 5.1.
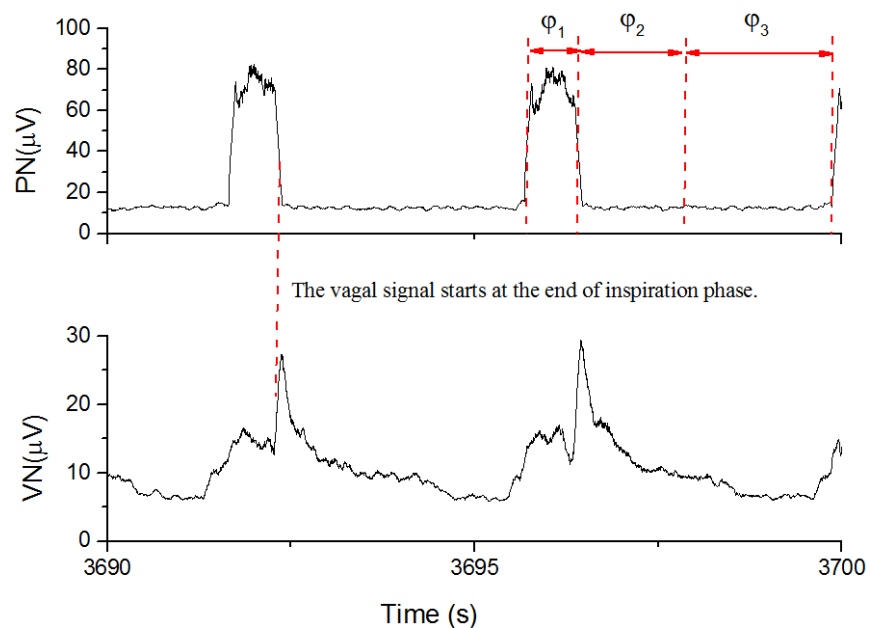
Figure 5.1 An example of phrenic and vagal signal and the relative positions of them. In our experiment, a respiration cycle is divided into three phases: the inspiration phase ($\varphi1$), early expiration phase ($\varphi2$) and the late expiration phase ($\varphi3$). The duration of inspiration phase is about 0.6-0.8s. The duration of early expiration is determined according to the duration of vagal signal. It lasts about 0.7s. We use phrenic signal to synchronize N1 on the CPG board with inspiration phase. And we use vagal signal to synchronize N1 on the CPG board with the early expiration phase.

5.2.2 Preparation of the In Vivo Experiments

The setup of the live experiments is shown in figure 5.2. The artificial CPG receives input from the phrenic nerve and produces voltage oscillations that are used to stimulate the cut

peripheral end of the vagus nerve. The raw phrenic signal consists of fast voltage oscillations with both plus and minus values during the inspiratory phase. This signal will be amplification, rectification, smoothing and conversion to a current to stimulate the CPG. The processing is done electronically in the series of steps depicted in figure 5.2(a). The raw phrenic signal is first amplified 10,000 times by a pre-amplifier and band pass filtered (80 Hz to 3 kHz) in order to filter out noise. The signal is then amplified by a second amplifier on the CPG board that has a gain tuneable in the 1-20 range. This step is for finely adjusting the amplitude of the stimulus relative to the firing the threshold of N1. The next stage is injecting amplified phrenic signal into the diode and a second order low pass filter circuits which are constructed on the CPG board. The purpose of this stage is to rectify and smooth the signal. The phrenic voltage (VPN) is then converted into a current (IPN) by a transconductance differential amplifier performing the function $I_{PN} = GV_{PN}$ where G=0.1mS. The current IPN is then injected into N1. N1 or N2 then modulates the heart rate through stimulation of the cut peripheral end of the vagus nerve (VN).
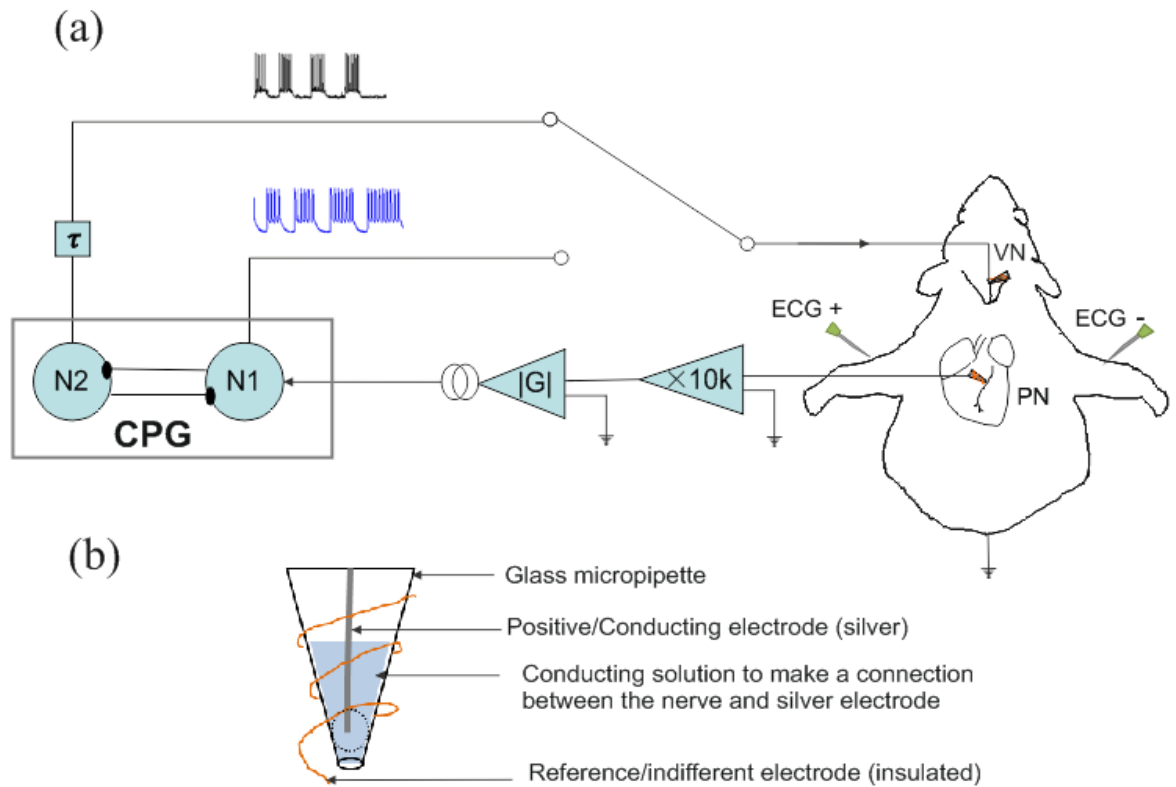
Figure 5.2 (a) A schematic diagram of the in vivo experiment with a decerebrated rat. Suction glass electrodes are attached to the thoracic phrenic nerve (PN) and central vagus nerve (VN) to record inspiration patterns and vagus activity respectively. Electrocardiogram (ECG) and perfusion pressure were also recorded in order to monitor the heart rate and blood pressure. The ECG signal is collected by two stainless steel needles. The setup for recording the perfusion pressure is not shown in the diagram because it is not my work. It is provided by collaborators who work on the medical side of the experiments. A pre-amplifier stage magnifies the phrenic signal by 10,000 and produces quasi-rectangular voltage pulses during inspiration. A second amplifier stage rectifies and smoothes the pre-amplified signal. And the voltage gain of the second stage is used to fine tune the amplitude of phrenic pulses relative to the firing threshold of neuron 1 (N1). The voltage pulses are then converted into current pulses which are used to stimulate N1. N1 and N2 are silicon neuros that interacted via reciprocally inhibitory synapses. They oscillate out of phase with each other. The voltage oscillations of N1 are used to stimulate the vagus nerve in phase. N2 provides the stimulation out of phase and third phase. (b) Schematic diagram of structures of a glass suction electrode. It consists of a glass micropipette with conducting solution, a positive electrode inside the micropipette and a reference electrode round the micropipette.

We used two juvenile rats for modulating the heart rate. In situ rats preparation described in this paragraph was done by collaborators who work on medical side of the experiment. The process can be found in Ref [108]. Rats were deeply anaesthetized by Halothane. The evidence of the successful anaesthesia is loss of withdrawal response to noxious pinching of the tail and paws. Rats were bisected beneath the diaphragm and exsanguinated. The head and thorax were cooled in ice-chilled ringer's solution. The composition of the solution is (in mM): NaCl (125); $NaHCO_3$ (24); KCl (3); $CaCl_2$ (2.5); $MgSO_4$ (1.25); KH_2PO_4 (1.25); dextrose (10). The pH is in the rage of 7.35-7.4 after carbogenation. All chemicals were from Sigma (UK) containing 1.25% ficoll, gassed with carbogen, filtered by 25 μm screen filter and warmed at 31^oC. Perfusion pressure was set to around 70-80 mmHg by increasing flow rate to $25ml.min^{-1}$ and arginine-vasopressin to the perfusate (200-400 pM). The perfusion pressure (PP) is recorded during experiments in order to monitor the blood pressure. Electrodes were put on the rat for collecting signals, including ECG signal, phrenic signal, and also for stimulating the vagus nerve. Figure 5.2(a) shows all the electrodes on the rat. Electrocardiography (ECG) signals were recorded by two stainless steel needles sitting on left and right arms respectively. Besides, glass suction electrodes were used here. Two suction electrodes were put on the left phrenic nerve and the left central end of the vagus nerve respectively to record the centrally generated respiratory activity. A third suction electrode was connected to the artificial CPG and used to electrically stimulate the cut peripheral end of the right vagus nerve. Ground electrode for the ECG signals is a piece of wire that connects to the bottom of the animal. In other words, the animal is placed over this wire and ground that goes into the amplifier is clipped onto this wire.

The glass suction electrodes were manufactured in the lab by Dr. Erin O'Callaghan in medical science laboratory in University of Bristol. Schematic of the structures are shown in figure 5.2(b). A silver positive electrode was dipped in the conducting solution within a micropipette. The glass suction holds the nerve up and the electrical signals from the nerve reach the silver electrode through the conducting solution. An insulated indifferent electrode was wound round the micropipette. Insulation is stripped about 1-2mm from the tip of this wire such that the tips of the indifferent electrodes can touch the outside of the nerve to provide reference signals.

All the electrodes have conductive wires attached to them. After electrodes are prepared and well attached on the rat, my collaborators who work on medical side finish their work.

I connect the wires with my CPG board, monitor the heart rate of the rat, and adjust the output of my CPG board according to the situation of the rat. For example, the intensity of the signal that is safe for the rat could be very different from rat to rat. Spikes with frequency of 30Hz can work well on one rat but kill another rat by reducing the heart rate too much. My collaborators who work on the medical side can only tell the situation of the rat, such as if the heart rate of the rat looks good, if the rat is dying, etc. They have no idea about the range of the firing frequency and amplitude of artificial neurons we can use.

5.2.3 Preparation of CPG Hardware

We used two neurons on the CPG board demonstrated in chapter 4 for initial trials. The trials provided information on how to modify the CPG board and what spikes are good for rats. According to the information, I fabricated a new CPG board specifically for this experiment. The new board include the CPG circuit and some auxiliary circuits, such as amplifiers, low pass filters, potential dividers, etc.

The CPG circuit consists of two silicon neurons connected by inhibitory synapses. The implementation of individual neurons and electrical synapses on the CPG board has been demonstrated in chapter 3.

Auxiliary circuits constructed on the board include a circuit that rectifies, delays and smoothes the phrenic signal (shown in figure 5.3), and a potential divider followed by a source follower circuit that can provides with tuneable and steady output voltages.

Figure 5.3 shows the circuit for rectifying, delaying and smoothing the phrenic signal. The diode is for removing the minus values of the phrenic signal. The RC integrator is for delaying the out of phase signal by extending the in phase signal. In this way, phase $\varphi 3$ signal is obtained. In the RC integrator, R is a variable resistance. The range of its value is between 0 and 5kΩ. C=100μF; R1=R2=5kΩ; C1=C2=4.7μF; R1' =R2' =5kΩ. The two second low pass filter is for smoothing the phrenic signal.
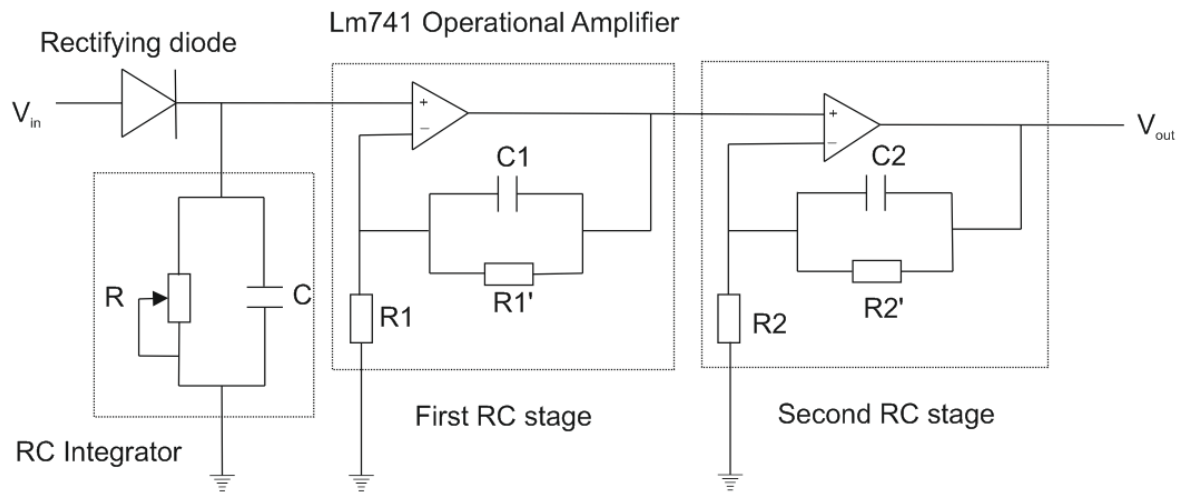
Figure 5.3 A diagram of the auxiliary circuits which reshape the phrenic signal. It consists of a diode, RC integrator, and a second order low pass filter. The diode rectifies the signal. The RC integrator delays the signal. The second order low pass filters smoothes the signal.

When connecting the output patterns with vagus nerve, we also need source follower circuits, which can keep the output voltages steady. The artificial neurons may be directly connected to the vagus nerve as in most experiments the input impedance of the vagus nerve is larger than the leakage resistance in our artificial neurons (10KΩ). Changes in conductivity of the ringer bath may however cause the impedance of the stimulation electrode to drop below 10kΩ decreasing the amplitude of neuron spikes. Therefore we need the source follower circuit to guard against attenuation of the output signal.

The output of the system is spiking patterns. The intensity of the stimulation needs to be controlled carefully. If the stimulation is too weak, it shows no effect on the vagus nerve of the rat. If it is too strong, a rat could be killed because of the big changing in heart rate. During experiments, we usually tune the intensity of the stimulation by tuning the amplitude and frequency of the spikes from the CPG. The amplitude can be easily tuned in the range of 0 and 3.7V by a potential divider circuit. The method of tuning the frequency has been demonstrated in chapter 3: it can be tuned by tuning the time constant of the Na and K gates together with the membrane capacitance. The frequency was chosen to fit bursts of about 5-10 spikes in the time interval of phrenic duration, which is corresponding to the inspiration phase. The inspiration phase lasts 0.6s-0.8s, thus the interval between

spikes had to be in the range 50-160ms for firing frequency of 6-20Hz. For the neurons we designed for this experiment, these are the typical frequencies obtained for a current stimulus of $100\,\mu A$. As discussed in chapter 3, the neurons have a firing threshold of $86\,\mu A$ and the firing frequency increases with increasing stimulation as in real neurons.

The photo of the prepared CPG board and its block diagram is shown in figure 5.3. The CPG board was designed to provide three phase stimulation, namely to selectively excite the vagus nerve during inspiration ($\varphi 1$), early expiration ($\varphi 2$) and late expiration ($\varphi 3$) as shown in figure 5.1. When excited by the phrenic input, N1 and N2 fires during phase $\varphi 1$ and phase $\varphi 2 + \varphi 3$ respectively. To stimulate phase $\varphi 3$ only, we introduce a time delay τ by building a RC circuit (figure 5.4) to slow the rise of the current stimulating neuron 2. To stimulate phase $\varphi 2$ only, we substitute the phrenic nerve with the input from central vagus nerve recording as input to N1. This is because the central vagus nerve activity contains not only central inspiratory activity but also post-inspiratory discharge. Since the latter has higher amplitude than the former this was used to trigger the firing of N1 at the onset of the early expiratory phase. We are able to tune the timing of N2 by controlling the moment at which its input current reaches the $86\,\mu A$ firing threshold.

In order to test the new board, we performed preliminary trials of synchronization to respiration by stimulating the artificial CPG with recordings of the phrenic nerve through a NI6259DAQ card from National Instruments. After the success with the preliminary trials, we then moved to the live experiments.

(a)
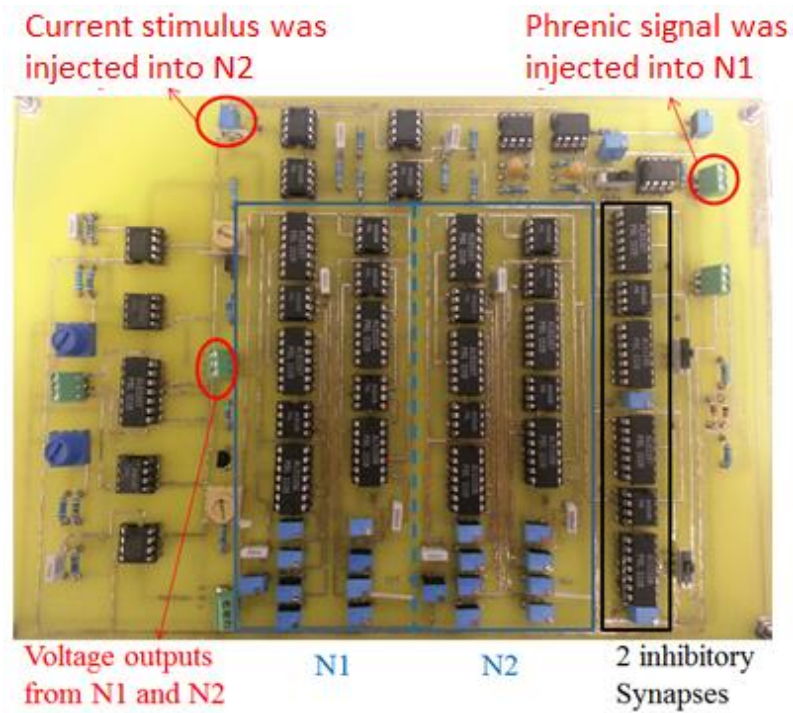
(b)
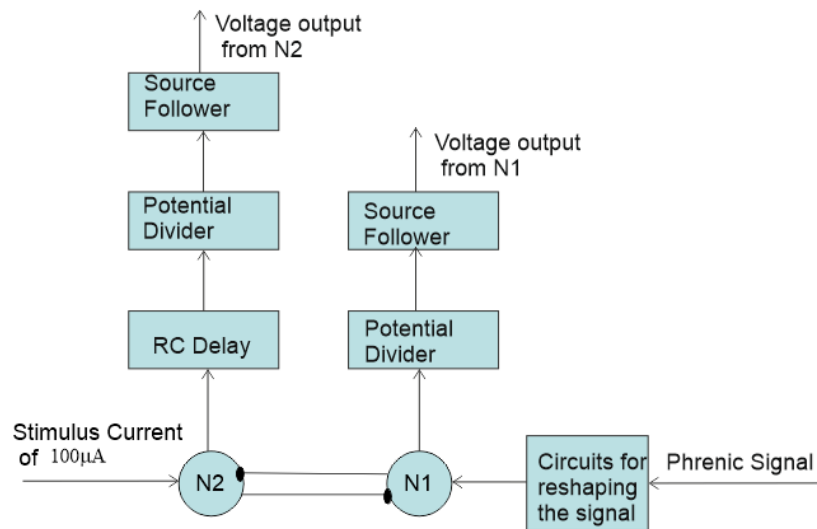
Figure 5.4 (a) The photo of the prepared CPG hardware. It consists of two silicon neurons (in the blue square) that interact with each other through reciprocally inhibitory synapses (in the black square) and auxiliary circuits (in other regions), such as circuits for reshaping the phrenic signal (demonstrated in figure 5.3), potential dividers and source followers, etc. (b) A block diagram showing the construction of the CPG.

5.3 Results

We show results from two juvenile rats. The natural activity of cardiorespiratory system of two rats without external modulation is shown in figure 5.5. The figure shows the ECG signals (bottom) and heart rate signals (top). When recording the ECG signals, we do not record the full electrical impulses produced by the heart. ECG signals in this chapter indicate the state that if there is an electrical impulse or not. If there is an electrical impulse, the number '1' would be written into the datasheet. Otherwise the number '0' would be recorded. And the ECG signals reflect the position of the peak of each electrical impulses produced by the heart. Then HR is calculated by taking the reciprocal of time delays of every two heartbeat. The HR shows the heart rate in time thus it is called instantaneous HR.

According to figure 5.5, the average heartbeat is 4.8 beats /s. This value is similar between the two rats. The natural RSA has a period of 4.1s and amplitude of 0.08Hz.
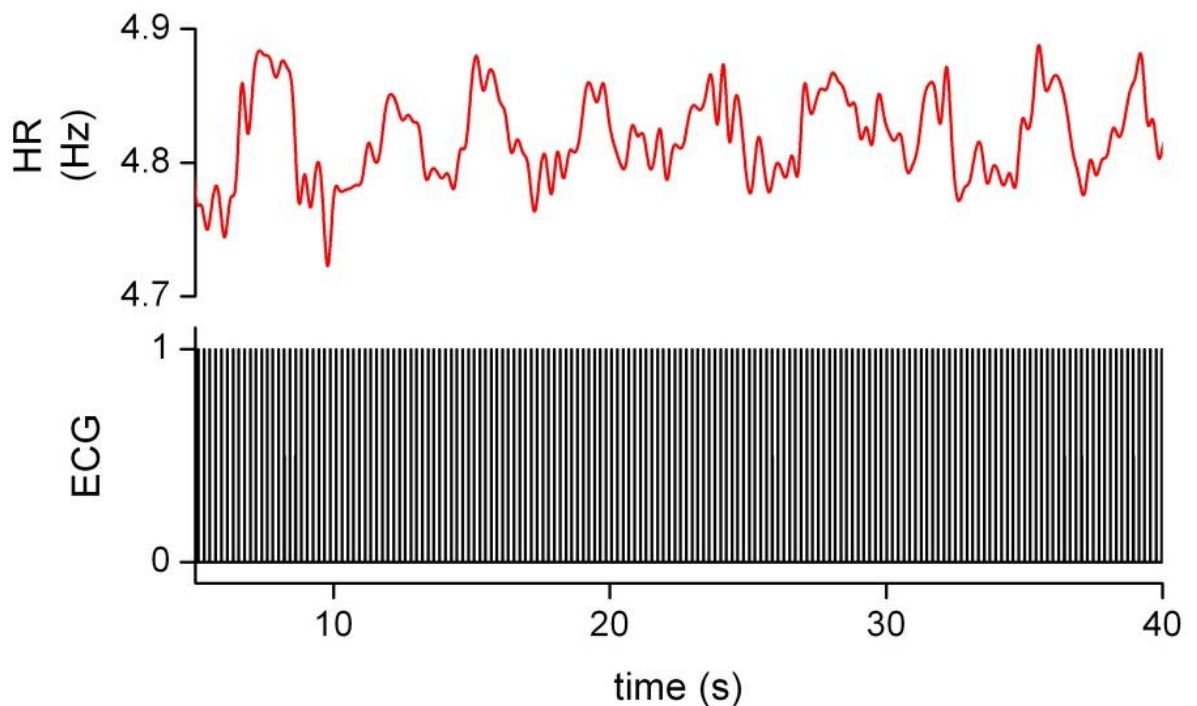
Figure 5.5 Natural respiratory sinus arrhythmia. The instantaneous heart rate (HR) was calculated from electrocardiogram (ECG) recordings of Rat 1. The ECG signals here only show information on the rate of electrical impulses. We used two rats during the experiments and they had similar average heart rate at 4.8 beats/s. The fluctuation of amplitude of the heart rate indicates the natural respiratory sinus. The natural RSA here has a period of 4.1s and amplitude of 0.08Hz.

During the experiments we used the silicon CPG to modulate the heart rate of rats. We expect to see Artificial Induced respiratory Sinus Arrhythmia (RIRSA). The evidence of that is the instantaneous heart rate oscillates in phase with the rhythm of respiration.

We then connected the output of artificial neuron 1, which fired in phase with phrenic signal to excite the vagus nerve. In other words, we modulated the heart rate during the inspiratory phase φ1. Results from rat 1 and rat 2 are shown in figure 5.6(a) and (b) respectively.

In figure 5.6, vertical axis PP represents the perfusion pressure, ECG represents the ECG signals, PN represents the phrenic signal, VN represents the vagal signal, N1 represents the output of artificial neuron 1, and N2 represents the output of artificial neuron 2. Electrical signals, including ECG, phrenic signal, vagal signal, output of artificial neuron 1, and output of artificial neuron 2, are collected by me. The perfusion pressure is provided by collaborators who work on the medical side of the experiment. We monitor the PP signal for two reasons. Firstly, it consists of small oscillations. Every oscillation corresponds to an electrical impulse produced by the heart. Therefore when we failed in collecting ECG signal, we calculated heart rate by counting the number of oscillations in PP signals. The amplitude of the oscillations in PP signal depends on quality of the measurement and it does not matter to our experiments. Secondly, the perfusion pressure reflects the blood pressure of the rat and it tells us if the rat is suitable for experiments. At the beginning of an experiment, the perfusion pressure of the rat is 70-80mmHg. During experiments, the perfusion pressure of rats would drop down. We need to finish the experiment when the perfusion pressure is above 50mmHg otherwise the rat would start to die.

In figure 5.6 (a), big fluctuation happened in the heart rate. The heart beat is slowed down from 4.8 beats/s to 2.5 beats/s. This indicates a strong RSA. This AIRSA makes the heart rate decrease during stimulation at a rate of $-3beats/s^2$. After the stimulation, the heart rate recovers and returns to its resting value at a rate of $+1beat/s^2$. In figure 5.6(b), we injected sodium cyanide into rat 2 for increasing the phrenic burst rate. As a result, the duty cycle of spiking patterns of the artificial CPG increases. The time for the heart rate to recover is then reduced. It leads to the weaker oscillation amplitude at 3beats/s for rat 2. In both rats, the spiking patterns from CPG board remain perfectly synchronization with respiration rhythm.
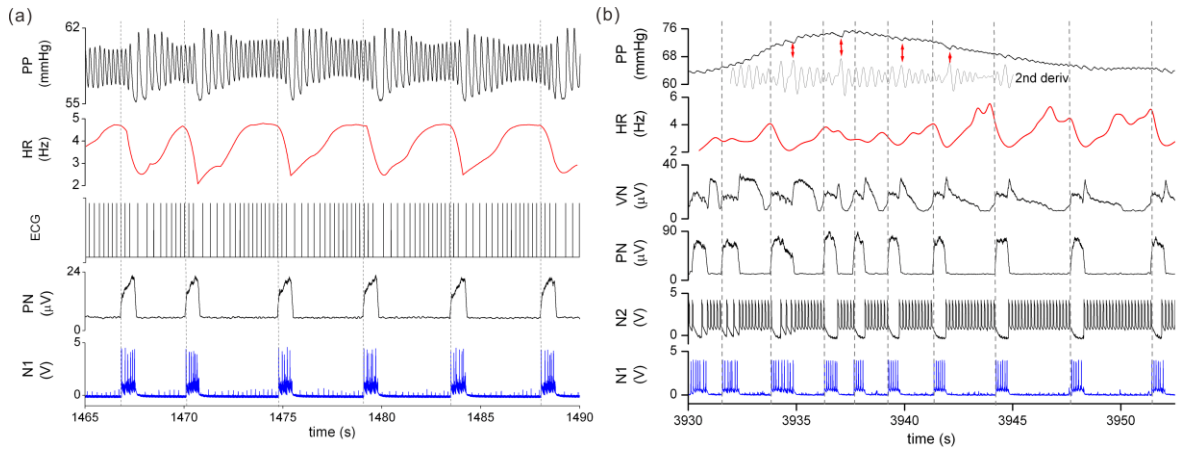
Figure 5.6 Modulating the heart rate by stimulating the vagus nerve in inspiration phase φ_1. The stimuli we used were from N1 and are shown here in blue trace. Besides the voltage output of artificial neurons, signals from the rats, including electrocardiogram (ECG), perfusion pressure (PP), phrenic nerve input (PN), central vagus nerve output (VN) are also shown here. The amplitude of the perfusion pressure signals depend on the position of electrodes. It does not matter to our data analysis. We only concern about the oscillation frequency of the perfusion pressure signals because it indicates the heart rate. (a) shows the modulation for rat 1; (b) shows the modulation for rat 2. In (a), the instantaneous heart rate (HR) was calculated from the ECG. In (b), we failed in collecting the ECG signal. Thus the instantaneous HR is calculated from the fast oscillations of the perfusion pressure. In both rats, vagus nerve stimulation during the inspiration phase causes strong decrease in heart rate and an increase in the amplitude of pressure oscillations. In panel (b), we artificially induced the varying in the duration of respiration cycle. The outputs of the two artificial neurons show very good synchronization with the respiration cycle.

In figure 5.7, the vagus nerve is now stimulated by N2 over the entire expiration phase ($\varphi2+\varphi3$). N1 is triggered by the PN signal. N2 oscillates out of phase with N1. We used the output of N2 as the stimulation. In this way, out of phase synchronization was obtained. During the time of applying the stimulation, the heart rate halves and remains constant. The heart rate drops to 3beats/s for rat 1 (figure 5.7a) and to 2.5beats/s for rat 2 (figure 5.7b). The lowest heart rate is the same with that caused by inspiration stimulation. Therefore the heart rate appears to have saturated at its lower value of about 2.5beats/s. This is found to be the same in both rats. The expiratory phase lasts 4 times longer than the inspiratory phase. As a result, the vagus nerve is modulated 4 times longer than when triggered in the inspiratory phase as seen in figure 5.6. In this case, there is little time for

recovery in between spike bursts. In this case, the heart rate shows a lone peak (figure 5.7b) when N2 stays quiet for an unusually long period of time. Another interesting feature is the series of randomly timed phase slips which appear in figure 5.7a. These are especially clear in the second derivative of the PP curves where heart beats appear to be missing.

Figure 5.7 Modulating the heart rate by stimulating the vagus nerve in expiration phase φ2 + φ3. The vagus nerve is now stimulated by N2 (blue trace) which fires out of phase with N1 and PN. (a) Results from rat 1. Neuromodulation applied during the long expiration phase reduces the average heart rate from ~4.8 beats/s to ~2.5 beats/s. The heart rate occasionally drops to 2 beats/s during the longer bursts (487s). Even during the change of respiration frequency, neurostimulation by N2 remains synchronized out of phase. (b) Results from rat 2. Here also neuromodulation reduces the average heart rate to ~3.2 beat/s. The heart rate increases when N2 falls silent.

Figure 5.8 shows the effect of stimulating the vagus nerve over a short time interval at the early expiration phase (φ2). To achieve this, we used the signal from central vagus (cVN) nerve rather than phrenic signal as an input to N1. The peaks of cVN signal happen at the beginning of the expiration phase, neuron 1 was made to fire during phase φ2 by tuning the amplifier gain so that the cVN signal crosses the N1 threshold near the cVN peak. Figure 5.8(a) shows the cardiorespiratory activity of Rat 2 when stimulated by short bursts of two or three pulses contained in phase φ 2. Given the narrow time window (<0.4s), AIRSA is hardly detectable and the heart keeps beating at its rest pace of 4.8beats/s. When the spike bursts become broad enough to overlap the inspiratory phase as shown in figure 5.8(b), the strong AIRSA described in figure 5.6 is observed again.
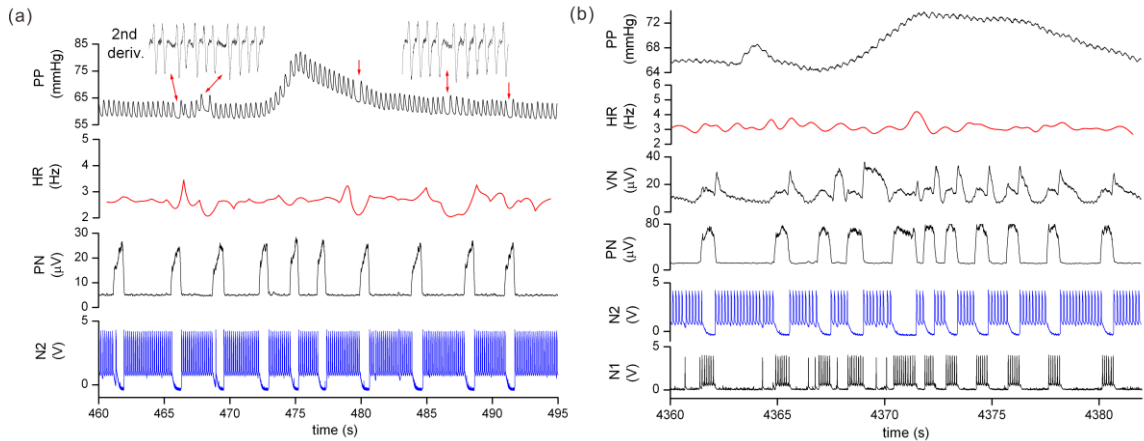
Figure 5.8 Modulating the heart rate by stimulating the vagus nerve in early expiration phase φ_2. The vagus nerve is stimulated by neuron N1 (blue trace) whose firing is triggered by the central vagus nerve. (a) Rat 2-The firing threshold is set at the level of the VN peak producing a narrow spike burst at the beginning of phase 2. The average heart rate 5 beats /s is the natural heart rate. Temporal modulation can be detected. However, it is of the same order as the error on measurement. (b) Rat 2- The firing threshold is set at a lower level giving wider spike bursts that overlap regions 1 and 2. Neuromodulation strongly reduces the heart rate from 5 to 3 beats /s during the spike burst intervals. The PP amplitude triples during the bursts.

From the above results, it would appear that AIRSA depends mainly on the duration of the stimulation, which should be more than 3 consecutive spikes to induce any response. However, the timing of the stimulus also matters. This is going to be shown in figure 5.9. Figure 5.9 reports the effect of applying spike bursts in the second half of the expiratory phase ($\varphi3$). This was achieved by delaying the rise of the current stimulating N2. AIRSA is observed. However, comparing with that in inspiratory phase in figure 5.6, the modulation of the heart rate is weaker despite the spike bursts lasting 2 to 3 times longer than the inspiratory phase. In figure 5.9(a), the heart rate decreases to 2.5-4beats/s compared to 2.5beats/s in figure 5.6. This suggests that it is more difficult to induce AIRSA in the late expiration phase than in the inspiration phase. Further evidence for the reduced sensitivity of phase $\varphi3$ is provided by reducing the duration of spike bursts which is shown in figure 5.9(b). The spike bursts seen after t=5243s have similar width to those applied in the inspiration phase in figure 5.6. However, it did not produce any virtually AIRSA at all.
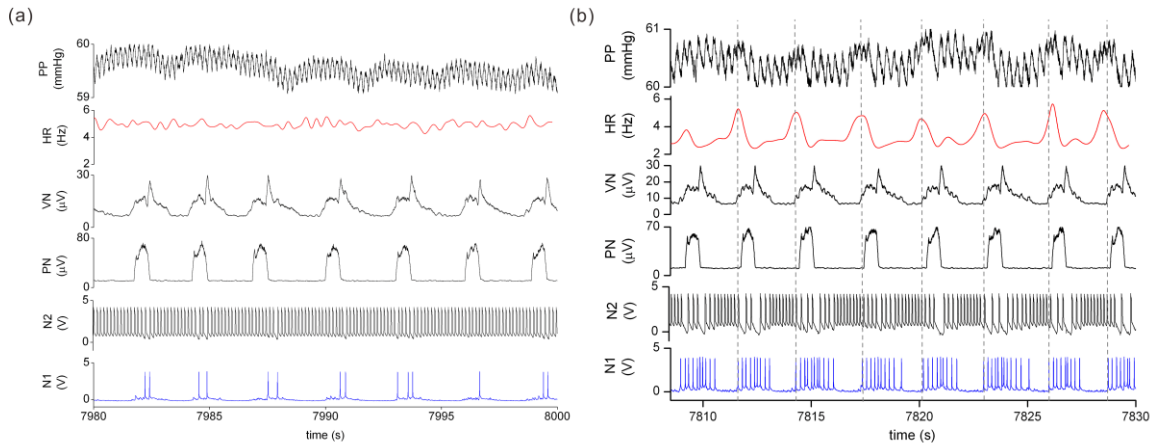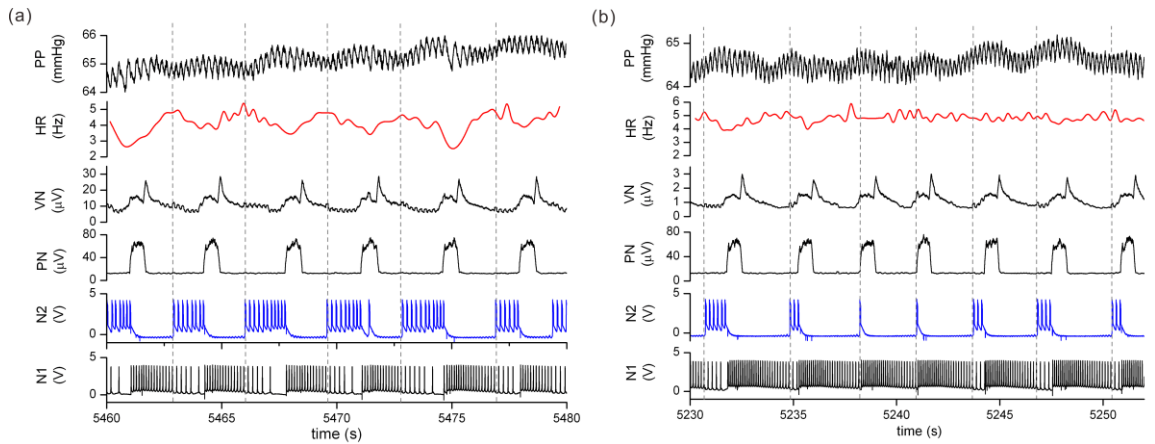
Figure 5.9 Modulating the heart rate by stimulating the vagus nerve in expiration phase φ3. The vagus nerve is stimulated by output of N2 (blue trace), which is delayed by time constant τ. (a) Rat 2/small delay τ: the vagus nerve is stimulated over the full duration of the late expiratory phase. Strong sinus arrhythmia is induced. The heart rate occasionally dropping from 5 beats /s to little less than 3 beats /s. (b) Rat2/long delay τ: the vagus nerve is stimulated at the end of the late expiratory phase (φ3). The resulting sinus arrhythmia is weaker but clearly visible at 5231s, 5253s and 5348s when the spike bursts consist of 3 or more spikes.

Lastly, AIRSA increases arterial pressure as seen by the greater magnitude of the PP oscillations during the time intervals of stimulation. For instance, the PP oscillations double in amplitude when stimulation is applied during the inspiratory phase (figure 5.6a) and triple when it is applied in the late expiratory phase (figure 5.8b).

5.5 Discussion

This study has shown that we can improve the cardio-respiratory system by using the artificial CPG to produce the artificial modulation of the heart rate. So far, the artificial modulation of the heart rate is 16 times greater than the natural one produced by the brainstem CPG. In all the experiments we have done the juvenile rats. Vagus nerve stimulation consistently decreases the heart rate while increasing vascular pressure. The artificial CPG is better than the established pacemaker is that it can induce the natural synchronization to the respiration cycle. In this way, AIRSA is induced.

The competition between neurons in the CPG further allows timing neuron bursts at different points of the respiration cycle. So we can study the response of the heart outside the dynamic range of the brainstem CPG. Another flexibility of stimulation by artificial

neurons is to decrease the heart rate proportionally to the duration of the stimulus. However this response is not the same at every point of the respiration cycle. It varies according to the timing of stimulation. For instance, vagus stimulation makes the heart rate drop at $3Hz/s^2$ in the inspiration phase (figure 5.6, figure 5.8b) but only $1Hz/s^2$ in the late expiration phase (figure 5.8a). This explains the larger heart rate modulation seen in the former case. The reduced sensitivity in the late expiration phase might relate to interaction within the cardiac ganglion such that there is likely to be less noradrenaline released from cardiac sympathetic terminals which fire at end of inspiration and early expiration [109]. Since noradrenaline potentiates vagal nerve responses at the level of the cardiac ganglion ([110, 111]), vagal brachycardia could be reduced. Heart rate recovery during quiescent intervals appears to be the same across the respiration cycle with a recovery rate of $+1Hz/s^2$.

During the expiration stimulation (figure 5.8a), which has a longer time scale than inspiration stimulation, the heart rate does not drop to zero but saturates at 2.5beats/s. This is about the half value of natural heart rate. Without any external perturbation, respiration and the cardiovascular system form two coupled oscillators whose interaction produces RSA (figure 5.5). The effect of constant excitation by the silicon CPG is to introduce a third oscillator which competes with the brainstem CPG to synchronize with the cardiovascular system. In this process N1 and N2 which oscillates at its own frequency (10-50Hz) can lock to the heart beat (2.5Hz). The phase slips indicated by the red arrows in figure 5.8a are believed to arise from such phase locking. This behaviour is known to occur when the synchronization region between two coupled oscillators is being reduced by the action of an external perturbation. In the present case this perturbation is the artificial CPG. Schäfer et al. [100] have modelled the heart as a noisy van der Pol oscillator whose natural oscillation frequency is modulated by respiration. In such system, the perturbation (noise) has the effect of narrowing the region of cardio-respiratory synchronization allowing phase slips to occur.

The CPG technology demonstrated here compute by analogue hardware rather than software. This is a fundamental difference from previous hybrid-neural systems [104, 106]. Our analogue network integrates stimuli in real time. This process has lower power consumption than cardiac pacemakers and its circuits can easily be scaled to less than $1mm^2$ of silicon wafer, all of which are crucial advantages for medical implants. The two-phase oscillations are very robust since our experiments have only required adjusting the

gain of the second amplifier stage to compensate for small differences in the PN amplitude of different rats. To obtain multiphase phase oscillations slow potassium currents would need to be included in the neuron model to deliver spike bursts whose duration is set by winnerless competition rather than simply by the duration of the stimulus.

5.6 Summary

In summary, our silicon CPG has successfully been coupled to juvenile rat models. I fabricated the CPG board and proved that it can induce artificial respiratory sinus arrhythmia and modulate the heart rate according to respiratory cycles. The modulation of the heart output is most effective in the inspiratory phase and is less effective in the late expiratory phase. This paves to way to novel medical devices that mimic biological CPGs to engineer neuro-modulation synchronized to biological rhythms.

Chapter 6 Conclusion

6.1 Summary and Key Insights

We have demonstrated two different types of analogue neuron hardware to perform neurocomputation.

One is a micro transmission line made from magnetic GaMnAs/GaAsSi p-n wires. It emulates nerve fibres and propagates electrical spikes in space. Therefore, we can use it to study the spatial aspect of neurocomputation. The p-n wire integrates inputs in space, times and conditionally regenerates pulses [24, 30, 31]. Moreover, the response of the device to a square stimulus pulse could be a propagating solitary wave. It indicates that the p-n micro wire can transmit information with small power consumption as solitons can propagate over long distances without loss of energy [60]. The spatial aspect goes beyond conductance model of the Hodgkin Huxley type which only considers temporal aspect. In addition, the width of depletion region of a p-n wire can change with temperature. This indicates that the p-n wire can be a thermo-dynamical neuron model. It can describe soliton propagation in bio membranes that incorporates thermodynamic variables [112]. This aspect is superior to that of HH neuron models which do not take into account temperature considerations at all.

The other hardware implementing conductance models is a network consisting of analogue neurons which are coupled via inhibitory synapses.

The conductance model takes into account sodium and potassium ion currents. Consequently, tonic spikes are generated by the silicon neurons. We have demonstrated how to set up the intrinsic properties of individual neurons, such as the amplitude of spikes, firing frequency, etc. These are useful parameters for constructing a neural network. We set up all of these parameters according to results from biological experiments. This is an advantage of HH neurons as they are realistic neuron models. In addition, these neurons respond to stimulus in real time. This is a distinct advantage for medical application.

Spiking neurons are reciprocally connected via electrical synapses which can be either excitatory or inhibitory. We mainly focus on the inhibitory connection. We have demonstrated how to control the coupling strength which is significant in rhythm of output patterns.

Spiking neurons connected via inhibitory synapses make a neural network which can function as a central pattern generator. It produces spatiotemporal patterns and performs polyrhythm generation. We are the first who study the polyrhythmic patterns in neural hardware. We have demonstrated adaptive behaviours of the network by showing stimulus dependent outputs. Besides, we have mapped the phase portraits of output spiking patterns and revealed the attractor dynamics existing in the system. Attraction dynamics is usually associated with functions of brain such as associative memory, pattern recognition, etc. Our research provides the potential of modelling these functions. In addition, we have shown that we can switch between the polyrhythmic outputs of the system by switching the time delay between current inputs. We use winnerless competition principles to explain the mechanism underlying polyrhythm generation in this system. The generation and control of polyrhythm in a neural network is important because it is associated with rhythmic behaviours, such as heart beating, breathing, etc. and locomotive behaviours of animals. And winnerless competition system usually is capable of producing rich rhythms.

The last part of the thesis demonstrated an application of the central pattern generator. We have constructed a central pattern generator device that can generate antiphase spiking patterns. The output patterns are timed by respiratory cycle of juvenile rats. In this way, respiratory phase locking patterns are produced. We have used these patterns modulating the heart rate of juvenile rats and artificially induced the respiratory sinus arrhythmia which can improve the blood pumping efficient of cardiovascular system. Our device can potentially be a novel therapy that mimics the biological CPGs. It could help with restoring the biological rhythms and being implanted in animals.

6.2 Future Directions

The present work opens several avenues for future research.

6.2.1 Soliton Propagation along P-n Wires under Low Temperature Conditions

Firstly, computer modelling of magnetic p-n wires is needed. By calculating the inductance in the material in theory, propagating speed of solitary waves can be predicted. The comparison of results from simulation and experimental measurement shows that the solitary waves propagate does exist in p-n wires.

Secondly, measuring the soliton propagating along the p-n wire under low temperature conditions is in need. One reason for doing this is that the width of depletion region of p-n

layers will change with temperatures and thus result in the changing in capacitance of the p-n wire. This will lead to the change in properties of solitary waves, such as propagating speed, or even break the balance between the nonlinearity and dispersion. Another reason for taking the measurement under low temperature is that the GaMnAs/GaAsSi is magnetic material. It is paramagnetic at room temperature. It will be ferromagnetic when the temperature is under 65K, which is the Curie temperature of this material. In ferromagnetic phase, the magnetic moments in the material will be aligned. This can increase the magnetic flux and thus increase the inductance. Bigger inductance leads to stronger dispersion. It will be interesting to see how the pulses would propagate through the wire in this case.

6.2.2 Carry on with Mapping Attractor Dynamics

We aim to explore the capability of generating polyrhythms of the CPG board and study the stability of attractors.

One way to achieve this is to let more than three neurons participate the competition and see how many different attractors they can generate. And we are also interested in how many stable attractors and attraction basins we can find in the system. In addition, we can add noise to the input in order to test the robustness of these rhythmic patterns to noise.

The second way is that we can take advantage of the flexibility of HH neurons. Additional ion channels associated with calcium currents can be added on the silicon neurons in order to generate spiking-bursting patterns or adaptive spikes. So phase portraits of output patterns generated by CPG board consisting of spiking bursting neurons can be plotted. They could show richer dynamical properties, such as bifurcation, more rhythms, and multi-stabilities, etc.

The third way is that we can try a bigger range of synaptic conductance. So far, the range of the synaptic conductance for us to tune is between 16-45 μS. We can technique improve the synapses to obtain a bigger range of synaptic conductance and see if that could lead to more rhythms.

6.2.3 A New Pacemaker for Improving Cardiovascular Functions

So far our silicon CPG has successfully been coupled to juvenile rat models.

During the previous experiments, we chose the parameters of spiking patterns of the CPG mainly according to experiment effects. Next we need to limit the parameters, such as frequency, pulse width, amplitudes, etc. in the range that satisfies the requirements for medical devices.

We are also trying the CPG board on adult rats and measuring the cardiac output during the modulation, which would provide us a direct evidence of increasing blood pumping efficacy.

After the success in adult rats, we will try the CPG board on sheep and pigs as their heart rate is closer to humans and their age favours implementation of the CPGs. We will also fabricate portable CPG board which can be connected with conscious animals for several days in order to collect real time data under various conditions.

Bibliography

1. Sejnowski, T.J., C. Koch, and P.S. Churchland, *Computational Neuroscience.* Science, 1988. **241**(4871): p. 1299-1306.

2. Hopfield, J.J. and D.W. Tank, *Computing with Neural Circuits - a Model.* Science, 1986. **233**(4764): p. 625-633.

3. Nagarajan, N. and C.F. Stevens, *How does the speed of thought compare for brains and digital computers?* Current Biology, 2008. **18**(17): p. R756-R758.

4. Wolpert, D.M. and Z. Ghahramani, *Computational principles of movement neuroscience.* Nature Neuroscience, 2000. **3**(11): p. 1212-1217.

5. Wong, A.J.W., *Recognition of General Patterns Using Neural Networks.* Biological Cybernetics, 1988. **58**(6): p. 361-372.

6. Hopfield, J.J., *Pattern-Recognition Computation Using Action-Potential Timing for Stimulus Representation.* Nature, 1995. **376**(6535): p. 33-36.

7. Willshaw, D.J., O.P. Buneman, and Longueth.Hc, *Non-Holographic Associative Memory.* Nature, 1969. **222**(5197): p. 960-&.

8. Rabinovich, M.I., et al., *Dynamical principles in neuroscience.* Reviews of Modern Physics, 2006. **78**(4): p. 1213-1265.

9. Brette, R., et al., *Simulation of networks of spiking neurons: A review of tools and strategies.* Journal of Computational Neuroscience, 2007. **23**(3): p. 349-398.

10. Delorme, A. and S.J. Thorpe, *SpikeNET: an event-driven simulation package for modelling large networks of spiking neurons.* Network-Computation in Neural Systems, 2003. **14**(4): p. 613-627.

11. Mahowald, M. and R. Douglas, *A Silicon Neuron.* Nature, 1991. **354**(6354): p. 515-518.

12. Herz, A.V.M., et al., *Modeling single-neuron dynamics and computations: A balance of detail and abstraction.* Science, 2006. **314**(5796): p. 80-85.

13. Knudsen, E.I. and M. Konishi, *Neural Map of Auditory Space in Owl.* Science, 1978. **200**(4343): p. 795-797.

14. Brette, R., *Computing with Neural Synchrony.* Plos Computational Biology, 2012. **8**(6).

15. Nogaret, A., et al., *Artificial ion channels and spike computation in modulation-doped semiconductors.* Europhysics Letters, 2004. **68**(6): p. 874-880.

16. Hodgkin, A.L., A.F. Huxley, and B. Katz, *Measurement of Current-Voltage Relations in the Membrane of the Giant Axon of Loligo.* Journal of Physiology-London, 1952. **116**(4): p. 424-448.

17.   Hodgkin, A.L. and A.F. Huxley, *A Quantitative Description of Membrane Current and Its Application to Conduction and Excitation in Nerve.* Journal of Physiology-London, 1952. **117**(4): p. 500-544.

18.   Rabinovich, M., et al., *Dynamical encoding by networks of competing neuron groups: Winnerless competition.* Physical Review Letters, 2001. **87**(6).

19.   Lodish, H., et al., *Molecular Cell Biology*. 2012: W. H. Freeman.

20.   Debanne, D., et al., *Axon Physiology.* Physiological Reviews, 2011. **91**(2): p. 555-602.

21.   Gerstner, W. and W.M. Kistler, *Spiking neuron models: Single neurons, populations, plasticity*. 2002: Cambridge university press.

22.   Choquet, D. and A. Triller, *The dynamic synapse.* Neuron, 2013. **80**(3): p. 691-703.

23.   Koester, J. and S.A. Siegelbaum, *Membrane potential.* Principles of neural science, 1991. **4**: p. 125-139.

24.   Samardak, A.S., et al., *Coincidence detection and spike regeneration in artificial neurons.* Physica Status Solidi a-Applications and Materials Science, 2008. **205**(11): p. 2651-2654.

25.   Gerstner, W. and W.M. Kistler, *Mathematical formulations of Hebbian learning.* Biological Cybernetics, 2002. **87**(5-6): p. 404-415.

26.   Hebb, D.O., J.L. Martinez, and S.E. Glickman, *The Organization of Behavior - a Neuropsychological Theory - Hebb,Do.* Contemporary Psychology, 1994. **39**(11): p. 1018-1020.

27.   Jeffress, L.A., *A Place Theory of Sound Localization.* Journal of Comparative and Physiological Psychology, 1948. **41**(1): p. 35-39.

28.   Moiseff, A. and M. Konishi, *The Owls Inter-Aural Pathway Is Not Involved in Sound Localization.* Journal of Comparative Physiology, 1981. **144**(3): p. 299-304.

29.   Koch, C., *Cable Theory in Neurons with Active, Linearized Membranes.* Biological Cybernetics, 1984. **50**(1): p. 15-33.

30.   Samardak, A., et al., *Propagation and spatiotemporal summation of electrical pulses in semiconductor nerve fibers.* Applied Physics Letters, 2007. **91**(7).

31.   Samardak, A., et al., *An analogue sum and threshold neuron based on the quantum tunnelling amplification of electrical pulses.* New Journal of Physics, 2008. **10**.

32.   Samardak, A., et al., *Noise-Controlled Signal Transmission in a Multithread Semiconductor Neuron.* Physical Review Letters, 2009. **102**(22).

33.   Levin, J.E. and J.P. Miller, *Broadband neural encoding in the cricket cercal sensory system enhanced by stochastic resonance.* Nature, 1996. **380**(6570): p. 165-168.

34.   Long, L.N. and G. Fang. *A review of biologically plausible neuron models for spiking neural networks*. in *AIAA InfoTech@ Aerospace Conference, Atlanta, GA*. 2010.

35.   Ermentrout, B., *Type I membranes, phase resetting curves, and synchrony.* Neural Computation, 1996. **8**(5): p. 979-1001.

36.   Latham, P.E., et al., *Intrinsic dynamics in neuronal networks. II. Experiment.* Journal of Neurophysiology, 2000. **83**(2): p. 828-835.

37.   Fourcaud-Trocme, N., et al., *How spike generation mechanisms determine the neuronal response to fluctuating inputs.* Journal of Neuroscience, 2003. **23**(37): p. 11628-11640.

38.   Fitzhugh, R., *Impulses and Physiological States in Theoretical Models of Nerve Membrane.* Biophysical Journal, 1961. **1**(6): p. 445-&.

39.   Morris, C. and H. Lecar, *Voltage Oscillations in the Barnacle Giant Muscle-Fiber.* Biophysical Journal, 1981. **35**(1): p. 193-213.

40.   Izhikevich, E.M., *Which model to use for cortical spiking neurons?* Ieee Transactions on Neural Networks, 2004. **15**(5): p. 1063-1070.

41.   Pospischil, M., et al., *Comparison of different neuron models to conductance-based post-stimulus time histograms obtained in cortical pyramidal cells using dynamic-clamp in vitro.* Biological Cybernetics, 2011. **105**(2): p. 167-180.

42.   Getting, P.A., *Emerging Principles Governing the Operation of Neural Networks.* Annual Review of Neuroscience, 1989. **12**: p. 185-204.

43.   Grillner, S., *Biological pattern generation: The cellular and computational logic of networks in motion.* Neuron, 2006. **52**(5): p. 751-766.

44.   Marder, E. and R.L. Calabrese, *Principles of rhythmic motor pattern generation.* Physiological Reviews, 1996. **76**(3): p. 687-717.

45.   Ijspeert, A.J., *Central pattern generators for locomotion control in animals and robots: A review.* Neural Networks, 2008. **21**(4): p. 642-653.

46.   Marder, E. and D. Bucher, *Understanding circuit dynamics using the stomatogastric nervous system of lobsters and crabs.* Annual Review of Physiology, 2007. **69**: p. 291-316.

47.   Reyes, M.B., et al., *Artificial synaptic modification reveals a dynamical invariant in the pyloric CPG.* European Journal of Applied Physiology, 2008. **102**(6): p. 667-675.

48.   Zeeman, E.C. and M.L. Zeeman, *An n-dimensional competitive Lotka-Volterra system is generically determined by the edges of its carrying simplex.* Nonlinearity, 2002. **15**(6): p. 2019-2032.

49.   Izhikevich, E.M., *Dynamical systems in neuroscience*. 2007: MIT press.

50.   Silberberg, G., et al., *Synaptic pathways in neural microcircuits.* Trends in Neurosciences, 2005. **28**(10): p. 541-551.

51.   Solis, M.M. and D.J. Perkel, *Rhythmic activity in a forebrain vocal control nucleus in vitro.* Journal of Neuroscience, 2005. **25**(11): p. 2811-2822.

52.   Yuste, R., et al., *The cortex as a central pattern generator.* Nature Reviews Neuroscience, 2005. **6**(6): p. 477-483.

53.   Traven, H.G.C., et al., *Computer-Simulations of Nmda and Non-Nmda Receptor-Mediated Synaptic Drive - Sensory and Supraspinal Modulation of Neurons and Small Networks.* Journal of Neurophysiology, 1993. **70**(2): p. 695-709.

54.   Hellgren, J., S. Grillner, and A. Lansner, *Computer-Simulation of the Segmental Neural Network Generating Locomotion in Lamprey by Using Populations of Network Interneurons.* Biological Cybernetics, 1992. **68**(1): p. 1-13.

55.   Wojcik, J., R. Clewley, and A. Shilnikov, *Order parameter for bursting polyrhythms in multifunctional central pattern generators.* Physical Review E, 2011. **83**(5).

56.   Shilnikov, A., R. Gordon, and I. Belykh, *Polyrhythmic synchronization in bursting networking motifs.* Chaos, 2008. **18**(3).

57.   Kristan, W.B., R.L. Calabrese, and W.O. Friesen, *Neuronal control of leech behavior.* Progress in Neurobiology, 2005. **76**(5): p. 279-327.

58.   Yu, X.T., B. Nguyen, and W.O. Friesen, *Sensory feedback can coordinate the swimming activity of the leech.* Journal of Neuroscience, 1999. **19**(11): p. 4634-4643.

59.   Friesen, W.O. and J.H. Cang, *Sensory and central mechanisms control intersegmental coordination.* Current Opinion in Neurobiology, 2001. **11**(6): p. 678-683.

60.   Heimburg, T. and A.D. Jackson, *On soliton propagation in biomembranes and nerves.* Proceedings of the National Academy of Sciences of the United States of America, 2005. **102**(28): p. 9790-9795.

61.   Kuusela, T., et al., *Soliton experiments in a nonlinear electrical transmission line.* European Journal of Physics, 1987. **8**(1): p. 27.

62.   Toda, M., *Nonlinear waves and solitons*. Vol. 5. 1989: Springer.

63.   Kuusela, T., *Soliton Experiments in a Damped Ac-Driven Nonlinear Electrical Transmission-Line.* Physics Letters A, 1992. **167**(1): p. 54-59.

64.   Camassa, R., J.M. Hyman, and B.P. Luce, *Nonlinear waves and solitons in physical systems.* Physica D, 1998. **123**(1-4): p. 1-20.

65.   Toda, M., *Study of one-dimensional nonlinear lattice - Review.* Proceedings of the Japan Academy Series B-Physical and Biological Sciences, 2004. **80**(10): p. 445-458.

66.   Sze, S.M., *Semiconductor devices, physics and technology*. 1985: Wiley.

67.   Smith, L.S., *Implementing neural models in silicon*, in *Handbook of nature-inspired and innovative computing*. 2006, Springer. p. 433-475.

68.   Mead, C., *Analog VLSI and neural systems*. 1989: Addison-Wesley.

69.   Nogaret, A., et al., *Modulation of respiratory sinus arrhythmia in rats with central pattern generator hardware.* Journal of Neuroscience Methods, 2013. **212**(1): p. 124-132.

70.   Nicholls, J.G., *From Neuron to Brain*. 2012: Sinauer Associates, Incorporated.

71.   Bennett, M.V.L., *Electrical synapses, a personal perspective (or history).* Brain Research Reviews, 2000. **32**(1): p. 16-28.

72.   Jefferys, J.G., R.D. Traub, and M.A. Whittington, *Neuronal networks for induced '40 Hz' rhythms.* Trends Neurosci, 1996. **19**(5): p. 202-8.

73.   Ermentrout, B., *Complex Dynamics in Winner-Take-All Neural Nets with Slow Inhibition.* Neural Networks, 1992. **5**(3): p. 415-431.

74.   Huguenard, J.R., O.P. Hamill, and D.A. Prince, *Developmental changes in Na+ conductances in rat neocortical neurons: appearance of a slowly inactivating component.* J Neurophysiol, 1988. **59**(3): p. 778-95.

75.   Huguenard, J.R. and D.A. McCormick, *Simulation of the currents involved in rhythmic oscillations in thalamic relay neurons.* J Neurophysiol, 1992. **68**(4): p. 1373-83.

76.   Kiehn, O., *Locomotor circuits in the mammalian spinal cord.* Annual Review of Neuroscience, 2006. **29**: p. 279-306.

77.   Hess, A., et al., *Neural Mechanisms Underlying Breathing Complexity.* Plos One, 2013. **8**(10).

78.   Grillner, S., et al., *Microcircuits in action - from CPGs to neocortex.* Trends in Neurosciences, 2005. **28**(10): p. 525-533.

79.   Wojcik, J., et al., *Key Bifurcations of Bursting Polyrhythms in 3-Cell Central Pattern Generators.* Plos One, 2014. **9**(4).

80.   McCrea, D.A. and I.A. Rybak, *Organization of mammalian locomotor rhythm and pattern generation.* Brain Research Reviews, 2008. **57**(1): p. 134-146.

81.   Laurent, G., et al., *Odor encoding as an active, dynamical process: Experiments, computation, and theory.* Annual Review of Neuroscience, 2001. **24**: p. 263-297.

82.   Arena, P., et al., *The winnerless competition paradigm in cellular nonlinear networks: Models and applications.* International Journal of Circuit Theory and Applications, 2009. **37**(4): p. 505-528.

83.   Afraimovich, V.S., M.I. Rabinovich, and P. Varona, *Heteroclinic contours in neural ensembles and the winnerless competition principle.* International Journal of Bifurcation and Chaos, 2004. **14**(4): p. 1195-1208.

84.   Zhang, X., et al., *Transition from winnerless competition to synchronization in time-delayed neuronal motifs.* Epl, 2012. **97**(5).

85.   Gonzalez-Diaz, L.A., et al., *Winnerless competition in coupled Lotka-Volterra maps.* Physical Review E, 2013. **88**(1).

86.   Fukushima, K., *Neocognitron - a Hierarchical Neural Network Capable of Visual-Pattern Recognition.* Neural Networks, 1988. **1**(2): p. 119-130.

87.   Hopfield, J.J., *Neural Networks and Physical Systems with Emergent Collective Computational Abilities.* Proceedings of the National Academy of Sciences of the United States of America-Biological Sciences, 1982. **79**(8): p. 2554-2558.

88.   Daun, S., J.E. Rubin, and I.A. Rybak, *Control of oscillation periods and phase durations in half-center central pattern generators: a comparative mechanistic analysis.* Journal of Computational Neuroscience, 2009. **27**(1): p. 3-36.

89.   Satterlie, R.A., T.P. Norekian, and T.J. Pirtle, *Serotonin-induced spike narrowing in a locomotor pattern generator permits increases in cycle frequency during accelerations.* Journal of Neurophysiology, 2000. **83**(4): p. 2163-2170.

90.   Norris, B.J., et al., *A central pattern generator producing alternative outputs: Temporal pattern of premotor activity.* Journal of Neurophysiology, 2006. **96**(1): p. 309-326.

91.   Ben-Tal, A., S.S. Shamailov, and J.F.R. Paton, *Evaluating the physiological significance of respiratory sinus arrhythmia: looking beyond ventilation-perfusion efficiency.* Journal of Physiology-London, 2012. **590**(8): p. 1989-2008.

92.   Richter, D., *Neural regulation of respiration: rhythmogenesis and afferent control*, in *Comprehensive human physiology*. 1996, Springer. p. 2079-2095.

93.   Ezure, K., *Synaptic connections between medullary respiratory neurons and considerations on the genesis of respiratory rhythm.* Progress in neurobiology, 1990. **35**(6): p. 429-450.

94.   Abdala, A.P.L., et al., *Abdominal expiratory activity in the rat brainstem-spinal cord in situ: patterns, origins and implications for respiratory rhythm generation.* Journal of Physiology-London, 2009. **587**(14): p. 3539-3559.

95.   Baekey, D.M., et al., *Effect of baroreceptor stimulation on the respiratory pattern: Insights into respiratory-sympathetic interactions.* Respiratory Physiology & Neurobiology, 2010. **174**(1-2): p. 135-145.

96.   Nicholls, J.G. and J.F.R. Paton, *Brainstem: neural networks vital for life.* Philosophical Transactions of the Royal Society B-Biological Sciences, 2009. **364**(1529): p. 2447-2451.

97.   Champagnat, J., et al., *Developmental basis of the rostro-caudal organization of the brainstem respiratory rhythm generator.* Philosophical Transactions of the Royal Society B-Biological Sciences, 2009. **364**(1529): p. 2469-2476.

98.   La Rovere, M.T., et al., *Baroreflex sensitivity and heart-rate variability in prediction of total cardiac mortality after myocardial infarction.* Lancet, 1998. **351**(9101): p. 478-484.

99.   Mortara, A., et al., *Can Power Spectral-Analysis of Heart-Rate-Variability Identify a High-Risk Subgroup of Congestive-Heart-Failure Patients with Excessive Sympathetic Activation - a Pilot-Study before and after Heart-Transplantation - Abstracts.* British Heart Journal, 1994. **71**(5): p. 422-430.

100.   Schafer, C., et al., *Synchronization in the human cardiorespiratory system.* Physical Review E, 1999. **60**(1): p. 857-870.

101.   Landa, P.S. and M.G. Rosenblum, *Modified Mackey-Glass Model of Respiration Control.* Physical Review E, 1995. **52**(1): p. R36-R39.

102.   Rosenblum, M.G., et al., *Identification of coupling direction: Application to cardiorespiratory interaction.* Physical Review E, 2002. **65**(4).

103.   Rulkov, N.F., et al., *Generalized Synchronization of Chaos in Directionally Coupled Chaotic Systems.* Physical Review E, 1995. **51**(2): p. 980-994.

104.   Pinto, R.D., et al., *Extended dynamic clamp: controlling up to four neurons using a single desktop computer and interface.* Journal of Neuroscience Methods, 2001. **108**(1): p. 39-48.

105.   Elson, R.C., et al., *Synchronous behavior of two coupled biological neurons.* Physical Review Letters, 1998. **81**(25): p. 5692-5695.

106.   Olypher, A., G. Cymbalyuk, and R.L. Calabrese, *Hybrid systems analysis of the control of burst duration by low-voltage-activated calcium current in leech heart interneurons.* Journal of Neurophysiology, 2006. **96**(6): p. 2857-2867.

107.   Hayano, J., et al., *Respiratory sinus arrhythmia a phenomenon improving pulmonary gas exchange and circulatory efficiency.* Circulation, 1996. **94**(4): p. 842-847.

108.   Paton, J.F.R., *A working heart-brainstem preparation of the mouse.* Journal of Neuroscience Methods, 1996. **65**(1): p. 63-68.

109.   Boscan, P., A.M. Allen, and J.F.R. Paton, *Baroreflex inhibition of cardiac sympathetic outflow is attenuated by angiotensin II in the nucleus of the solitary tract.* Neuroscience, 2001. **103**(1): p. 153-160.

110.   Levy, M.N., et al., *Sympathetic and Parasympathetic Interactions Upon Left Ventricle of Dog.* Circulation Research, 1966. **19**(1): p. 5-&.

111.   Potter, E., *Presynaptic Inhibition of Cardiac Vagal Postganglionic Nerves by Neuropeptide-Y.* Neuroscience Letters, 1987. **83**(1-2): p. 101-106.

112.   Krilowicz, B.L., D.M. Edgar, and H.C. Heller, *Action-Potential Duration Increases as Body-Temperature Decreases during Hibernation.* Brain Research, 1989. **498**(1): p. 73-80.